



# NAVAL POSTGRADUATE SCHOOL

MONTEREY, CALIFORNIA

## DISSERTATION

**MOTION OF THE DEBRIS FROM A HIGH-ALTITUDE  
NUCLEAR EXPLOSION: SIMULATIONS INCLUDING  
COLLISIONLESS SHOCK AND CHARGE EXCHANGE**

by

David P. Morrow

June 2014

Dissertation Supervisor:

David Larson

**Approved for public release; distribution is unlimited**

THIS PAGE INTENTIONALLY LEFT BLANK

<b>REPORT DOCUMENTATION PAGE</b>			<i>Form Approved OMB No. 0704-0188</i>	
Public reporting burden for this collection of information is estimated to average 1 hour per response, including the time for reviewing instruction, searching existing data sources, gathering and maintaining the data needed, and completing and reviewing the collection of information. Send comments regarding this burden estimate or any other aspect of this collection of information, including suggestions for reducing this burden, to Washington headquarters Services, Directorate for Information Operations and Reports, 1215 Jefferson Davis Highway, Suite 1204, Arlington, VA 22202-4302, and to the Office of Management and Budget, Paperwork Reduction Project (0704-0188) Washington, DC 20503.				
<b>1. AGENCY USE ONLY (Leave blank)</b>		<b>2. REPORT DATE</b> June 2014	<b>3. REPORT TYPE AND DATES COVERED</b> Dissertation	
<b>4. TITLE AND SUBTITLE</b> MOTION OF THE DEBRIS FROM A HIGH-ALTITUDE NUCLEAR EXPLOSION: SIMULATIONS INCLUDING COLLISIONLESS SHOCK AND CHARGE EXCHANGE			<b>5. FUNDING NUMBERS</b>	
<b>6. AUTHOR(S)</b> David P. Morrow				
<b>7. PERFORMING ORGANIZATION NAME(S) AND ADDRESS(ES)</b> Naval Postgraduate School Monterey, CA 93943-5000			<b>8. PERFORMING ORGANIZATION REPORT NUMBER</b>	
<b>9. SPONSORING / MONITORING AGENCY NAME(S) AND ADDRESS(ES)</b> N/A			<b>10. SPONSORING / MONITORING AGENCY REPORT NUMBER</b>	
<b>11. SUPPLEMENTARY NOTES</b> The views expressed in this thesis are those of the author and do not reflect the official policy or position of the Department of Defense or the U.S. Government. IRB Protocol number ____N/A____.				
<b>12a. DISTRIBUTION / AVAILABILITY STATEMENT</b> Approved for public release; distribution is unlimited			<b>12b. DISTRIBUTION CODE</b> A	
<b>13. ABSTRACT (maximum 200 words)</b>  In 1962, the United States conducted its final atmospheric nuclear test. Since 1962, the American national laboratories have attempted to simulate the results observed in exo-atmospheric testing in order to understand and explain how high-energy electrons became trapped further across the Earth's magnetic field than expected.  In this thesis, my research will use a computer modeling program designed by the late Dr. Dennis Hewett for LLNL in 1972 to simulate the debris from a High Altitude Nuclear Explosion (HANE). The objective of this research is to examine two physical phenomena, collisionless shocks driven by multiple ion species and charge exchange, to determine their independent relevance to the final spatial disposition of fission fragments from a HANE.  This research used the ZMR code, a one-dimensional, particle-in-cell plasma code to simulate the movement of the debris ions produced by the HANE. The debris ions are assumed to be the source of the measured high-energy electrons due to subsequent beta-decay. These high-energy electrons can damage the satellite network vital to the Department of Defense and security of the nation.				
<b>14. SUBJECT TERMS</b> High-Altitude Nuclear Explosion, Charge Exchange, Collisionless Shock, Hybrid Plasma Code			<b>15. NUMBER OF PAGES</b> 135	
			<b>16. PRICE CODE</b>	
<b>17. SECURITY CLASSIFICATION OF REPORT</b> Unclassified	<b>18. SECURITY CLASSIFICATION OF THIS PAGE</b> Unclassified	<b>19. SECURITY CLASSIFICATION OF ABSTRACT</b> Unclassified	<b>20. LIMITATION OF ABSTRACT</b> UU	

THIS PAGE INTENTIONALLY LEFT BLANK



**Approved for public release; distribution is unlimited**

**MOTION OF THE DEBRIS FROM A HIGH-ALTITUDE NUCLEAR  
EXPLOSION: SIMULATIONS INCLUDING COLLISIONLESS SHOCK AND  
CHARGE EXCHANGE**

David P. Morrow  
Lieutenant Colonel, United States Army  
B.S., United States Military Academy, 1991  
M.S., Air Force Institute of Technology, 2003

Submitted in partial fulfillment of the  
requirements for the degree of

**DOCTOR OF PHILOSOPHY IN PHYSICS**

from the

**NAVAL POSTGRADUATE SCHOOL  
June 2014**

Author: David P. Morrow

Approved by:	David J. Larson Lawrence Livermore National Lab Dissertation Supervisor	Craig F. Smith Professor of Physics Dissertation Committee Chair
--------------	---	--

William B. Colson Professor of Physics	James H. Luscombe Professor of Physics
---	---

Todd R. Weatherford Professor of Electrical Engineering	Christopher G. Cross DTRA Stockpile Associate
--	--

Approved by: Andres Larraza, Chair, Department of Physics

Approved by: Douglas Moses, Vice Provost for Academic Affairs

THIS PAGE INTENTIONALLY LEFT BLANK

## **ABSTRACT**

In 1962, the United States conducted its final atmospheric nuclear test. Since 1962, the American national laboratories have attempted to simulate the results observed in exo-atmospheric testing in order to understand and explain how high-energy electrons became trapped further across the Earth's magnetic field than expected.

In this thesis, my research will use a computer modeling program designed by the late Dr. Dennis Hewett for LLNL in 1972 to simulate the debris from a High Altitude Nuclear Explosion (HANE). The objective of this research is to examine two physical phenomena, collisionless shocks driven by multiple ion species and charge exchange, to determine their independent relevance to the final spatial disposition of fission fragments from a HANE.

This research used the ZMR code, a one-dimensional, particle-in-cell plasma code to simulate the movement of the debris ions produced by the HANE. The debris ions are assumed to be the source of the measured high-energy electrons due to subsequent beta-decay. These high-energy electrons can damage the satellite network vital to the Department of Defense and security of the nation.

THIS PAGE INTENTIONALLY LEFT BLANK

# TABLE OF CONTENTS

<b>I.</b>	<b>INTRODUCTION .....</b>	<b>1</b>
<b>A.</b>	<b>INTRODUCTION.....</b>	<b>1</b>
<b>B.</b>	<b>PREVIOUS WORK IN THIS FIELD .....</b>	<b>4</b>
<b>C.</b>	<b>RESEARCH OBJECTIVES AND METHODOLOGY .....</b>	<b>6</b>
<b>II.</b>	<b>BACKGROUND PHYSICS.....</b>	<b>9</b>
<b>A.</b>	<b>L-SHELL MODEL OF EARTH'S MAGNETIC FIELD.....</b>	<b>9</b>
<b>B.</b>	<b>MOTION OF A CHARGED PARTICLE IN A CONSTANT MAGNETIC FIELD.....</b>	<b>11</b>
<b>C.</b>	<b>MOTION OF A CHARGED PARTICLE IN A DYNAMIC MAGNETIC FIELD.....</b>	<b>13</b>
<b>D.</b>	<b>OVERVIEW OF FISSION .....</b>	<b>15</b>
<b>III.</b>	<b>THE STARFISH PRIME TEST .....</b>	<b>19</b>
<b>A.</b>	<b>PHYSICAL SETTING .....</b>	<b>19</b>
<b>B.</b>	<b>MAGNETIC BUBBLE OBSERVATIONS .....</b>	<b>20</b>
<b>C.</b>	<b>OBSERVED BELT PUMPING.....</b>	<b>21</b>
<b>IV.</b>	<b>COLLISIONLESS SHOCK.....</b>	<b>25</b>
<b>A.</b>	<b>FORMATION OF COLLISIONLESS SHOCK.....</b>	<b>25</b>
<b>B.</b>	<b>COUPLING OF DEBRIS TO BACKGROUND PLASMA .....</b>	<b>29</b>
<b>V.</b>	<b>CHARGE EXCHANGE.....</b>	<b>35</b>
<b>A.</b>	<b>OVERVIEW.....</b>	<b>35</b>
<b>1.</b>	<b>General Overview .....</b>	<b>35</b>
<b>2.</b>	<b>Electron Capture.....</b>	<b>37</b>
<b>3.</b>	<b>Electron Loss .....</b>	<b>37</b>
<b>B.</b>	<b>SEMI-EMPIRICAL FORMULATION.....</b>	<b>38</b>
<b>C.</b>	<b>MATCH OF SEMI-EMPERICAL FORMULA TO EXPERIMENTAL DATA .....</b>	<b>39</b>
<b>VI.</b>	<b>ZMR CODE DESCRIPTION.....</b>	<b>45</b>
<b>A.</b>	<b>OVERVIEW.....</b>	<b>45</b>
<b>B.</b>	<b>COMPUTATIONAL FLOW IN ZMR.....</b>	<b>49</b>
<b>C.</b>	<b>INITIAL CONDITIONS USED IN THE SIMULATIONS.....</b>	<b>51</b>
<b>D.</b>	<b>SPECIFIC MODIFICATIONS FOR THIS WORK .....</b>	<b>51</b>
<b>1.</b>	<b>Modifications for Including Multiple Species .....</b>	<b>51</b>
<b>2.</b>	<b>Modifications to Analyze Charge Exchange.....</b>	<b>52</b>
<b>E.</b>	<b>VERIFICATION OF ZMR.....</b>	<b>56</b>
<b>F.</b>	<b>OVERVIEW OF SIMULATIONS EMPLOYED.....</b>	<b>59</b>
<b>VII.</b>	<b>RESULTS AND CONCLUSIONS .....</b>	<b>65</b>
<b>A.</b>	<b>OVERVIEW.....</b>	<b>65</b>
<b>1.</b>	<b>Simulations Examining Collisionless Shock Driven by Multiple Ion Species .....</b>	<b>65</b>
<b>2.</b>	<b>Simulations Completed Examining Charge Exchange.....</b>	<b>66</b>

B.	MULTISPECIES COLLISIONLESS SHOCK .....	67
1.	Debris Co-Located .....	68
2.	Debris Staggered .....	71
C.	CHARGE EXCHANGE .....	74
1.	Sensitivity .....	75
2.	Effects of Collisionless Shock on Charge Exchange .....	75
3.	Constant and Exponential Atmosphere .....	78
4.	Slip through with Constant Atmosphere .....	79
a.	<i>Uranium Only</i> .....	79
b.	<i>Uranium and Xenon</i> .....	81
c.	<i>Uranium and Zirconium</i> .....	84
d.	<i>Uranium and Lead</i> .....	87
5.	Slip through with Exponential Atmosphere .....	90
a.	<i>Uranium Only</i> .....	90
b.	<i>Uranium and Xenon</i> .....	93
c.	<i>Uranium and Zirconium</i> .....	95
d.	<i>Uranium and Lead</i> .....	98
6.	Calculations of Neutral Yield to Match Measured Flux .....	101
D.	ANALYSIS OF DATA .....	102
1.	Atmospheric profiles.....	102
2.	Elemental Considerations .....	102
E.	RECOMMENDATIONS FOR FUTURE WORK.....	103
E.	CONCLUSIONS .....	105
	LIST OF REFERENCES .....	109
	INITIAL DISTRIBUTION LIST .....	115

## LIST OF FIGURES

Figure 1.	Simple drawing of Earth's L-Shell organization and general sketch of a magnetic dipole field.....	10
Figure 2.	Motion of a charged particle in the Earth's dipole magnetic field (after Hess, 1964). ....	14
Figure 3.	Distribution of mass of fission fragments from the fission of uranium-235 by a thermal neutron (after Krane, 1988).....	17
Figure 4.	Number density of gaseous components of nighttime atmosphere above Johnston Atoll as a function of altitude (after Larson, 2011) .....	20
Figure 5.	Time dependent size of diamagnetic cavity produced by STARFISH detonation with flight path of instrumented rockets superimposed showing times instruments were collecting data (after Dyal, 2006) .....	21
Figure 6.	Collisionless shock observed in z component of magnetic field during author's simulation of expanding plasma pushing against background plasma after 1725 time steps while the debris has expanded out to $10^7$ cm. ....	29
Figure 7.	Phase space plot of radial velocity versus radius for author's simulation of uncoupled plasma (red) expanding into a background plasma (blue). ....	32
Figure 8.	Phase space plot of radial velocity versus radius for author's simulation of a coupled debris plasma (red) expanding into background plasma (blue).....	33
Figure 9.	Experimental and semi-empirical cross section of electron capture of Xenon +1 as a function of velocity. ....	40
Figure 10.	Experimental and semi-empirical cross section of electron loss of Xenon +1 as a function of velocity.....	41
Figure 11.	Experimental and semi-empirical cross section of electron capture of Uranium+1 as a function of velocity. ....	42
Figure 12.	Experimental and semi-empirical cross section of electron loss of Uranium+1 as a function of velocity. ....	43
Figure 13.	View of simulation grid with one simulation particle (green) and diamonds showing cell centered field values. Only the blue diamonds contribute to the force computations for the green simulation particle.....	49
Figure 14.	Oxygen+1 background plasma number density as a function of radius. ....	56
Figure 15.	Neutral fraction of uranium in theoretical calculation as a function of penetration distance. ....	58
Figure 16.	Neutral fraction of uranium in test simulation as a function of real time. ....	59
Figure 17.	Simulation of two uranium debris species with charge states +1 (green) and +2(red) expanding into a background plasma of O+1 (blue) plotted as a radial velocity [cm/s] versus radial distance [cm]. The smooth profile for uranium +1 indicates no acceleration.....	69
Figure 18.	Simulation of two uranium debris species with charge states +1 (green) and +4 (red) expanding into a background plasma of O+1 (blue) plotted as a radial velocity [cm/s] versus radial distance [cm]. The smooth profile for uranium +1 indicates no acceleration.....	70

Figure 19.	Simulation of two uranium debris species with charge state +1 (green) and +8 (red) expanding into a background plasma of O+1 (blue) plotted as a radial velocity [cm/s] versus radial distance [cm]. The smooth profile for uranium +1 indicates no acceleration. ....	71
Figure 20.	Simulation of two uranium debris species with charge state +1 (red) and +2 (green) expanding into a background plasma of O+1 (blue) plotted as a radial velocity [cm/s] versus radial distance [cm]. The smooth profile for uranium +1 indicates no acceleration. ....	72
Figure 21.	Simulation of two uranium debris species with charge state +1 (red) and +4 (green) expanding into a background plasma of O+1 (blue) plotted as a radial velocity [cm/s] versus radial distance [cm]. The smooth profile for uranium +1 indicates no acceleration. ....	73
Figure 22.	Simulation of two uranium debris species with charge state +1 (red) and +8 (green) expanding into a background plasma of O+1 (blue) plotted as a radial velocity [cm/s] versus radial distance [cm]. The smooth profile for uranium +1 indicates no acceleration. ....	74
Figure 23.	Simulation of uranium+1 expanding into a background of neutral hydrogen without generating a collisionless shock and with charge exchange enabled. ....	76
Figure 24.	Simulation of uranium+1 expanding into a background of oxygen+1 while generating a collisionless shock and with charge exchange enabled. Plot of number of real, neutral uranium atoms as a function of time. ....	77
Figure 25.	Simulation of Uranium+1 (red) expanding into background plasma of Oxygen+1 (blue) in a constant atmosphere without charge exchange. ....	79
Figure 26.	Simulation of Uranium+1 expanding into background plasma of Oxygen+1 in a constant atmosphere with charge exchange. ....	80
Figure 27.	Simulation involving Uranium+1 (light blue) and Xenon+1 (red) expanding into background plasma of Oxygen+1 with a constant atmosphere without charge exchange. ....	82
Figure 28.	Simulation involving Uranium+1 (light blue) and Xenon+1 (gold) expanding into a background plasma of Oxygen+1 with a constant atmosphere and charge exchange enabled. ....	83
Figure 29.	Simulation involving Uranium+1 (green) and Zirconium+1 (red) expanding into a background plasma of O+1 (blue) with a constant atmosphere without charge exchange. ....	85
Figure 30.	Simulation involving Uranium+1 (light blue) and Zirconium+1 (gold) expanding into a background plasma of O+1 (blue) with a constant atmosphere and charge exchange. ....	86
Figure 31.	Simulation involving Uranium+1 (green) and Lead+1 (red) expanding into a background of Oxygen+1 (blue) with a constant atmosphere without charge exchange. ....	88
Figure 32.	Simulation with Uranium +1 (light blue) and Lead+1 (gold) expanding into a background plasma of Oxygen+1 (blue) in a constant atmosphere with charge exchange. ....	89



Figure 33.	Simulation involving Uranium +1 (Red) into Oxygen +1 (Blue) without charge exchange where the debris couples into background. ....	91
Figure 34.	Simulation involving Uranium +1 (Green) into Oxygen +1 (Blue) with charge exchange forming neutral Uranium (Red) where some debris slips ahead of shock front. ....	92
Figure 35.	Simulation involving Uranium +1 (green) and Xenon +1 (red) into Oxygen +1 (blue) without charge exchange where debris couples into background. ....	93
Figure 36.	Simulation involving Uranium+1 (light blue) and Xenon+1 (red) into Oxygen+1 (blue) with charge exchange forming neutral Uranium (green) and neutral Xenon (gold) where some debris slips through the background. ...	94
Figure 37.	Simulation involving Uranium +1 (green) and Zirconium +1 (red) into Oxygen +1 (blue) without charge exchange where debris couples into background. ....	96
Figure 38.	Simulation involving Uranium +1 (Blue) and Zirconium +1 (Yellow) into Oxygen +1 (Blue) with charge exchange where some debris slips through the background. ....	97
Figure 39.	Simulation involving Uranium +1 (Green) and Lead +1 (red) into Oxygen +1 (Blue) without charge exchange where debris couples into background. ..	99
Figure 40.	Simulation involving Uranium +1 (Blue) and Lead +1 (Yellow) into Oxygen +1 (Blue) with charge exchange where debris slips through background. ....	100
Figure 41.	Graphic summary of simulations examining charge exchange. ....	106

THIS PAGE INTENTIONALLY LEFT BLANK

## LIST OF TABLES

Table 1.	List of simulations conducted to examine collision shock driven by multiple species.....	61
Table 2.	List of simulations conducted to examine charge exchange.....	63
Table 3.	Comparison of slip through data without and with charge exchange for uranium. ....	81
Table 4.	Comparison of slip through data for uranium and xenon without and with charge exchange in a constant atmosphere. ....	84
Table 5.	Comparison of slip through data without and with charge exchange for uranium and zirconium in a constant atmosphere.....	87
Table 6.	Comparison of slip through data without and with charge exchange for uranium and lead in a constant atmosphere. ....	90
Table 7.	Comparison of slip through data without and with charge exchange for uranium. ....	93
Table 8.	Comparison of slip through data without and with charge exchange for uranium and xenon.....	95
Table 9.	Comparison of slip through data without and with charge exchange for uranium and xenon.....	98
Table 10.	Comparison of slip through data without and with charge exchange for uranium and lead.....	101

THIS PAGE INTENTIONALLY LEFT BLANK

## LIST OF ACRONYMS AND ABBREVIATIONS

1-D	One Dimensional
3-D	Three Dimensional
CMHD	Collisionless magnetohydrodynamics
DOD	Department Of Defense
eV	electron-volt
HANE	High-Altitude Nuclear Explosion
LLNL	Lawrence Livermore National Laboratory
LTBT	Limited Test Ban Treaty
KIM3D	Kinetic Ion Model, 3 Dimensional
km	kilometer
MHD	Magneto-Hydrodynamics
MT	Mega-Ton
NASA	National Aeronautics and Space Administration
PIC	Particle-In-Cell
RPPSP	real particles per simulation particle

THIS PAGE INTENTIONALLY LEFT BLANK

## ACKNOWLEDGMENTS

The author would like to thank the professionals at Lawrence Livermore National Laboratory for all the support throughout this work. Special thanks goes to Dr. Dennis Hewett for all his mentoring and encouragement. This would not be possible without his tremendous effort. Even today, I am learning and understanding things from what he taught me. He was a great scientist and tremendous mentor. His patience and commitment to my education is a special gift. I would also like to thank Dr. David Larson for his keen insight and coaching. I would also like to thank COL Chris Cross for forcing me to work at a higher level and asking the tough and obvious questions I had overlooked. I would like to thank the whole Physics Department of NPS for all the support over the years, and I would like to single out Professor Craig Smith, my staunchest supporter and wisest counselor. I am grateful to Professors Bill Colson, Jim Luscombe and Todd Weatherford for supporting me on this endeavor. I recognize the time and effort all have sacrificed to get me to this point. Most importantly, I would like to thank my gracious wife and daughter for supporting me throughout this whole process. This would not have been possible without their love, support and understanding. I owe them both so very much.

THIS PAGE INTENTIONALLY LEFT BLANK



# **I. INTRODUCTION**

## **A. INTRODUCTION**

STARFISH PRIME (hereafter referred to as STARFISH) was a high-altitude nuclear explosion (HANE) conducted by the United States (U.S.) on 9 July 1962. While the explosion occurred at 400 kilometers (km) above the Earth's surface, satellites measured high-energy fission-spectrum electrons at locations (elevations) and corresponding magnetic field lines well above what analysts have been able to explain. Bomb debris from STARFISH was composed of fission products, other ionized materials, and electrons, some born from beta decay of fission fragments. Charged particles moving in the presence of the existing magnetic field of the Earth will gyrate around the field lines. The binding of these charged particles to the field lines limits how far charged particles will travel in the direction perpendicular to the field lines. That is part of the mystery observed with the STARFISH test; the question of how ions and electrons were transported to higher field lines has not been fully explained by analyses using simulations relying on fluid-based principles suggesting that kinetic effects and other physical processes must be incorporated to develop a full description of the test.

The measured energetic electrons from STARFISH are more than just a scientific curiosity. Electrons and ions from a HANE can be expected to collide with satellites and the resulting accumulation of damage can result in a corresponding increase in failure rates (i.e., a reduction in the mean-time-to-failure). Following STARFISH, three satellites quickly failed and another two failed well before their predicted lifetimes. The dramatic increase in the number and importance of military as well as civilian satellites from 1962 to the present underscores how critical this effect can be to the Department of Defense (DOD) and to the Nation.

In addition to the anomalous distribution of debris, the energy of STARFISH “dragged” the Earth's magnetic field lines outward and created a diamagnetic cavity or

“bubble.”<sup>1</sup> In such a bubble, the magnetic field strength is well below that of the ambient field, and in this region charged particles will experience a reduced level of turning and binding to the magnetic field lines. Therefore, charged particles in a diamagnetic cavity will travel in a generally straight line until they depart the bubble. However, the diamagnetic cavity observed in STARFISH was not large enough to fully explain the spatial distribution of energetic electrons measured.<sup>2</sup> Additionally, attenuation of the cosmic background radio waves gives insight to ionization of the atmosphere. There were differences in the attenuation data when compared from collection stations in Alaska to collection stations in Canada and Norway leading researches to conclude “that upward-traveling debris from the explosion managed to work its way through the Earth’s magnetic field vertically overhead of Johnston Island.”<sup>3</sup>

Fission of an actinide generally produces two ionized fission fragments. These fission fragments are highly ionized; the process of fission injects both positive ions and negative electrons into the background plasma. Additionally, these fission fragments are normally neutron rich and decrease their internal (nuclear) energy by beta decay. Generally a fission fragment undergoes several beta decays before becoming a stable isotope.<sup>4</sup> These beta decays are a source of energetic electrons. It is unknown where the energetic electrons measured after STARFISH came from; however, one possible explanation (based on the measured energy spectrum and the fact that they were not present before the detonation) is they were from the beta decays of fission fragments that had been somehow transported to much higher altitudes than their point of generation.

This work considers two physical processes as possible explanations for the presence of the large number of energetic electrons at field lines above where they were expected. The two processes explored here are a multispecies collisionless shock and

---

<sup>1</sup> Palmer Dyal, “Particle and Field Measurements of the STARFISH Diamagnetic Cavity,” *Journal of Geophysical Research* 111 (2006): 1.

<sup>2</sup> Ibid., 13.

<sup>3</sup> R.P Balser, R.B. Dyce and H. Leinback. “High-Latitude Ionization Associated with the July 9 Explosion,” *Journal of Geophysical Research* 68 (1963): 741.

<sup>4</sup> K.Krane. *Introductory Nuclear Physics* (New York: John Wiley & Sons, 1988), 485.

collisional charge exchange. A collisionless shock occurs when the expanding plasma generates an electric field of large enough intensity to rapidly accelerate (shock) the background plasma. When the expanding plasma consists of more than a single ionic constituent, it is called multispecies. Is it possible a debris species with a small gyro-radius would form a collisionless shock that would subsequently accelerate other species with larger gyro-radii? Charge exchange is the process where one (or more) electron(s) is exchanged between atoms. The change in charge state affects how the ion's trajectory bends in the magnetic field. Neutral atoms' trajectories do not bend in the magnetic field and, they travel in a straight line until a collision diverts their path. Could this process explain the electron population further from the blast point and across many magnetic field lines? Those two questions are addressed in this work.

These two processes were modeled using a cylindrical geometry code called ZMR. ZMR was initially developed (and subsequently updated) at Lawrence Livermore National Laboratory (LLNL) 30 years ago and has been used to simulate various plasma phenomenologies principally in cases where the motion of the ions was important but the detailed electron dynamics do not influence the phenomena of interest.<sup>5</sup> This situation arises when the Debye length is small compared to the ion gyro-radius, so the quasi-neutral assumption is valid and the electron inertial length is much smaller than the ion inertial length.<sup>6</sup> This dissertation research expanded upon the multispecies investigation began by Hewett and then added a capability to examine charge exchange. This work is computational in nature and relies on simulation to provide insight into physical processes. Understanding these two processes in a basic one-dimensional (1-D) geometry will help in the analysis of their importance and may lead to their incorporation into more robust future simulations. That is the goal of this work. This research is not intended to provide a full reproduction the STARFISH data set. However, this work is a preliminary

---

<sup>5</sup> D.W. Hewett. "A Global Method of Solving the Electron-Field Equations in a Zero-Inertia-Electron-Hybrid Plasma Simulation Code," *J. Comp. Phys.* 38 (1980) 378–395.

<sup>6</sup> G.F. Simonson, D.W. Hewett, D.E. Shumaker, D.V. Anderson, J.A. Byers and G.DiPeso. "Numerical Simulation of Interactions of Nuclear Weapons with the Geomagnetic Field," UCRL-JC-109841: Sensor Technical Conference (1992), 5.

investigation of relevant physical hypotheses that could account for observed anomalies. From this work, it will be possible to integrate and test the developed computational methods into larger and more robust HANE simulation codes.

LLNL, other national laboratories and the DOD have been studying STARFISH since 1962 and attempting to explain the results. The limited number of high altitude tests and the limited data from each test hinder the community's overall understanding of the complex problem. Simulation models will increase in complexity and fidelity as computing power increases. Original codes used magneto-hydrodynamics (MHD)-based modeling where the plasma was treated as a charged fluid where the rules of fluid dynamics are combined with the rules of electricity and magnetism. Subsequent increases in computing power allowed the use of the Particle-In-Cell (PIC) method. PIC codes are used when the assumption of a Maxwellian velocity distribution is inadequate to describe the plasma.<sup>7</sup> At the altitude of STARFISH, the mean free path of the debris ions in the thin atmosphere is too large to use a MHD code.<sup>8</sup> ZMR is a PIC code with an implicit field solver<sup>9</sup> and it provides better resolution for the spatial motion of the ions than an MHD code.

## **B. PREVIOUS WORK IN THIS FIELD**

Since 1962 there have been many varied efforts to explain the STARFISH test. The *Journal of Geophysical Research* dedicated its whole 68th volume to the analysis and presentation of the data. The editors stated in the introduction that, “a central purpose of this introduction is to call attention to the fact that there still exists a lack of agreement on the spatial extent of the STARFISH radiation belt and on the total number of trapped particles therein.”<sup>10</sup> The journal devoted that issue to the efforts of various authors and

---

<sup>7</sup> E.C. Whipple Jr. “A kinetic approach to magnetospheric modeling,” *Quantitative Modeling of Magnetospheric Processes* (American Geophysical Union: Washington, DC, 1979), 463.

<sup>8</sup> T.G. Cowling, *Magnetohydrodynamics* (Bristol UK: Adam Hilger, 1976): 120.

<sup>9</sup> D.W. Hewett, Documentation of the EM 2.5D Quasi-neutral Hybrid Code ZEMER, 10.

<sup>10</sup> W.L. Brown, W.N. Hess and J.A. Van Allen, “Collected Papers of the Artificial Radiation Belt from the July 9, 1962, Nuclear Detonation,” *Journal of Geophysical Research* 68 (1 February 1963): 605.

institutes to capture, analyze and present the data on the introduced radiation measured following STARFISH.

The *Trapped Radiation Handbook* was originally compiled in 1971 for the Defense Nuclear Agency and was revised several times in the intervening years. Originally designed as a single source for satellite proponents to understand the trapped radiation environment, it evolved into a repository of derivations and facts related to charged particles in the Earth's magnetic field.<sup>11</sup> The handbook provided facts and data about trapped radiation but did not attempt to establish from first principles how the artificial radiation became trapped in the radiation belts. While the experts have laid out possible mechanisms, none were conclusively examined.<sup>12</sup>

In 1978, Kilb and Glenn employed a collisionless magneto-hydrodynamic (CMHD) simulation that included charge exchange for the atmospheric ions.<sup>13</sup> For STARFISH and the relatively low density of the atmosphere, the authors claimed the fluid equations of MHD did not produce the observed results.<sup>14</sup> However, the authors use a CMHD model below the burst to specifically look at the formation of a low altitude ion patch.<sup>15</sup> Additionally, their modeling employed charge exchange but only for the atmospheric constituents of oxygen and nitrogen; the debris ions were not modeled in the CMHD simulation.<sup>16</sup> In the simulation, the atmospheric ions were neutralized and then moved in a straight line across magnetic field lines. At a later time, the neutral air atoms were re-ionized to form the ion patch.<sup>17</sup> The modeling results appeared to conserve energy.<sup>18</sup> The model focused on the total amount and spectra of the ultraviolet radiation

---

<sup>11</sup> *Trapped Radiation Handbook*.

<sup>12</sup> Ibid

<sup>13</sup> R.W. Kilb, and D.E. Glenn. *CMHD Simulations of very high altitude nuclear bursts from 0 to 1 second (U)* (Santa Barbara: Mission Research Corporation, 1978), 17

<sup>14</sup> Ibid., 17.

<sup>15</sup> Ibid., 17.

<sup>16</sup> Ibid., 38.

<sup>17</sup> Ibid., 37.

<sup>18</sup> Ibid., 61–62.

generated<sup>19</sup> and not the spatial distribution of the debris. The choice of a CMHD model prevented the investigation of collisionless shock as this is a kinetic ion driven process. Additionally, Kilb and Glenn focused on charge exchange for constituents of the atmosphere only and did not examine the debris ions. As will be discussed in Chapter II.C, the debris ions likely undergo several beta decays and eject high-energy electrons, which contribute to the electron population measured following STARFISH.

LLNL published simulations using a 3D hybrid particle code originally designed for theta pinch plasma.<sup>20</sup> Shumaker used a 3D hybrid code called QN3D for 3D simulations of a single debris species expanding into a background plasma. The objective of that research involved investigation of the formation of the diamagnetic cavity.<sup>21</sup> Additionally, by collapsing a spatial dimension, the code produced 2D results for the study of longer time kinetic effects.<sup>22</sup> However, the code required long run times with only a single debris species<sup>23</sup> and is no longer in use at LLNL.

The review of the literature did not identify any work that examined either collisionless shock driven by multiple ion species or charge exchange as processes to move debris ions across magnetic field lines. These debris ions would be the source of high-energy electrons by beta decay. Additionally, these processes may be important to other simulation work at LLNL and elsewhere.

### **C. RESEARCH OBJECTIVES AND METHODOLOGY**

This research in this dissertation focused on two physical processes—collisionless shock driven by multiple ion species and charge exchange. These processes were examined in relation to the debris from a HANE expanding into the Earth’s ambient magnetic field and upper atmosphere. They were examined to judge their relative impact

---

<sup>19</sup> Ibid., 58.

<sup>20</sup> E. Shumaker, D.V. Anderson and G.F. Simonson, “3D and 2D Simulations of an Expanding Plasma Using a Darwin Hybrid Particle Code.” UCRL-ID-109852: LLNL: 1.

<sup>21</sup> Ibid. 10.

<sup>22</sup> Ibid. 1.

<sup>23</sup> Ibid. 12.

on the spatial distribution of the debris following a HANE. This work focused on the debris from a HANE since the debris is a source of high-energy upon electrons following beta decay. High-energy electrons were measured far across the Earth's magnetic field lines following a high altitude nuclear test. These high-energy electrons can impact on satellites and damage their electronics, thereby decreasing the mean-time-to-failure. The U.S. Government relies heavily on satellites, especially during a crisis. Our continued reliance on satellites makes us vulnerable to the effects of a high altitude nuclear explosion. Any improvement in our ability to model and forecast the spatial distribution of high-energy electrons following a HANE will increase our ability to protect and operate our vital satellite fleet.

The method of examination consisted of simulation using a one dimensional hybrid plasma code described in detail in Chapter VI. Simulations were performed in simple radial geometry (on a faster running code than a full three dimensional code) to develop an understanding of the importance of the two processes. If either or both processes are judged to contribute to the population of high-energy electrons beyond what has been previously predicted, then those processes should be included in a higher fidelity simulation.

The flow of the dissertation begins with an overview of the primary physics topics that are required for this research. The physical details of the STARFISH PRIME nuclear test are presented. Then the mechanics of collisionless shock formation are derived, and an overview of collisional charge exchange is provided. The final piece of background is an overview of the hybrid plasma code ZMR as well as a discussion of the modifications made to the code for this work. Finally, the results and conclusions from the research are provided and their implications discussed.

THIS PAGE INTENTIONALLY LEFT BLANK



## II. BACKGROUND PHYSICS

This chapter explains in more detail some of the background physics required for this work. Readers with a thorough understanding of the Earth's magnetic field, motion of a charged particle in a constant magnetic field and nuclear fission can skip ahead to Chapter III. This chapter provides a brief overview of those three topics as background to assist in understanding the remainder of the work.

### A. L-SHELL MODEL OF EARTH'S MAGNETIC FIELD

The Earth's magnetic field resembles a simple dipole field and is frequently modeled as such. In a dipole magnetic field, there are two opposite poles with magnetic field lines that follow a curved path between them. Figure 1 is a sketch of the standard dipole representation of the Earth's magnetic field. A slight complication in the representation is that the southern magnetic pole is in the Earth's northern hemisphere.<sup>24</sup>

Transferring this dipole model of the Earth's magnetic field into a mathematically usable form for modeling and simulation requires its representation in an appropriate coordinate system. For modeling the Earth's field, either a Cartesian or a spherical coordinate system could work; however, each of these representations has its own challenges. The Cartesian coordinates system is mathematically easier to work with for vector equations. However, the Cartesian system is cumbersome and intuitively difficult when used to describe locations in a spherical frame of reference. The spherical coordinate system has a more appropriate geometry for the Earth's magnetic field but is cumbersome to work with mathematically. Also, the spherical coordinate system has a simpler description for the distance of a point from the center of the system, but a more difficult description for the distance between two points in space.

McIlwain proposed labeling a drift shell, which is a constant magnetic field line rotated around the dipole, by two parameters. He used  $B_m$  as the scalar value of the

---

<sup>24</sup> J.W. Chamberlain *On Motion of Charged Particles in the Earth's Magnetic Field* (New York: Gordon and Breach, 1964), 2.

magnetic field at the mirror point and  $L$ , which is generally the number of Earth radii measured at the magnetic equator of the dipole.<sup>25</sup> More specifically

$$L = \frac{r}{R_e \sin^2 \theta} \quad (1)$$

where  $r$  is the radial distance from the center of the Earth,  $R_e$  is the radius of the Earth and  $\theta$  is the angle measured down from the pole of the dipole. While this system was originally designed to eliminate the need for a numerical solution to a differential equation, the system has continued to be used broadly by researchers studying space.<sup>26</sup> The L-shell method is used in much of the literature describing STARFISH's post detonation data collection.

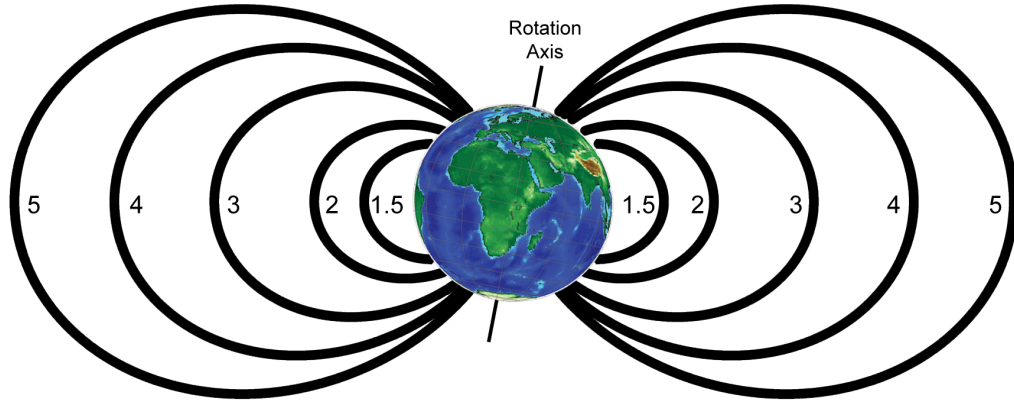


Figure 1. Simple drawing of Earth's L-Shell organization and general sketch of a magnetic dipole field.

<sup>25</sup> Carl E. McIlwain, "Coordinates for Mapping the Distribution of Magnetically Trapped Particles," *Journal of Geophysical Research* 66 (1961): 3681.

<sup>26</sup> M. Schulz, "Canonical Coordinates for Radiation-Belt Modeling," *Geophysical Monograph*, (1996): 157.

## B. MOTION OF A CHARGED PARTICLE IN A CONSTANT MAGNETIC FIELD

The motion of a charged particle subjected to electric and magnetic fields begins with a description of the Lorentz force

$$\vec{F} = m \frac{d\vec{v}}{dt} = q \left( \vec{E} + \vec{v} \times \frac{\vec{B}}{c} \right) \quad (2)$$

where  $m$  is the mass of the particle,  $t$  is the time element,  $q$  is the charge state of the charged particle,  $E$  is the electric field,  $v$  is the velocity of the particle,  $B$  is the magnetic field and  $c$  is the speed of light in a vacuum.<sup>27</sup>

Assuming there is no electric field this becomes

$$\frac{d\vec{v}}{dt} = \frac{q}{m} \left( \vec{v} \times \frac{\vec{B}}{c} \right) \quad (3)$$

Further assuming that the local magnetic field exists only in the  $z$  direction of the Cartesian coordinate system, this becomes

$$\frac{dv_x}{dt} = \frac{q}{mc} v_y B_z \quad (4)$$

$$\frac{dv_y}{dt} = \frac{-q}{mc} v_x B_z \quad (5)$$

$$\frac{dv_z}{dt} = 0 \quad (6)$$

Thus, the velocity in the  $z$  direction is constant. Since there is no electric field and the magnetic field does not change the energy of the charged particle, the initial  $z$  component of the velocity is unchanged. Taking another time derivative of equations 4 and 5 and

---

<sup>27</sup> J.D. Jackson. *Classical Electrodynamics* (Hoboken NJ : John Wiley & Sons, 1999), 553.

combining with the first derivatives of equations 5 and 4 respectively, the differential equations become

$$\frac{d^2 v_x}{dt^2} = \frac{qB_z}{mc} \frac{dv_y}{dt} = -\left(\frac{qB_z}{mc}\right)^2 v_x \quad (7)$$

$$\frac{d^2 v_y}{dt^2} = -\frac{qB_z}{mc} \frac{dv_x}{dt} = -\left(\frac{qB_z}{mc}\right)^2 v_y \quad (8)$$

These equations have the standard solutions of

$$v_x(t) = C_1 \sin\left(\frac{qB_z}{mc}t + \delta_1\right) \quad (9)$$

$$v_y(t) = C_2 \sin\left(\frac{qB_z}{mc}t + \delta_2\right) \quad (10)$$

$C$  and  $\delta$  are constants of the integration and do not affect the geometric nature of the motion; they do have particular values for a given set of initial conditions of the charged particle. Therefore, the resulting solutions to the vector component equations of motion for a charged particle in magnetic field generate helical motion along the lines of magnetic force. It is important to note that the presence of a magnetic field does not impact the component of motion of the charged particle parallel to the magnetic field (assumed to be in the  $z$  direction for this explanation). The term modifying the time component in equations 9 and 10 is defined as the cyclotron frequency,  $\omega_c$ .

$$\omega_c \equiv \frac{qB}{mc} \quad (11)$$

The constant of integration  $C$  is the component of the velocity in the plane perpendicular to the magnetic field. This has the symbol  $v_\perp$ . In this example, the magnetic field is in the  $z$  direction so  $v_\perp$  resides in the  $x$ - $y$  plane. Integrating equations 9 and 10 again, the equations for the positions in  $x$  and  $y$  become

$$x = x_o + v_{\perp} \frac{mc}{qB} \cos(\omega_c t + \delta_1) \quad \text{and} \quad (12)$$

$$y = y_o + v_{\perp} \frac{mc}{qB} \cos(\omega_c t + \delta_1) \quad (13)$$

The term modifying the trigonometry functions above is defined to be the Larmor radius,  $r_L$ .

$$r_L \equiv \frac{mc v_{\perp}}{qB} \quad (14)$$

The Larmor radius describes the perpendicular radius of the helical motion of the charged particle.<sup>28</sup> For a constant initial particle velocity and magnetic field, the ratio of mass to charge state determines the Larmor radius. The Larmor radius helps describe how the path of a charged particle turns while moving through a magnetic field.

### C. MOTION OF A CHARGED PARTICLE IN A DYNAMIC MAGNETIC FIELD

In addition to the above-described helical motion of charged particles bound to magnetic field lines, the phenomenon of drift also occurs. There are many physical causes for such drifts and they include the presence of an electric field, non-uniformity (i.e., curvature and gradient) of the magnetic field and the time variability of the magnetic field.<sup>29</sup> Charged particles with opposite charges drift in opposite directions. The motion of ions is explicitly simulated in the ZMR code, so all the relevant drift motions are accounted for.

---

<sup>28</sup> Francis Chen. *Introduction to Plasma Physics and Controlled Fusion* (New York: Springer, 2006), 20.

<sup>29</sup> Ibid., 43.

Figure 2 shows the motion of a charged particle bound to a magnetic field line on the Earth. The particle has a helical motion as it travels up and down the field line. There are no non-conservative forces, so the particle does not gain or lose energy. The portion of the velocity that is perpendicular to the magnetic field is a minimum at the magnetic equator, where the field strength is lowest, and increases to 100% at the ends the helical path where the field strength is highest. The end points are called the mirror points. The whole helical path of the charged particle then drifts according to the parameters of the fields and any forces. Figure 2 shows the helical path of the charged particle between the mirror points as well as the drifting of the whole helical path.

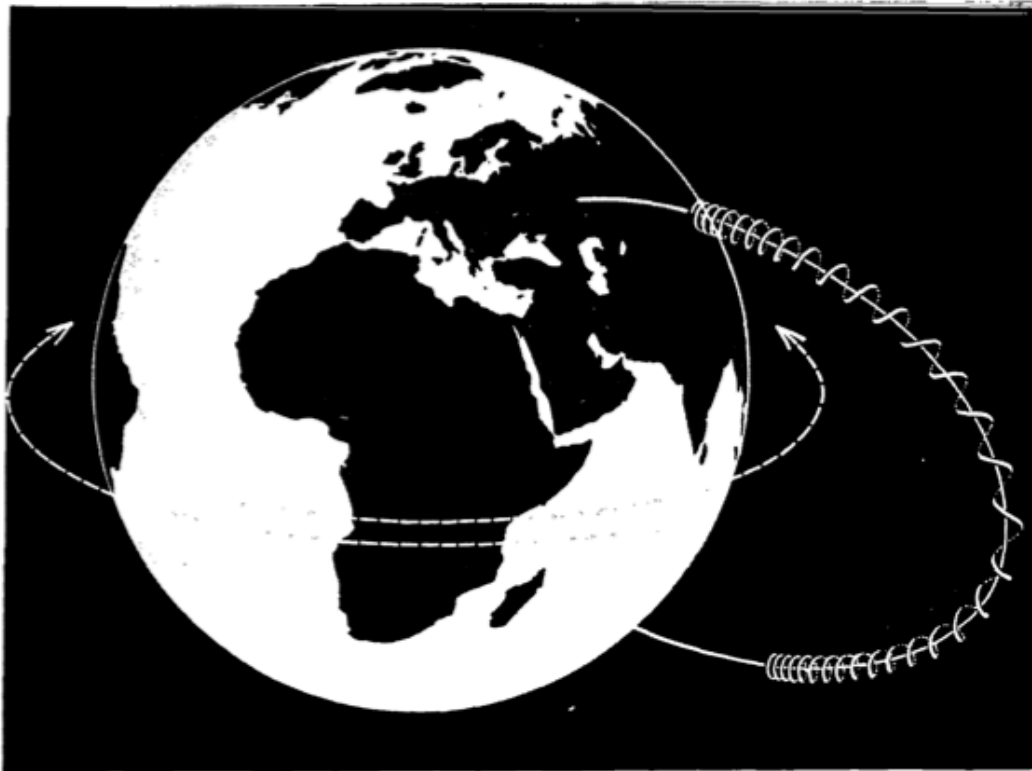


Figure 2. Motion of a charged particle in the Earth's dipole magnetic field (after Hess, 1964).

Absent any input or outflow of energy, the charged particle will maintain this helical, drifting motion. There are adiabatic invariants for the motion of charged particles around the lines of magnetic field as well as along the line of magnetic field and the drift

motion perpendicular to the magnetic field.<sup>30</sup> The adiabatic invariants are well documented and can be solved explicitly. The importance of the adiabatic invariants comes from the ability to predict the motion of charged particles as long as the conditions remain constant. In such cases, the charged particles will stay bound to the magnetic field. A HANE release a large amount of energy in a short time and a compact space, and the subsequent additional energy release (e.g., from beta decay of fission fragments) is very small in relation. Thus, there is no mechanism to input significant additional energy into the plasma to change the adiabatic invariants.<sup>31</sup>

#### **D. OVERVIEW OF FISSION**

Fission is a nuclear process where a nucleus splits into two or more smaller nuclei with an associated release of energy. Fission is normally triggered when a nucleus (commonly uranium-235 or plutonium-239) absorbs a neutron and forms a compound nucleus. That compound nucleus is unstable and splits into two or more fission fragments, although statistically the probability of three fission fragments is small (1 in 300).<sup>32</sup> The sum of the masses of these fission fragments is less than the original mass of the parent compound nucleus and the missing mass is released as energy on the order of 200 mega-electron-volts (MeV) per fission.<sup>33</sup>

The two (or more) fission fragments released from each fission reaction do not have specified atomic or mass numbers. Rather, they follow a bimodal statistical distribution based on mass numbers of the two fragments. Based on the distribution, the products are referred to as the light group with mass number between 80–110 and the heavy group with mass number between 130 and 155. The distribution of the mass of the

---

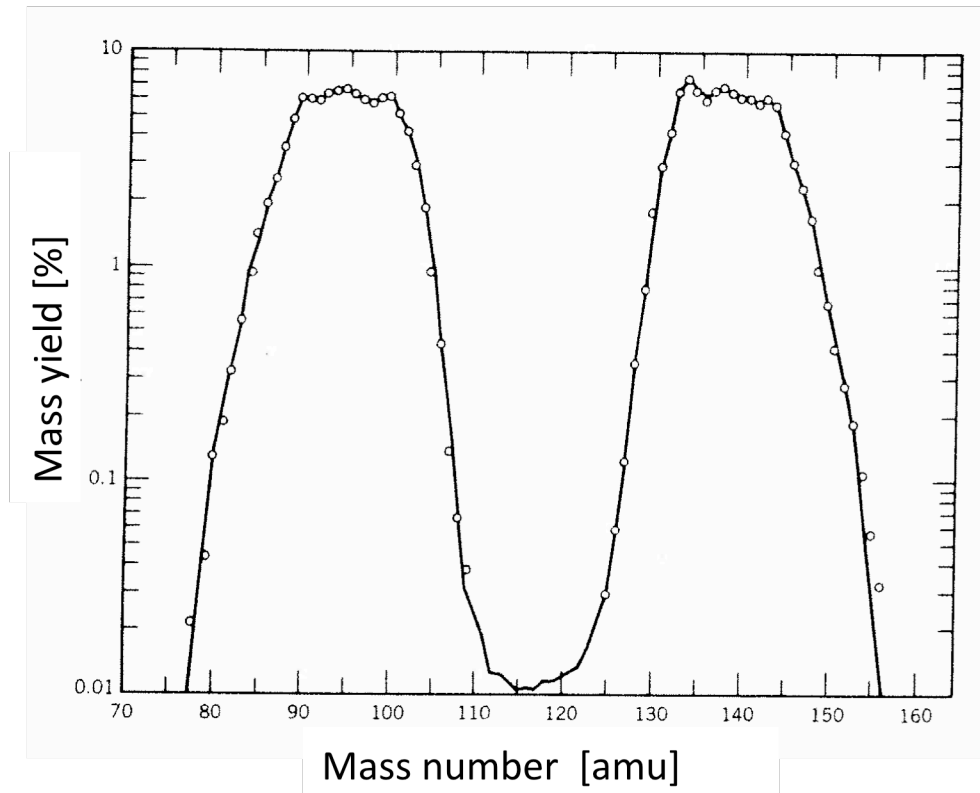
<sup>30</sup> George Parks, *Physics of Space Plasmas, An Introduction*, 2nd ed. (Boulder: Westview Press, 2004), 135.

<sup>31</sup> Charles Bridgman, *Introduction to the Physics of Nuclear Weapons Effects* (Wright Patterson AF Base: Defense Threat Reduction Agency, 2001), 77.

<sup>32</sup> H.D. Bush. *Atomic and Nuclear Physics: Theoretical Principles* (Englewood Cliffs: Prentice-Hall Inc, 1962), 136.

<sup>33</sup> Charles Bridgman, *Introduction to the Physics of Nuclear Weapons Effects* (Wright Patterson AF Base: Defense Threat Reduction Agency, 2001), 77.

fission fragments for fission of uranium-235 is shown in Figure 3. The distribution for fission of plutonium-239 is similar. Regardless if the parent nucleus is uranium or plutonium, both the fission fragments have excess neutron-to-proton ratios and therefore frequently seek a more stable nuclear state by one or more beta decays. Beta decay converts a neutron into a proton and releases an electron of variable energy.<sup>34</sup> The half-life for beta decay varies by isotope and can range from milli-seconds to years (with tens of years being the most abundant). Around 4% of the total energy released from fission occurs from the beta decay of the fission fragments.<sup>35</sup> This research considers mechanisms by which fission fragments can be transported to higher L-shells where their subsequent beta decay will introduce high-energy electrons that may account for otherwise unexplained anomalous radiation levels.



<sup>34</sup> H.D. Bush. *Atomic and Nuclear Physics: Theoretical Principles* (Englewood Cliffs: Prentice-Hall Inc, 1962), 137.

<sup>35</sup> Charles Bridgman. *Introduction to the Physics of Nuclear Weapons Effects* (Wright Patterson AF Base: Defense Threat Reduction Agency, 2001), 77.



Figure 3. Distribution of mass of fission fragments from the fission of uranium-235 by a thermal neutron (after Krane, 1988)

The energy spectrum of the electrons released following the fission of uranium-235 was experimentally measured and fits the distribution

$$Y = 3.88 \exp[-0.575E - 0.055E^2] \quad (15)$$

where Y is the distribution [electrons per fission per MeV] and E is the electron energy [MeV]; formula 15 is valid for  $E < 7$  MeV.<sup>36</sup> Energy dependent detectors allow the comparison of sampled electrons to the distribution of equation 15 and a determination of the fit of the measured spectrum to the experimentally derived spectrum of electron energy from beta decay.

A nuclear explosion consists of a very large number of atoms undergoing fission releasing a corresponding amount of energy in a very short amount of time. The total energy released will raise the temperature at the point of the explosion to tens of millions of degrees Fahrenheit.<sup>37</sup> The high temperatures achieved by a nuclear explosive detonation will cause a high degree of ionization of the resulting debris. The ionized debris will consist of both positive ions and free electrons. However, these initial ions and free electrons will be bound to the Earth's magnetic field lines as they stream away from the burst point. Even the creation of a diamagnetic bubble (as described in the next chapter) does not explain the movement of the ionized fission fragments and their electrons to elevations observed in STARFISH. Therefore, the initial production of electrons is not believed to be the source of the high L-shell electrons. The beta decay of the fission fragments and the electrons released from those decays are hypothesized to be the main source of the high-energy electrons. This research focused on the spatial distribution of the fission fragments as the source of high-energy electrons.

---

<sup>36</sup> J.A. Van Allen, L.A. Frank and B.J. O'Brien, "Satellite Observations of the Artificial Radiation Belt of July 1962," *Journal of Geophysical Research* 68 (1963): 620.

<sup>37</sup> S Glasstone and P.J. Dolan. *The Effects of Nuclear Weapons* (Washington, DC: Department of the Army DA Pamphlet No 50-3, 1977), 27.

THIS PAGE INTENTIONALLY LEFT BLANK

### III. THE STARFISH PRIME TEST

#### A. PHYSICAL SETTING

The STARFISH test occurred on 9 July 1962 at 0900 hours ZULU (Greenwich Mean Time), which was 2300 hours in Hawaii. The test occurred at 16.7° N latitude and 190.5° E longitude (roughly above Johnson Atoll) at an altitude of 400 km.<sup>38</sup> This test was conducted prior to the implementation of the Limited Test Ban Treaty (LTBT) so at that time, atmospheric testing was not prohibited by treaty or international law. The announced yield of STARFISH was 1.4 MegaTons (MT). Most other design details of the device remain classified.

At 400 km above the Earth's surface, the nighttime atmosphere above Johnston Atoll consists predominantly of atomic oxygen. NASA data for the neutral elements in the standard atmosphere at nighttime above Johnson Atoll is shown in Figure 4. Ionized monatomic oxygen is initially two orders of magnitude less than neutral oxygen; however, the prompt gamma and x-ray energy released in the detonation of a HANE would ionize the constituents of the atmosphere in the vicinity of the explosion (out to 10s of kilometers). While many gases contribute to the atmospheric composition at 400 km, monatomic oxygen is more abundant than other constituents by an order of magnitude. Therefore, monatomic oxygen is considered to be representative of the background gas for the work in this dissertation.

---

<sup>38</sup> J.A. Van Allen, L.A. Frank and B.J. O'Brien, "Satellite Observations of the Artificial Radiation Belt of July 1962." *Journal of Geophysical Research* 68 (1963): 619.

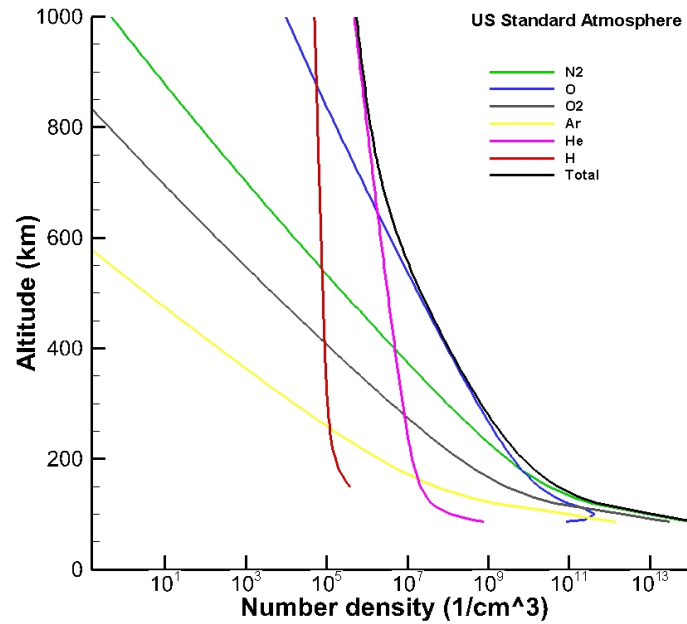


Figure 4. Number density of gaseous components of nighttime atmosphere above Johnston Atoll as a function of altitude (after Larson, 2011)

## B. MAGNETIC BUBBLE OBSERVATIONS

The Earth's magnetic field is similar to an offset, tilted dipole field. It has a dipole shape with the southern pole of the field occurring in the Earth's northern hemisphere and the northern pole in the southern hemisphere. Both magnetic poles are offset from the respective geographic poles of the rotating Earth. The nominal value of the magnetic field is 0.3 Gauss at the surface and decreases with distance further out from the center of the Earth's surface.

The STARFISH test employed 27 sensor-equipped rockets travelling at different routes to collect pictures and data. Some of these rockets collected data on the magnetic field strength.<sup>39</sup> The data from both particle counters and magnetometers showed that the explosion formed a diamagnetic cavity around the burst point. This asymmetrical cavity's

<sup>39</sup> "A 'Quick Look' At the Technical Results of STARFISH PRIME," 6.

expansion and collapse occurred in about 16 seconds.<sup>40</sup> This magnetic bubble is a volume of space where the measured magnetic field is less than the ambient magnetic field. As the Larmor radius of particle motion is a function of magnetic field strength, the weaker magnetic field in the bubble causes a larger Larmor, radius and hence ionized particles travel in a straighter, less curved path while traveling through the magnetic bubble. Figure 5 illustrates the rocket trajectories and the time period during which data was collected is shaded with red.

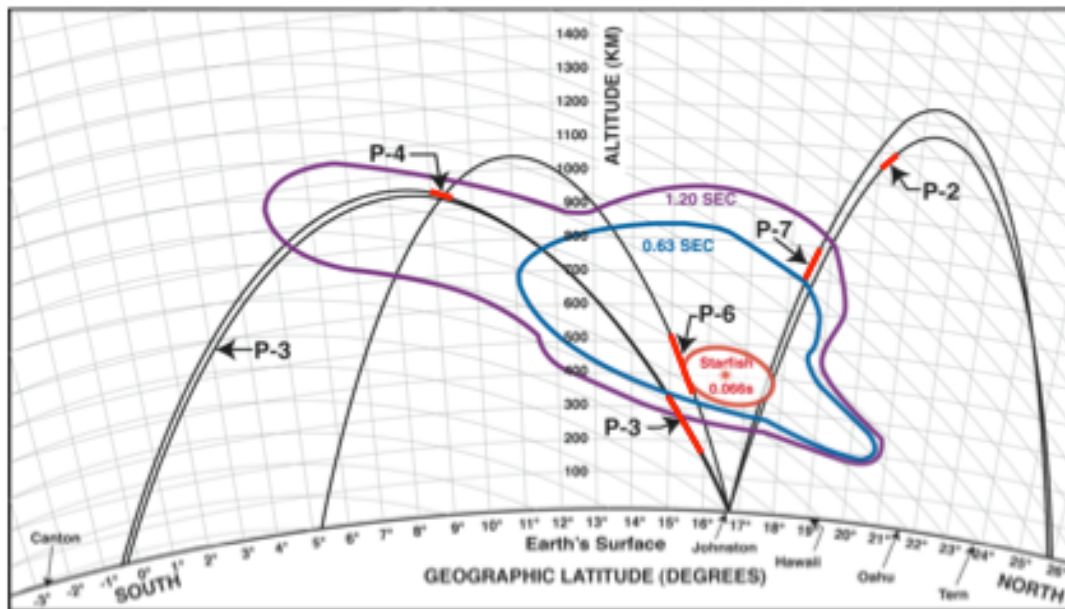


Figure 5. Time dependent size of diamagnetic cavity produced by STARFISH detonation with flight path of instrumented rockets superimposed showing times instruments were collecting data (after Dyal, 2006)

### C. OBSERVED BELT PUMPING

The STARFISH test was centered on  $L=1.12$ .<sup>41</sup> The resulting magnetic bubble (described in the previous section) stretched the Earth's magnetic field lines and allowed

<sup>40</sup> Palmer Dyal, "Particle and Field Measurements of the STARFISH Diamagnetic Cavity," *Journal of Geophysical Research* 111 (2006): 1.

<sup>41</sup> J.A. Van Allen, L.A. Frank and B.J. O'Brien, "Satellite Observations of the Artificial Radiation Belt of July 1962," *Journal of Geophysical Research* 68 (1963): 619.

the ionized weapon debris to travel in straighter lines under kinetic motion to the edge of the bubble. Upon leaving the magnetic bubble, the debris would have re-entered the Earth's unperturbed magnetic field and continued to travel as specified under the Lorentz force equation of motion. The magnetic bubble would place the ions a Larmor radius length beyond the edge of the bubble where they would resume their helical path along the magnetic field lines as previously described.

The United States had several satellites with limited data collection capabilities in orbit at the time of, or immediately following, the STARFISH test. These included the Injun, Telstar, Ariel and Traac satellites. They all had different instrumentation and orbital paths, so there is not a common set of data. Complicating the data comparison, the Telestar satellite was launched one day after STARFISH on 10 July 1962.<sup>42</sup> Therefore, there is no pre-blast data from Telestar to compare to the measurements taken post-blast.

Nevertheless, all satellites reported an increase in the flux of energetic electrons and this flux deposited energy into the satellites. The energy from these electrons affected the electronics and resulted in failures. Ariel failed within three days and Traac failed within 36 days.<sup>43</sup> An energetic electron impacting on a silicon-based semiconductor can release large numbers of secondary electrons and the corresponding deposition of energy can result in damage to the electronic structure and/or memory failures. Advances in electronic technology make modern satellites even more vulnerable to upset or destruction than technology from 1962.<sup>44</sup>

The trapped particle data obtained underwent significant scientific peer review and publication. The highest electron flux measured was  $1 \times 10^8$  [electrons/(cm<sup>2</sup> sec)] at L=1.20.<sup>45</sup> This peak flux fell to around  $1 \times 10^7$  [electrons/(cm<sup>2</sup> sec)] at L=1.8 and  $1 \times 10^6$

---

<sup>42</sup> J.A. Van Allen, L.A. Frank and B.J. O'Brien, "Satellite Observations of the Artificial Radiation Belt of July 1962," *Journal of Geophysical Research* 68 (1963): 622.

<sup>43</sup> Hess, W.H., "The Artificial Radiation Belt Made on July 9, 1962," *Journal of Geophysical Research* 68 (1963): 667.

<sup>44</sup> Herman Hoerlin. *United States High-Altitude Test Experiences*, (Los Alamos: LA-6405, 1976) 31.

<sup>45</sup> Mozer *et al.*, "Preliminary Analysis of the Fluxes and Spectrums of Trapped Particles after the Nuclear Test of July 9, 1962" *Journal of Geophysical Research* 68 (1963): 648.

[electrons/(cm<sup>2</sup> sec)] at L=2.2.<sup>46</sup> While this last value is only 1% of the maximum measured value, it is an entire L-shell beyond the location of the detonation; at the magnetic equator that corresponds to a distance of 6400 km. Data from the satellite Ariel indicated that there were some high-energy electrons out to L-shells 5 or 6 but the fluxes at those distances are uncertain.<sup>47</sup> Explaining and modeling how the energetic electrons populated these outer belts remains a scientific challenge.

---

<sup>46</sup> W.L.Brown, W.N. Hess and J.A. Van Allen, "Introduction," *Journal of Geophysical Research* 68 (1963): 605.

<sup>47</sup> Ibid. 606.

THIS PAGE INTENTIONALLY LEFT BLANK



## IV. COLLISIONLESS SHOCK

### A. FORMATION OF COLLISIONLESS SHOCK

The first hypothesis considered was collisionless shock acceleration of the debris ions as a method to move them to higher L-shells in the Earth's magnetic field. With multiple species in the debris, the lighter species could drive the formation of the collisionless shock. As the heavier species passed through the shock front, it would accelerate and gain energy to move to a higher L-shell. After moving to that higher L-shell, the debris would undergo beta decay and inject high-energy electrons into the Earth's magnetic field and contribute to the data observed in STARFISH.

Following a HANE, the ionized debris streams outward from the point of detonation into the Earth's magnetic field. The mean free path for ion-ion collisions is large enough that collisions between the ions do not dominate the motion of the particles compared to the electromagnetic forces.<sup>48</sup> Collisionless shock is generated by the highly non-linear interactions of the expanding debris ions, the background plasma, and the electromagnetic fields. Ultimately an electric field interacts with the background plasma and is the mechanism to transfer energy from the debris ions to the background ions. Since the fields mediate the energy transfer instead of kinetic collisions, the process is called collisionless shock.

The initial fields and early-time response of the background plasma can be analyzed using the electron momentum equation with some simplifying assumptions. Starting with the electron momentum equation as annotated by Hewett, Larson and Brecht:

$$m_e n_e \frac{d\vec{u}_e}{dt} = en_e \vec{E} - \nabla P_e + \vec{J}_e \times \frac{\vec{B}}{c} \quad (16)$$

---

<sup>48</sup> R.T. Glassey and W.A. Strauss, "Absence of Shocks in an Initially Dilute Collisionless Plasma," *Communications in Mathematical Physics* 113, (1987): 1.

where  $m_e$  is the mass of the electron,  $n_e$  is the number density of the electrons,  $u_e$  is the velocity of the electron fluid,  $E$  is the electric field,  $P_e$  is the pressure,  $J_e$  is the electron current density,  $B$  is the magnetic field and  $c$  is the speed of light.<sup>49</sup> With the approximation that electrons have zero mass, the equation reduces to

$$0 = en_e \vec{E} - \nabla P_e + \vec{J}_e \times \frac{\vec{B}}{c} \quad (17)$$

In this non-relativistic scenario, the zero inertia assumption for electrons is an appropriate assumption based on the ratio of masses for electrons and nucleons (electrons account for 0.05% of the simulation mass). Re-arranging the equation to solve for  $E$  it becomes

$$\vec{E} = \frac{\nabla P_e}{en_e} - \frac{\vec{J}_e \times \vec{B}}{en_e c} \quad (18)$$

Then the Darwin approximation for Ampere's law is employed. The displacement current, the time derivative of  $E$  is ignored.<sup>50</sup> Writing the total current density as the sum of the electron and ion current densities, the Darwin approximation to Ampere's law becomes

$$\nabla \times \vec{B} = \frac{4\pi}{c} \vec{J} = \frac{4\pi}{c} (\vec{J}_e + \vec{J}_i) \quad (19)$$

Solving for  $J_e$  and substituting the results into equation 18 gives

$$\vec{E} = \frac{\nabla P_e}{en_e} - \frac{\left[ \frac{c}{4\pi} (\nabla \times \vec{B}) - \vec{J}_i \right] \times \vec{B}}{en_e c} \quad (20)$$

---

<sup>49</sup> D.W Hewett, D.J. Larson and S. Brecht. "The Physics of Ion Decoupling in Magnetized Plasma Explosions," report no. LLNL-CONF- 470416 (Livermore, CA, Lawrence Livermore National Laboratory, 2011), 9.

<sup>50</sup> D.W Hewett, D.J. Larson and S. Brecht. "The Physics of Ion Decoupling in Magnetized Plasma Explosions," report no. LLNL-CONF- 470416 (Livermore, CA, Lawrence Livermore National Laboratory, 2011), 9.

We assume that early in time, the gradient of the electron pressure is zero and the magnetic field is irrotational (has no curl) such that

$$\nabla P_e = 0 = \nabla \times \vec{B} \quad (21)$$

The quasi-neutral approximation applies when the Debye length is small compared to the phenomenon under investigation. This approximation means the number of electrons is equal to the number density of the ions multiplied by their charge state<sup>51</sup>

$$en_e \equiv \sum_{species} n_{species} Z_{species} e \quad (22)$$

This approximation allows the denominator of equation 20 to be replaced with a sum of the ion charge density, which consists of debris ions and background ions. Also, early in time assume that the background ions are stationary

$$u_{Br} = 0 \quad (23)$$

Now look at the theta component of the electric field with the ambient magnetic field in the z direction noting that the subscript D refers to the debris and the subscript B refers to the background.

$$E_\theta = \frac{J_{I\theta} B_z}{en_e c} = \frac{(Z_B n_B u_{Br} + Z_D n_D u_{Dr}) B_z}{(Z_B n_B + Z_D n_D) c} \simeq \frac{(Z_D n_D u_{Dr}) B_z}{(Z_B n_B + Z_D n_D) c} \quad (24)$$

The corresponding equation for the radial component of the electric field is

$$E_r = \frac{-J_{I\theta} B_z}{en_e c} = \frac{-(Z_B n_B u_{B\theta} + Z_D n_D u_{D\theta}) B_z}{(Z_B n_B + Z_D n_D) c} \simeq \frac{-(Z_D n_D u_{D\theta}) B_z}{(Z_B n_B + Z_D n_D) c} \quad (25)$$

Collisionless shock is generated if the angular component of the electric field is great enough to accelerate the background ions ahead of the debris ions. The simple force equation for the acceleration of the background ions is

---

<sup>51</sup> Francis Chen, *Introduction to Plasma Physics and Controlled Fusion Vol I* (New York: Springer, 2006), 10.

$$m \frac{d\vec{v}_B}{dt} = q\vec{E} . \quad (26)$$

Looking at the angular component of the vector equation, this becomes

$$m \frac{dv_{B\theta}}{dt} = qE_\theta \approx m \frac{\Delta v_{B\theta}}{\Delta t} . \quad (27)$$

This angular impulse will push the ions into a circular motion. The background ions need to receive enough acceleration within a quarter turn of their normal gyro-rotation in order to stay ahead of the radial accelerating debris ions. This makes

$$\Delta t = \frac{\pi}{2} \frac{1}{\omega_{cB}} = \frac{\pi}{2} \frac{m_B c}{(eZ_B)B_z} . \quad (28)$$

Substituting in equation 24 and equation 28, the ratio of the change in the angular velocity of the background to the radial velocity of the debris becomes

$$\frac{\Delta v_{B-\theta}}{v_{D-r}} = \frac{\pi}{2} \frac{Z_D n_D}{(Z_B n_B + Z_D n_D)} . \quad (29)$$

If this ratio is greater than one, then the electric field can transfer enough energy to the background to rapidly accelerate it ahead of the debris and generate a shock front without particle collisions. The effect is strictly electromagnetic.

In the author's simulations of collisionless shock, the external magnetic field was set in the z direction with a magnitude of 0.3 gauss. The selection of the magnetic field in the z direction establishes the optimal geometry with the debris streaming in the radial direction perpendicular to the ambient magnetic field. This ambient field was affected by the collisionless shock driven by the expanding plasma. If expanding plasma generates a collisionless shock, it produces large variations in the field as seen in Figure 6, which shows the disturbance of the ambient magnetic field at a simulated time of 0.08625 seconds (or 1725 time steps) following a HANE.

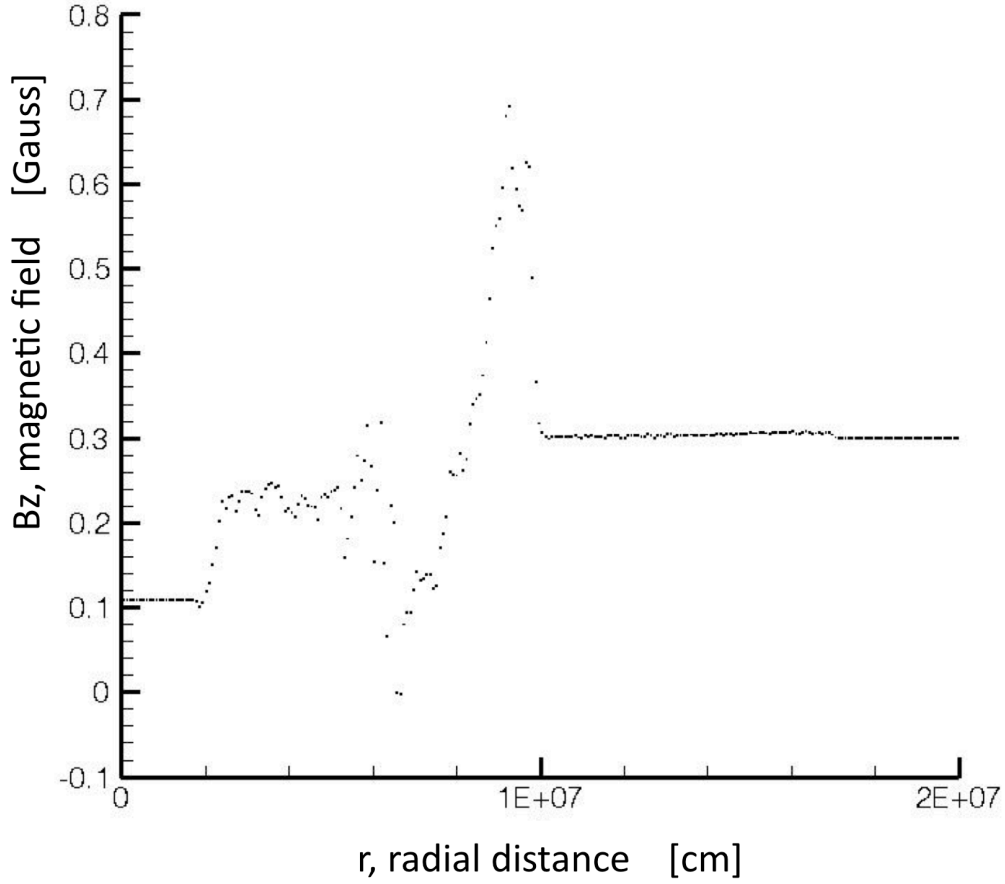


Figure 6. Collisionless shock observed in z component of magnetic field during author's simulation of expanding plasma pushing against background plasma after 1725 time steps while the debris has expanded out to  $10^7$  cm.

In Figure 6, the peak magnetic field value is 0.69 gauss, which is more than double the undisturbed ambient value. Also, the figure shows the sharp rise and fall of this peak. While this is a snapshot of the magnetic field, a charged particle in space would see the time varying magnetic field in the z direction and feel the corresponding electric forces in the radial and azimuthal directions.

## B. COUPLING OF DEBRIS TO BACKGROUND PLASMA

Early work on expanding plasmas typically used MHD models because computational power was lacking for a kinetic ion model. MHD models rely heavily on

concepts from fluid dynamics that assume zero mean-free-path for the ions. In a MHD model, all the expanding plasma is assumed to collide with the background plasma and would be contained by (or coupled to) the background plasma. The snowplow analogy is used where the heavy snowplow pushes against the stationary snow and causes the snow to pile up in front of the snowplow; the same effect is seen in the expanding plasma with the MHD model. The opposite analogy to the snowplow is the ship's bow. A ship moving forward in the water has a narrow bow that pushes the water around the ship's hull. This motion creates a wake (or a wave) that carries away some of the energy but the ship keeps moving forward and the water does not build up in front of the ship. Those two analogies can help understand coupled (snowplow) and uncoupled (ship's bow) plasmas.

In 2011, Hewett *et al.* demonstrated, using a kinetic ion model for simulating expanding ionized debris into a plasma background, that it was possible for the debris plasma to decouple from the background plasma and slip through the background plasma.<sup>52</sup> They established a coupling criterion given by

$$\alpha_{dc} \equiv \left( \frac{\pi}{2} - 1 \right) \frac{Z_D n_D}{Z_B n_B} < 1 \quad (30)$$

where  $\alpha_{dc}$  is the decoupling constant,  $Z$  is the charge state of the debris (subscript  $D$ ) and background (subscript  $B$ ) and  $n$  is the number density of the debris and background. If  $\alpha_{dc}$  is less than one, then the debris will decouple from the background. This slip-through will never be captured by MHD models and is potentially important because it is a mechanism that allows debris ions to expand out to approximately one gyro-radius from the edge of the magnetic bubble.

The coupling is best observed in phase space plots of radial velocity versus radius. Absent any background plasma, the charged particle would spiral around a magnetic field line. In phase space, this motion would be represented by a closed path. In the simulations performed for this research (and building off the work done by Hewett *et al.*),

---

<sup>52</sup>D.W. Hewett, D.J. Larson and S. Brecht. "The Physics of Ion Decoupling in Magnetized Plasma Explosions," report no. LLNL-CONF- 470416 (Livermore, CA, Lawrence Livermore National Laboratory, 2011), 9.

the debris starts at the center of the simulation and pushes out against the background plasma. In the simulations, the debris begins with a radial velocity of  $2 \times 10^8$  cm/s and no velocity in the z or theta components such that

$$v_r = 2 \times 10^8 [cm / s] \quad \text{and} \quad v_\theta = v_z = 0 [cm / s] . \quad (31)$$

At the start of the simulations, the debris is centered along the axis (in cylindrical geometry) at a user specified radius. Beyond the debris, the background plasma begins and fills the remaining spatial domain of the simulation at the user specified number density. In these simulations, the background plasma began with no velocity beyond its thermal motion. At the end of the simulations, the debris has slipped through of the background plasma while transferring little energy to the background plasma. Figure 7 shows a typical simulation result in phase space in which a small increase in the radial velocity of the background plasma (blue and comprised of  $O^{+1}$  ions) from the original value of zero is observed. The radial velocity of the debris is decreasing because the debris ions (represented by as red and comprised of  $U^{+1}$  ions) are turning in the ambient magnetic field and the uranium's velocity is transferred from the radial component to the angular component.

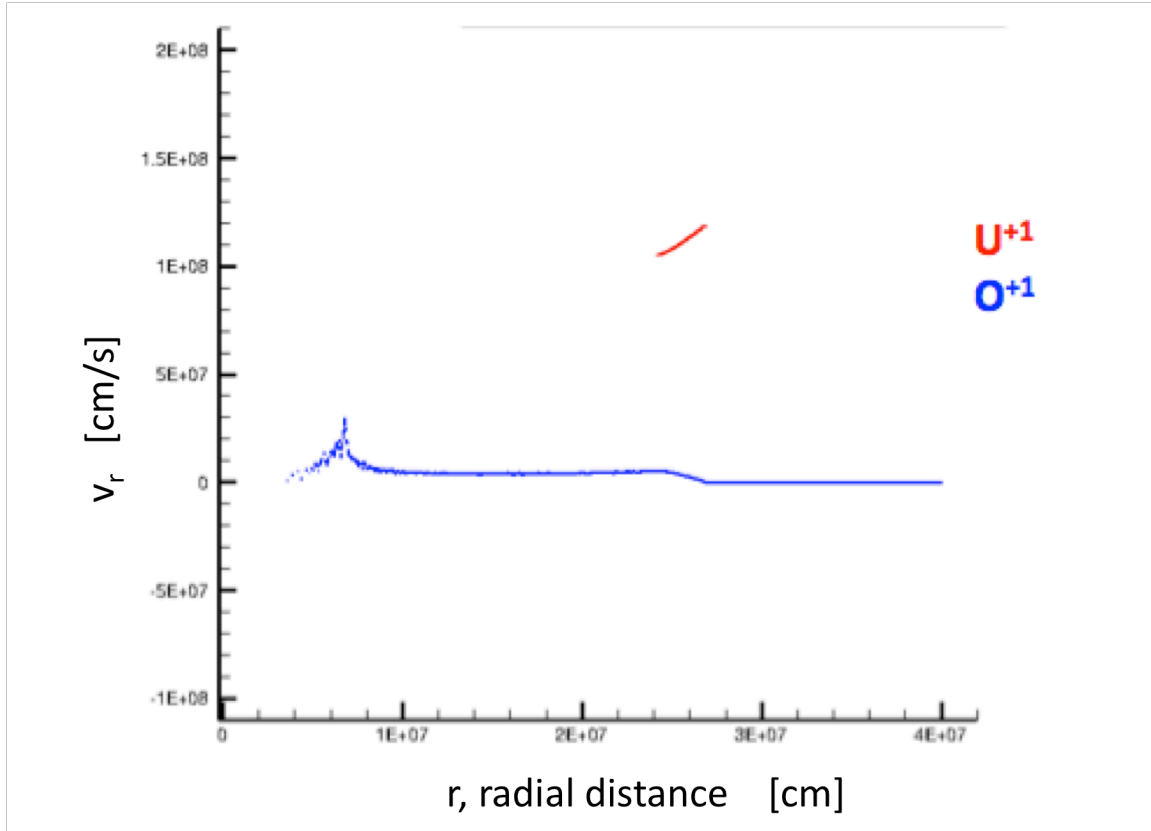


Figure 7. Phase space plot of radial velocity versus radius for author's simulation of uncoupled plasma (red) expanding into a background plasma (blue).

In the case where the debris is coupled (by changing the background density as seen in equation 30) at the end of the simulation, the debris (red) is seen to remain behind the background plasma (blue), as shown in Figure 8 below. Additionally, the radial velocity of the debris plasma is close to zero indicating that the debris plasma has stopped expanding into the background plasma. Comparing Figures 7 and 8, the effects of the coupling can be seen in the background plasma's radial velocity. In Figure 8, the debris plasma (red) has transferred more of its energy to the radial velocity of the background plasma (blue) and the background plasma is now expanding radial outward in the simulation. The simulation involves no collision effects so the transfer of energy from the debris plasma to the background plasma is purely electromagnetic.



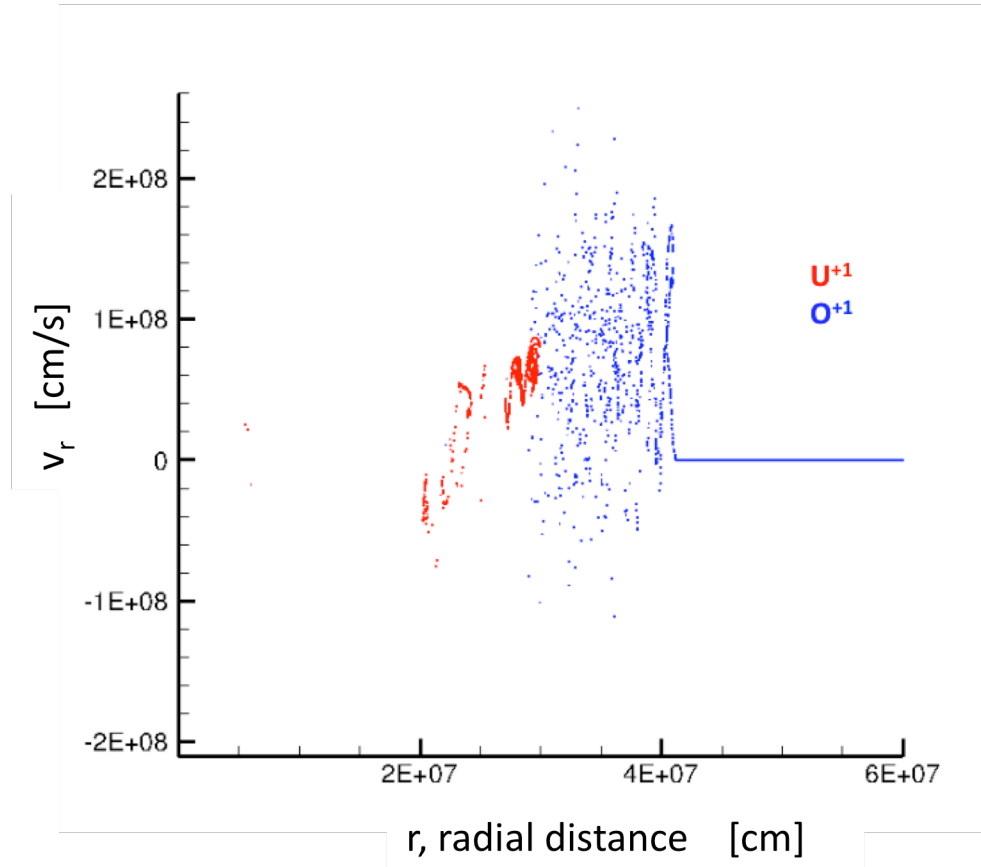


Figure 8. Phase space plot of radial velocity versus radius for author's simulation of a coupled debris plasma (red) expanding into background plasma (blue).

The coupled simulation generates results much like those expected from a MHD simulation.<sup>53</sup> All the energy from the debris is expended in pushing the background plasma and driving the magnetic field. The background plasma's radial velocity is an order of magnitude higher in the coupled simulation than the uncoupled simulation. The work by Hewett *et al.* provides a quick check on whether the correct simulation tool is MHD or PIC. For this work, PIC is the correct tool since kinetic effects are essential to the research. Shocks with multiple species were examined under the hypothesis that one species would drive the collisionless shock and the stronger magnetic field generated would couple species with larger gyroradii.

<sup>53</sup> Hewett, D. Private conversation with author, 23 August 2011.

THIS PAGE INTENTIONALLY LEFT BLANK

## V. CHARGE EXCHANGE

### A. OVERVIEW

The process of charge exchange was the second hypothesis considered in this dissertation research. Charge exchange could contribute to the motion of the weapon debris across magnetic field lines and contribute to the presence of the high-energy electrons at higher L-shells as observed following STARFISH.

#### 1. General Overview

Charge exchange is the process whereby two atoms or ions exchange one or more electrons resulting in both changing their charge state. Because the probability of charge exchange between two ions is several orders of magnitude less than the probability of exchange between an ion and a neutral atom, this work addresses only ion to neutral atom charge exchange. Also, the probability of more than one electron being exchanged is lower than that of a single electron exchange<sup>54</sup> and is therefore not addressed. Additionally, radiative charge exchange is not addressed (in keeping with the Darwin approximation discussed in Chapter IV.A) as the cross section for radiative charge exchange is very small compared to that of other methods of charge exchange.<sup>55</sup>

Collisional charge exchange is usually analyzed by assuming a moving ion and a stationary neutral atom. These are called the projectile and target, respectively, and that nomenclature is used here.

There are two components of charge exchange – electron capture and electron loss. Electron capture takes place when the projectile captures an electron in a collision, decreasing its charge state by one. This has the form

$$P^{+i} + T \rightarrow P^{+i-1} + T^{+1} \quad (32)$$

---

<sup>54</sup> R.E. Johnson, *Introduction to Atomic and Molecular Collisions* (NY: Plenum Press, 1982), 326.

<sup>55</sup> B.H. Bransden and M.R.C. McDowell, *Charge Exchange and the Theory of Ion-Atom Collisions*, (Oxford: Clarendon Press, 1992), 128.

where  $i$  is the initial charge state of the projectile,  $P$  refers to the projectile ion and  $T$  refers to the target atom. Electron loss occurs when the projectile loses an electron in a collision, increasing its charge state. This has the form



where  $i$  is the charge state and  $i \geq 0$ .

Physically, charge exchange is a quantum mechanical process that occurs when the electron wave function overlaps the projectile and the target nuclei. Experimentally, the cross section for charge exchange is measured by shooting a beam of ions into a gas of known pressure. The ion beam is charge analyzed on the opposite side of the gas and a cross section is calculated.<sup>56</sup> The probability of a projectile undergoing charge exchange is

$$p = \sigma(E)|v|n\Delta t \quad (34)$$

where  $p$  is the probability,  $\sigma$  is the cross section,  $|v|$  is the speed of the projectile and  $n$  is the number density of the target. The cross section has the units of area ( $\text{cm}^2$  in these calculations) and is energy dependent.<sup>57</sup> The easiest way to determine the cross section is experimentally.<sup>58</sup> In this work, the cross section is calculated from the semi-empirical formula described below.

The cross section is a method of quantifying the probability of a specific interaction. In this work, the interactions of interest are electron capture and electron loss, and the cross sections for those interactions are employed. The cross section represents a probability of interaction with a large cross section representing a higher likelihood of that specific interaction.

---

<sup>56</sup> H.Knudsen, H.K. Haugen and P. Hvelplund, "Single-electron-capture cross section for medium- and high-velocity, highly charged ions colliding with atoms" *Physical Review A* 23 (February 1981): 597.

<sup>57</sup> R.E. Johnson, *Introduction to Atomic and Molecular Collisions* (NY: Plenum Press, 1982), 21

<sup>58</sup> Ibid. 49

The number density of the target is a function of radial distance. As the distance from the center of the simulation increases, the number density decreases. Eventually, the number density of the target drops below a threshold and the probability of charge exchange drops to a negligible amount. At this radial distance, the charge state is stable and “frozen in.” Charge state freeze-out point depends on the speed and profile of the number density of the target atoms.

## **2. Electron Capture**

Electron capture occurs when the projectile ion captures an electron from the target, thereby decreasing the charge state by one. For an ion at charge state +1, electron capture results in the formation of a neutral atom. A neutral atom will continue on its trajectory with no influence from the electric and magnetic fields. If the initial ion is at a higher charge state than +1, electron capture reduces the charge state by one integer. The smaller charge state increases the Larmor radius and decreases the magnitude of the effect of the magnetic and electric fields.

An ion capturing multiple electrons in a single event is possible but less probable. The probability of an ion capturing multiple electrons is generally an order of magnitude lower than the probability of a single electron capture.<sup>59</sup> Multiple electron captures in a single time step are not simulated in this work.

## **3. Electron Loss**

Electron loss occurs when the projectile loses an electron to the neutral target or the continuum, thereby increasing the charge state by one. The important change is to the projectile charge state. A neutral atom that undergoes electron loss becomes an ion of charge state +1. Now the motion of that charged ion is affected by the electric and magnetic fields.

---

<sup>59</sup> Hans-Dieter Betz, “Charge States and Charge-Changing Cross Sections of Fast Heavy Ions Penetrating Through Gaseous and Solid Media,” *Review of Modern Physics* 44 (1972): 467.

A neutral atom losing multiple electrons in a single event is possible but less probable. The probability of a neutral atom losing multiple electrons is generally an order of magnitude less than the probability of a single electron loss.<sup>60</sup> Multiple electron losses in a single time step are not simulated in this work.

## B. SEMI-EMPIRICAL FORMULATION

The cross section for charge exchange interactions depends on several variables including the energy and the charge state of the projectile. Cross sections can be calculated using complex and time consuming simulations involving quantum mechanics, or they can be measured experimentally. A third and simpler alternative method for computer simulations, especially appropriate for multiple combinations of projectiles and targets with a range of energies and charge states, has also been developed. Schlachter *et al.* originally published a semi-empirical scaling law for electron capture with dependencies on energy (velocity), charge state of the projectile and atomic number of the target.<sup>61</sup> Schlachter's original scaling law has the form

$$\sigma_{ec} = \frac{q^{0.5}}{Z_{tgt}^{1.8}} \frac{1.1 * 10^{-8}}{\tilde{E}^{4.8}} \left[ 1 - \exp(-0.037 * \tilde{E}^{2.2}) \right] * \left[ 1 - \exp\left(-2.44 * 10^{-5} * \tilde{E}^{2.6}\right) \right] \quad (35)$$

where  $q$  is the charge state of the projectile,  $\tilde{E}$  is the scaled kinetic energy that is a function of kinetic energy per nucleon scaled by the atomic number and the charge state, and  $Z_{tgt}$  is the atomic number of the target. Schlachter states that if  $q < 3$ , then the scaling holds using

$$q' = q + 0.4 \quad (36)$$

---

<sup>60</sup> W.N.Spjeldvik and T.A. Fritz, "Theory for Charge States of Energetic Oxygen Ions in the Earth's Radiation Belts," *Journal of Geophysical Research* 83 (1978): 1585.

<sup>61</sup> A.S. Schlachter, J.W. Stearns, W.G. Graham, K.H. Berkner, R.V. Pyle and J.A. Tanis, "Electron capture for fast highly charged ions in gas targets: An empirical scaling rule," *Physical Review A* 27 (1983): 3373.

as an adjustment to the charge state  $q$ .<sup>62</sup> Schlachter *et al.* arrived at this semi-empirical formulation by data-fitting their experimentally measured cross sections to variables they adjusted in their experiments.<sup>63</sup>

Shevelko *et al.* expanded upon Schlachter's original work on electron capture and developed a semi-empirical scaling law for electron loss as well. Their scaling law has the form

$$\sigma_{el} = \frac{q^{0.5}}{Z_{tgt}^{1.8}} (0.88 * 10^{-16}) (Z_{tgt} + 1)^2 \frac{u}{u^2 + 3.5} \left( \frac{1}{I_p} \right)^{1+.01q} \left[ 4 + \frac{1.31}{n_o} \ln(4u + 1) \right] \quad (37)$$

where  $u$  is the scaled velocity in atomic units (such that speed of light corresponds to the velocity value 137),  $q$  is the charge state of the projectile,  $n_o$  is the principle quantum number of the outer electron for the projectile,  $Z_{tgt}$  is the atomic number of the target, and  $I_p$  is the ionization potential for the outer electron for the projectile atom.<sup>64</sup>

Using such a semi-empirical formula for the cross section allows for computer simulations across a range of energies, charge states and elements. The cross sections are easily calculated from the known velocities, masses and charge states. This allows for simulation of a multi-species (elements) plasma with charge exchange. In a PIC code such as ZMR, all the required variables are known and can be included.

### C. MATCH OF SEMI-EMPERICAL FORMULA TO EXPERIMENTAL DATA

Schlachter and Shevelko do not describe the exact method of determining the semi-empirical fit in the development of their semi-empirical formulas. They state that their formulas were matched to available experimental data. The lack of recent and relevant data made comparing this data to the elements of interest difficult. Recent data for the elements of interest at the appropriate velocities and energies was difficult to find.

---

<sup>62</sup> Ibid., 3373.

<sup>63</sup> Ibid., 3372.

<sup>64</sup> V.P. Shevelko *et al.*, "Charge-changing processes in collisions of heavy many-electron ions with neutral atoms," *Nuclear Instruments and Methods in Physics Research B* (2011): 269.

Data from the Air Force Weapons Laboratory (AFWL) in 1968 covered many of the elements of interest at energies just below the values used in this simulation. The AFWL work examined velocities between  $2 \times 10^7$  cm/s and  $1.2 \times 10^8$  cm/s. The simulations in this dissertation research began with an initial velocity of  $2 \times 10^8$  cm/s, so the experimental data set used to benchmark the semi-empirical formulas does not align exactly with the energy spectrum used in the simulation. Some of the data was reasonably close to the semi-empirical formula and some was off by as much as an order of magnitude. Figure 9 is a reasonably close match for electron capture of  $\text{Xe}^{+1}$  in monatomic oxygen, which is one of the elements of interest in this study.

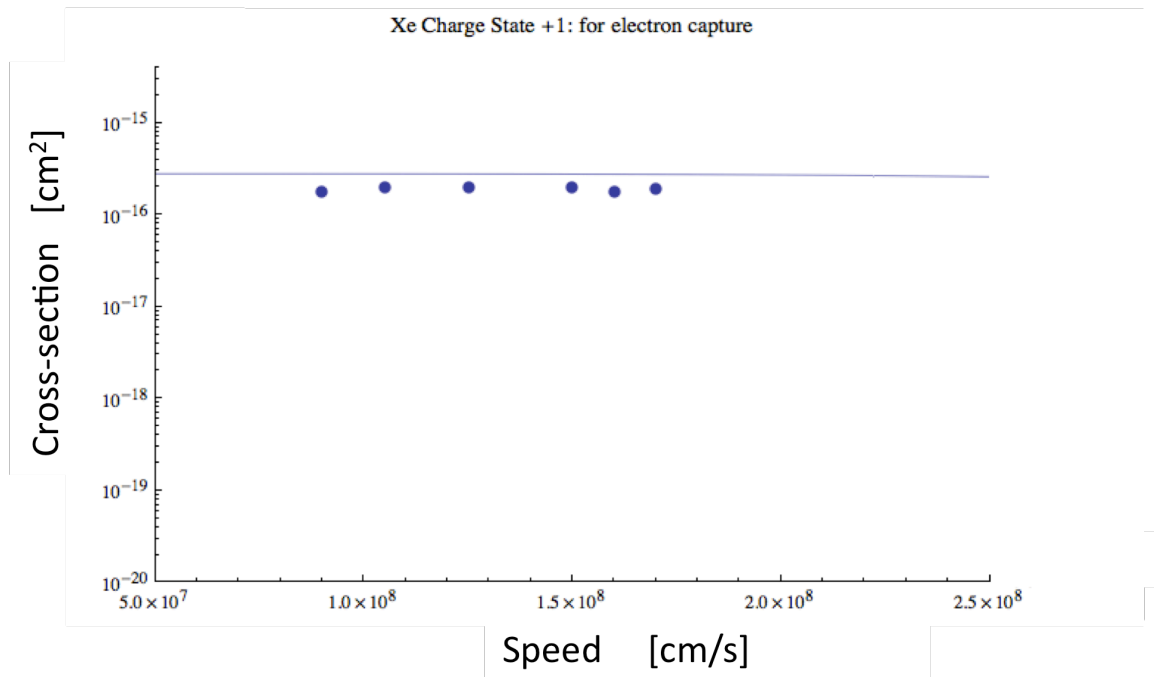


Figure 9. Experimental and semi-empirical cross section of electron capture of Xenon +1 as a function of velocity.



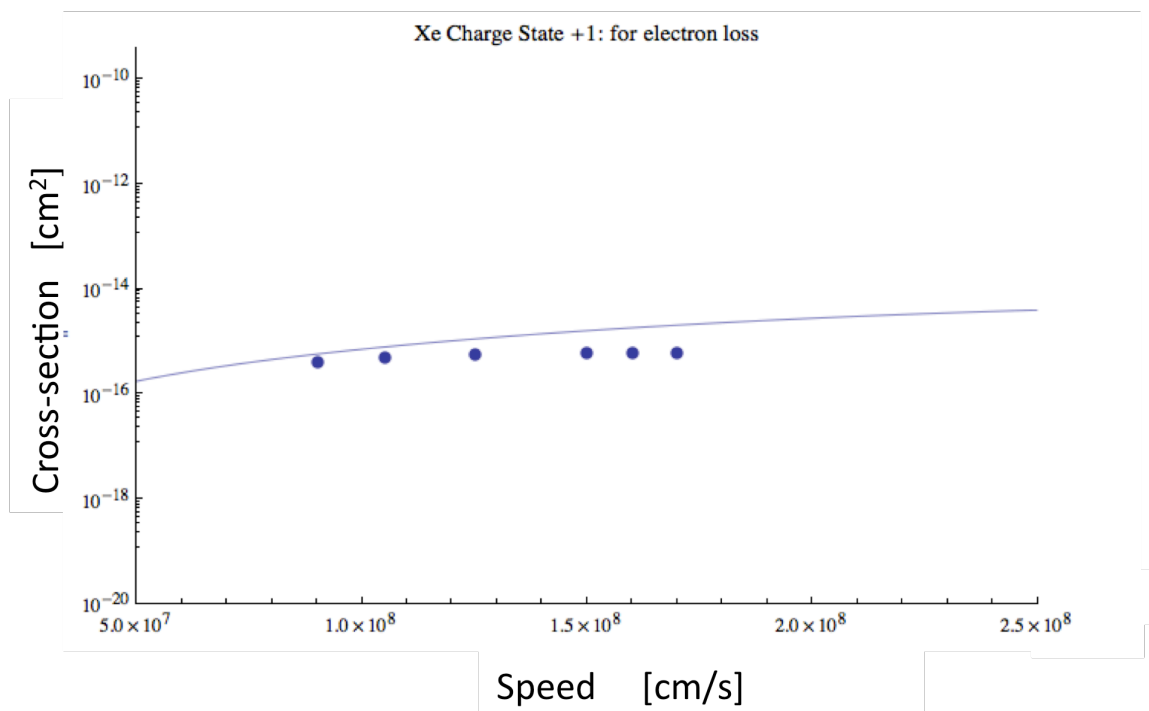


Figure 10. Experimental and semi-empirical cross section of electron loss of Xenon +1 as a function of velocity.

Figures 9 and 10 show a reasonably close correlation of experimental data to the semi-empirical formula for an element of interest in the correct energy/velocity regime of the simulation. However, for uranium the match between the experimental data and the semi-empirical formula was too low by almost an order of magnitude. Figures 11 and 12 show the plot of experimental data (points) against the theoretical cross-section (line).

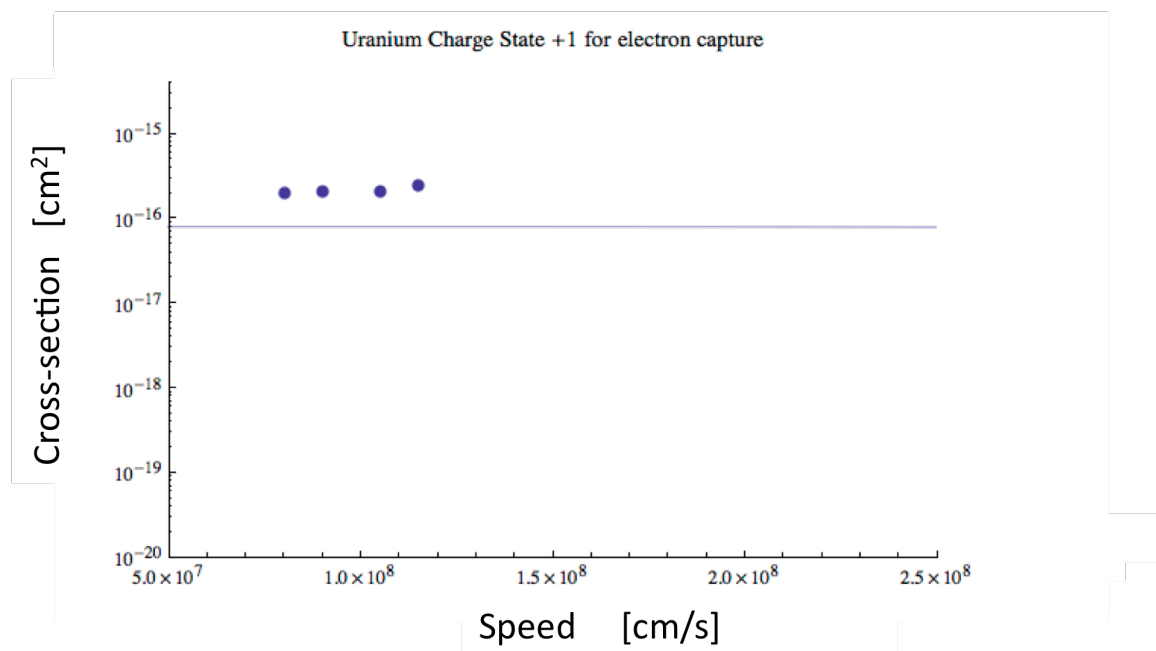


Figure 11. Experimental and semi-empirical cross section of electron capture of Uranium+1 as a function of velocity.

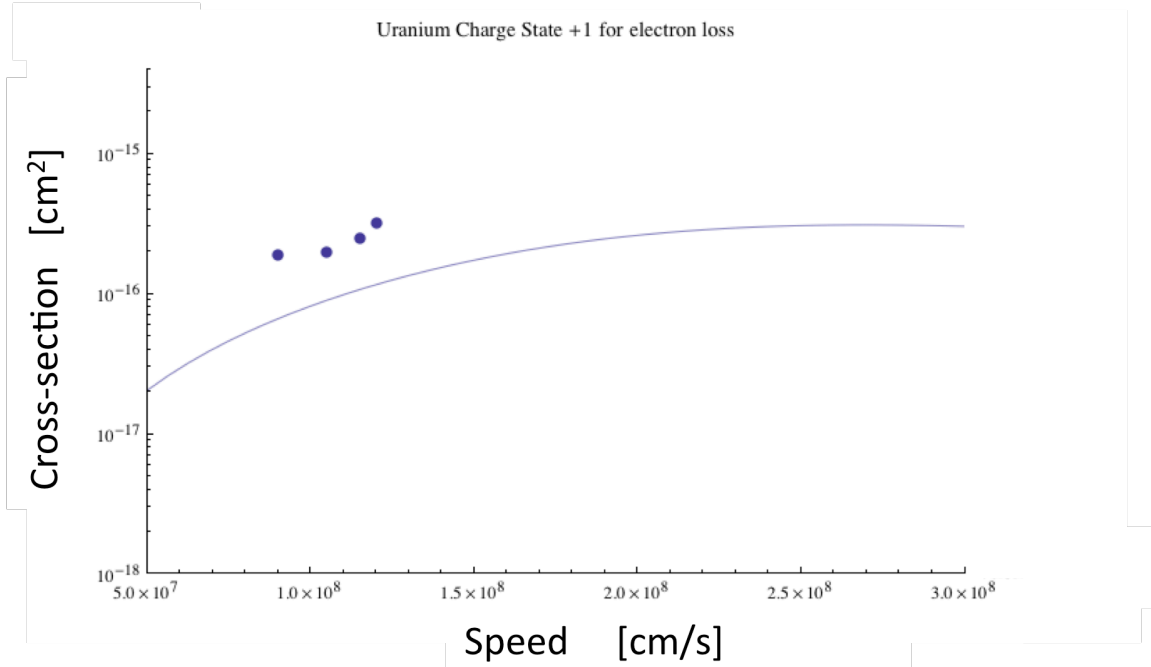


Figure 12. Experimental and semi-empirical cross section of electron loss of Uranium+1 as a function of velocity.

While the velocity regimes do not perfectly align, Schlachter and Shevelko's algorithm is computationally efficient. No other approach to calculating cross sections for both electron loss and electrons capture was uncovered in my literature search. The code was modified in a modular manner and insertion of a different algorithm for calculating cross sections would be straightforward. Finding a more accurate algorithm for calculating cross-sections for electron capture and electron loss in the regimes of interest remains a goal.

THIS PAGE INTENTIONALLY LEFT BLANK

## VI. ZMR CODE DESCRIPTION

### A. OVERVIEW

ZMR is a two dimensional, plasma simulation, FORTRAN code created by Dr. Dennis Hewett of LLNL. It uses the particle-in-cell (PIC) technique in cylindrical geometry to simulate plasma behavior. It has been used for over 30 years on topics that include theta pinch plasma, z pinch plasma, and HANE debris coupling.<sup>65</sup>

ZMR is a hybrid code that treats the ions in the PIC methodology and the electrons as an inertia-less charged fluid. As the ratio of electron to proton mass is 1/1836, less than 0.05% of the mass in the non-relativistic simulation is electrons, so this is a valid assumption. It is assumed that the ions contain all of the inertia, and the electrons are a mass-less fluid that flows along with the heavy ion particles. Hybrid codes provide good resolution for the kinetic effects of the ions, but cannot resolve the kinetic effects of the electrons.<sup>66</sup> A full PIC code that resolves the electron motion requires a very small spatial domain to resolve the electron Debye length and a very small time step to resolve the electron plasma frequency.<sup>67</sup> For plasma at STARFISH altitudes with an energy of 1 electron-volt (eV), this resolution requires a cell length of 0.07 cm and a time step on the order of  $10^{-11}$  seconds. This level of resolution is computationally expensive and six orders of magnitude greater than what is required for a hybrid code. Since this work focuses on the spatial distribution of the debris ions, using a hybrid code provides the appropriate balance of fidelity in spatial domain and speed of computing.

The code also employs the quasi-neutral approximation of plasma physics,<sup>68</sup> which is applicable when the Debye length is much smaller than the length scales under investigation. The Debye length is a measure of the length over which the plasma will

---

<sup>65</sup> D.W. Hewett. "Documentation of the EM 2.5 Quasi-neutral Hybrid Code ZEMER," p3

<sup>66</sup> Petr Hellinger, "Structure and Stationarity of Quasi-perpendicular Shocks: Numerical simulations." *Planet. Space Sci*, 51 (2003): 650.

<sup>67</sup> Ibid. 651.

<sup>68</sup> D.W. Hewett. "Documentation of the EM 2.5 Quasi-neutral Hybrid Code ZEMER," p2

shield the field introduced by a test charge. If this condition holds, the plasma is considered “neutral enough” and mathematically the electron density is approximately equal to the ion density.<sup>69</sup> This is written as

$$n_e \simeq n_i \quad (38)$$

This approximation becomes important when calculating electrical currents as well as solving the field equations.

The geometry assumes symmetry in the theta (angular) direction such that the partial derivative of any variable with respect to  $\theta$  is zero.

$$\frac{\partial}{\partial \theta} = 0 \quad (39)$$

and the particle displacement in the theta direction is set to zero in every time step.<sup>70</sup> Thus, the direction of interest in ZMR is radial. However, the theta components of all the vectors are calculated and maintained throughout the simulation. For this reason, ZMR is referred to a 2.5 dimension code.

Different problems are modeled in ZMR by different inputs at the start of the simulation. The input module allows the user to set the spatial parameters of the simulation as well as the size of the time step. Within the input module, the user can specify the number of species modeled in the simulation, as well as the starting geometries, densities and velocities of each species. The beginning geometry, density and atomic mass of a species determine the initial mass of that individual species.

Since the total mass of a species is specified and the total number of simulation particles for that species is also specified, ZMR computes the number of real particles per simulation particle (RPPSP). This quantity is initialized for the species but is tracked for each individual simulation particle. As a simulation particle quantity, it enables the

---

<sup>69</sup> Francis Chen, *Introduction to Plasma Physics and Controlled Fusion Vol I* (New York: Springer, 2006), 10.

<sup>70</sup> D.W. Hewett, Documentation of the EM 2.5 Quasi-neutral Hybrid Code ZEMER, 3.

addition of the charge exchange routine by allowing a simulation particle to “split” into two simulation particles. The simulation particle that splits from the original simulation particle will have the same location and velocity but different charge states reflecting that some of the real particles modeled by the simulation particle have undergone charge exchange. The total mass of the simulation is unchanged as the original simulation particle has its RPPSP value decreased by the same amount as the new particle created with a different charge state. This procedure conserves mass, energy and momentum within the simulation but it does result in an exponential increase in the number of simulation particles. As the number of simulation particles increases, the simulation undergoes more individual calculations and slows down. Including charge exchanged increased the simulation run time (wall time) by a factor of ten.

Advancing the position is done using the Boris Push method. The Boris Push method is an algorithm to time advance the Lorentz force equation. Generally, the Boris Push method uses a half time step advancement from the electric field,

$$\vec{v}_{prime} = \vec{v}_{old} + \frac{q}{m} \vec{E} \frac{\Delta t}{2}, \quad (40)$$

a full time step advancement from the magnetic field ,

$$\vec{v}_{temp} = \vec{v}_{prime} + \vec{v}_{prime} \times \vec{B} \frac{q}{mc} \Delta t, \quad (41)$$

followed by a rotation of that magnetic field advancement

$$\vec{v}_{plus} = \vec{v}_{prime} + \frac{2}{1 + \vec{B}^2} \left( \vec{v}_{prime} \times \vec{B} \frac{q}{mc} \Delta t \right), \quad (42)$$

and then the last half time step advancement from the electric field

$$\vec{v}_{new} = \vec{v}_{plus} + \vec{E} \frac{q}{m} \frac{\Delta t}{2}. \quad (43)$$

A more detailed explanation of the Boris Push method is available in Birdsall and Langdon.<sup>71</sup> The new positions

$$\vec{x}_{new} = \vec{x}_{old} + \vec{v}_{new}\Delta t \quad (44)$$

of all the particles are used to calculate the charge densities and, along with the new velocities, are used to calculate the electric currents.

After the particles are advanced in time, the electric and magnetic fields are advanced in time. The cylindrical geometry allows the theta component of the vector potential to be solved for explicitly from the electron momentum equation (in the limit of small electron inertia). From the explicitly calculated value of the theta component of the vector potential, the radial and z components of the magnetic field are calculated. The theta component of the magnetic field is calculated in a manner similar to the theta component of the vector potential. The components of the electric field are calculated from the electron momentum in equation 18.

ZMR employs the Darwin approximation that removes the propagation of electromagnetic waves.<sup>72</sup> This approximation means changes to the electric and magnetic fields propagate instantly across the simulation with no time delay. This is a valid assumption because the study is focused on the motion of ions and not the electromagnetic waves produced by the plasma. The electric and magnetic fields are computed and stored on the simulation grid. Only the closest four grid points contribute to the fields used in the equations of motion for the particle at a particular point. In Figure 13 below, the electric and magnetic fields at the simulation particle represented by the green dot are calculated from the values of those fields stored on the grid represented by the blue dots. The other values of the fields on the grid (represented by the red dots) do not impact the motion of simulation particle. In the computational time step, an

---

<sup>71</sup> C.K. Birdsall and A.B. Langdon, *Plasma Physics Via Computer Simulation*. (New York: Taylor and Francis Group, 2005), 59.

<sup>72</sup> M.R. Gibbons and D.W. Hewett, "The Darwin Direct Implicit Particle-in-Cell Method for Simulation of Low Frequency Plasma Phenomena," *Journal of Computational Physics* 120 (1995): 232.



electromagnetic wave would prorogate across four cells so assuming the wave is faster does not change the physics.

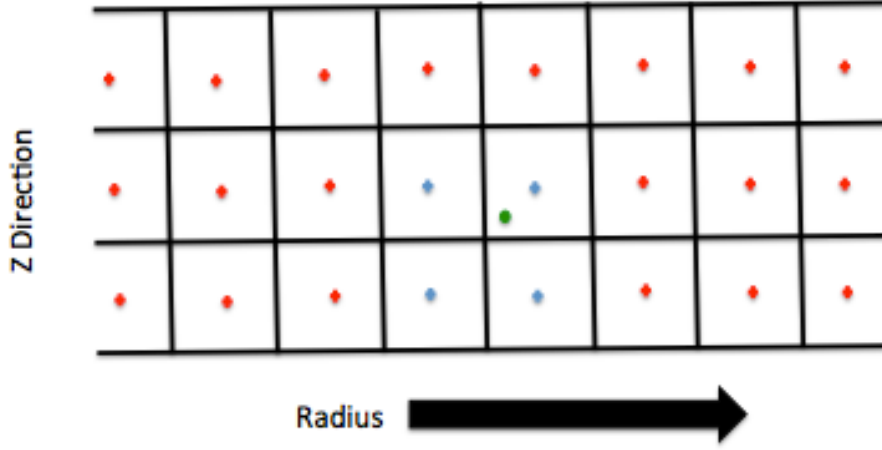


Figure 13. View of simulation grid with one simulation particle (green) and diamonds showing cell centered field values. Only the blue diamonds contribute to the force computations for the green simulation particle.

The data from ZMR is captured in output data files. For every species, the position and velocities are recorded. The magnetic field is also captured to observe the magnetic shock front.

## B. COMPUTATIONAL FLOW IN ZMR

ZMR follows the general flow of hybrid PIC codes of advancing the particles using the Lorentz force, accumulating the source terms on the grid, calculating the electric and magnetic fields and then advancing the time step. The following is a brief overview of all those steps.

At the beginning of a time step, the particles are moved according to the Lorentz force

$$\frac{d\vec{v}}{dt} = \frac{\vec{v}_{new} - \vec{v}_{old}}{\Delta t} = q(\vec{E} + \vec{v} \times \vec{B}) \quad (45)$$

This vector equation can be decomposed into its scalar, directional components such as

$$\frac{dv_x}{dt} = \frac{v_x^{new} - v_x^{old}}{\Delta t} = q(E_x + v_y B_z - v_z B_y) \quad (46)$$

for the x component and similar expansions for the y and z components. This difference equation is solved for the time-advanced velocity in all three components. Then the positions of all the particles are advanced. From this time advanced positions, the currents and charge densities are calculated and assigned to the internal grid structure.

After the time-advanced positions, currents and charge densities are calculated, the time-advanced values for the electric and magnetic fields are calculated. ZMR capitalizes on the ability to solve for the theta component of the vector potential ( $A_\theta$ ) explicitly. The angular symmetry required in ZMR and the use of cylindrical geometry allows for the closed form solution to  $A_\theta$ . Once the theta component of the vector potential (A) is found, the radial and axial components of A are calculated. From the components of A, the components of the magnetic field (B) are easily calculated using

$$\nabla \times \vec{A} = \vec{B} \quad (47)$$

since all the components of the vector potential are known. A complete explanation of the field-solving algorithm is available from Hewett.<sup>73</sup> The computer program iterates position advancement and then a field calculation every time step. The number of time steps is a user specified input.

The species of interest in this work were derived from selected debris and fission fragments from the nuclear weapon and the ambient ionosphere. As shown in Figure 4, atomic oxygen is the dominant constituent of the unperturbed atmosphere at the time and elevation of STARFISH, so singly ionized oxygen was used as the background plasma and neutral oxygen was used as the catalyst for charge exchange. For fission fragments, the elements of xenon and zirconium were used to correspond to the high points of the fission fragment distribution curve. Lead and carbon were also examined as elements at the extreme heavy and light ends of the mass spectrum.

---

<sup>73</sup> D.W. Hewett, "A Global Method of Solving the Electron-Field Equations in a Zero-Inertia-Electron-Hybrid Plasma Simulation Code," *Journal of Computational Physics* 38 (1980): 379–395.

### **C. INITIAL CONDITIONS USED IN THE SIMULATIONS**

In this work, a common set of user-supplied physical parameters was used in order to allow a consistent comparison of results. The grid was divided into 256 cells in the radial direction and one in the axial direction (plus two ghost cells in the axial direction to calculate the fields primary cell). The spatial domain in the radial direction was set to 600 km. The spatial domain in the axial direction was set to 10 km. The time step was set to  $5 \times 10^{-5}$  seconds. These parameters were used throughout all the simulations examining both collisionless shock generated from multiple species and charge exchange.

### **D. SPECIFIC MODIFICATIONS FOR THIS WORK**

The ZMR Code was the starting point for this work. The simple geometry and speed of execution made it a natural starting point to examine the physics of collisionless shock and charge exchange. Since charge exchange appears to have a significant impact on the motion and final spatial distribution of the debris, it is being incorporated into other codes at LLNL or other research facilities that have higher fidelity and more representative geometry.

In this work, the intent was to use ZMR to simulate a 1-D radial slice of the expanding plasma. In order to reduce the spatial dimensionality, the simulations were initialized with only one cell in the z direction. That one cell width was set to 10 km, large enough to prevent simulation particles from leaving the simulation through the ends of the cylindrical mesh. These dimensions are large enough to replicate the distance of relevance for STARFISH and simulate the motion of the debris.

#### **1. Modifications for Including Multiple Species**

ZMR was run using a debris plasma consisting of multiple species. This ability was already resident within ZMR but Hewett's previous work focused on single species

debris for his studies of coupling.<sup>74</sup> Using multiple debris species required only slight modifications to the input file.

In the initial simulations, the two species were different charge states of uranium. One species maintained a charge state of +1 while the second species had a charge state of +2, +4 or +8, depending on the simulation. The ratio of charge state to mass determines the Larmor radius (as defined in equation 14). Holding the mass constant while varying the charge state allowed for different plasma interactions while simplifying the number of variables. Keeping a constant mass and number density in the simulation also kept the kinetic energy constant. It was possible to understand the effects of the multiple species on the formation of collisionless shock by varying the charge state of a single element/isotope.

The debris plasmas were initialized in two different configurations. In the first configuration, all the debris plasma was co-located in a single mix with a radius of 10 km. In the simulation the debris plasmas expanded into the background plasma and the ambient magnetic field and the different Larmor radii separated the two charge states. In the second configuration, the debris plasma was initially stacked into two shells with the higher charge state on the outside with an outer radius of 10 km. The lower charge state was on the inside of the expanding cylinder with an initial radius of 5km. This geometry relates to the heavier element on the inside and the lighter element on the outside if all the charge states were set to +1. Again the debris species expanded into the background plasma and the ambient magnetic field.

All of the multispecies simulations without charge exchange were conducted using a constant atmosphere. The constant density was used to focus on the effects from multiple species on the collisionless shock formation and not on the atmospheric density.

## **2. Modifications to Analyze Charge Exchange**

ZMR had to be modified to include the physics of charge exchange. The thrust of the research was to determine if charge exchange would affect the final spatial

---

<sup>74</sup> D.W. Hewett, private conversation with author, 28 July 2011.

distribution of the debris. Could neutral debris produced by charge exchange make it through the shock front? If so, how much and at what velocity? The desire to investigate these effects guided how the physics of charge exchange was implemented in the code modifications.

The two competing processes of charge exchange (electron capture and electron loss) could be dealt with separately or combined into a single process. Combining them into a single process would involve comparing the rates of electron capture and electron loss and calculating the difference between the two rates. This difference would be manifested as a change in the charge state. This method does not reflect the two-step charge exchange process. First, a charged ion undergoes electron capture and becomes neutral. Then that neutral atom travels a distance before undergoing electron loss and becoming charged again. The distance traveled as a neutral atom is a kinetic effect that will determine the final spatial distribution of the debris and thus could not be discounted.

Another option for modeling charge exchange would involve adjusting the charge state of the simulation particle to account for the relative change in charge state. The charge state of the species is an input parameter and is typically an integer. However, in ZMR the variable for charge state is defined as a real number, and thus could have a fractional value. Based on the difference in the rate of charge exchange, the variables for charge state could be adjusted to account for the difference in electron capture and electron loss cross sections computed. Adjusting the charge state would change the Larmor radius for that species. This adjustment would also affect the final spatial distribution; however it would not appropriately simulate physical behavior. Ions do not have charge states with fractional values and this technique would produce charge states with non-integer values. Therefore, this computational approach would have produced non-physical results and was not pursued.

The modification used in this work involved transporting the simulation particles through neutral oxygen. Each simulation particle represents many real particles and is tracked by a variable assigning the number of real particles per simulation particle (RPPSP). A certain number of these real particles will undergo charge exchange. That number was calculated directly using

$$number = \sigma(E)|v|n_oR(\Delta t) \quad (48)$$

where  $\sigma(E)$  is the calculated cross section for either electron capture or electron loss,  $|v|$  is the speed,  $\Delta t$  is the time step,  $n_o$  is the number density of neutral oxygen, and  $R$  is the number of real particles per simulation particle. The existing simulation particle is decremented in how many simulation particles it represents ( $R$ ) and a new simulation particle of different charge state is created with the same spatial properties as the original simulation particle. The total number of real particles in the simulation is unchanged. The newly created simulation particle has an integer value for charge state and a clearly defined Larmor radius; this would not be the case if the charge states were just adjusted to a fraction. This new simulation particle will move at least a time step before undergoing charge exchange and this movement will affect the spatial distribution of the debris. This method of tracking charge exchange creates the problem of geometric growth in the number of simulation particles. Use of the high performance computing resource at LLNL allowed for relatively quick runs using two debris species.

The charge exchange routines were inserted into the original code in the particle movement phase of the logic flow. After all the particles have their new locations determined, the charge exchange routines are applied to the debris ions. To control the geometric increase in the number of simulation particles, all debris particles start at charge state +1. No higher initial charge states were considered in this work examining the effects of charge exchange. Those ions at charge state +1 underwent electron capture and those neutral debris atoms underwent electron loss. Once all the charge states were adjusted, then ZMR collected the source terms of charge density and current to be used in the subsequent field calculations. The fields are calculated using the source terms appropriately adjusted for charge exchange, and reflect the correct values for each time step. The value of the time step ( $\Delta t$ ) needed to be kept small enough so that not all the particles underwent charge exchange in a single time step. Having all the atoms undergo charge exchange in a single time step is not physically realistic and would introduce instabilities in the calculations.

Another modification involves the use of an exponentially declining atmospheric density. The particle density for the atmosphere is dependent on the height above the surface of the Earth. This decrease with altitude is exponential and occurs for both the neutral and ionized oxygen atoms. After modification, ZMR could be run with either a constant particle density or an exponentially decreasing atmosphere. The number density of the neutral oxygen species is used only to compute the amount of charge exchange; the neutral oxygen species has no other impact on the plasma dynamics. Therefore, neutral oxygen atoms are not represented with simulation particles but its density is stored on the grid of the simulation and called at the appropriate value for the location of the simulation particle undergoing charge exchange. The number density of the neutral oxygen atoms could be made an exponentially decreasing function of radial distance to simulate the exponential decrease in real density.

It was assumed that all the initially neutral oxygen within 50 km of the detonation was highly ionized by the detonation and no neutral oxygen existed within this range following the detonation. In both the constant density and exponential atmosphere, the charge exchange routines were not called while the simulation particle's displacement from the centerline axis was less than 50 km.

Unlike neutral oxygen atoms, ionized oxygen in the background directly affects the kinetics of the debris plasma. Therefore, the ionized oxygen is represented by simulation particles and ZMR computes all the kinetics for ionized oxygen as the background plasma. The exponentially decreasing number density for ionized oxygen was simulated by exponentially decreasing the real particles per simulation particle (RPPSP) variable assigned to the ionized oxygen simulation particles. Figure 14 shows the number density of the real background plasma particles used in ZMR for the exponentially decreasing atmosphere. This allowed the simulation of the interaction between the debris plasma and the background plasma to capture the kinetic effects while including an exponentially decreasing atmosphere.

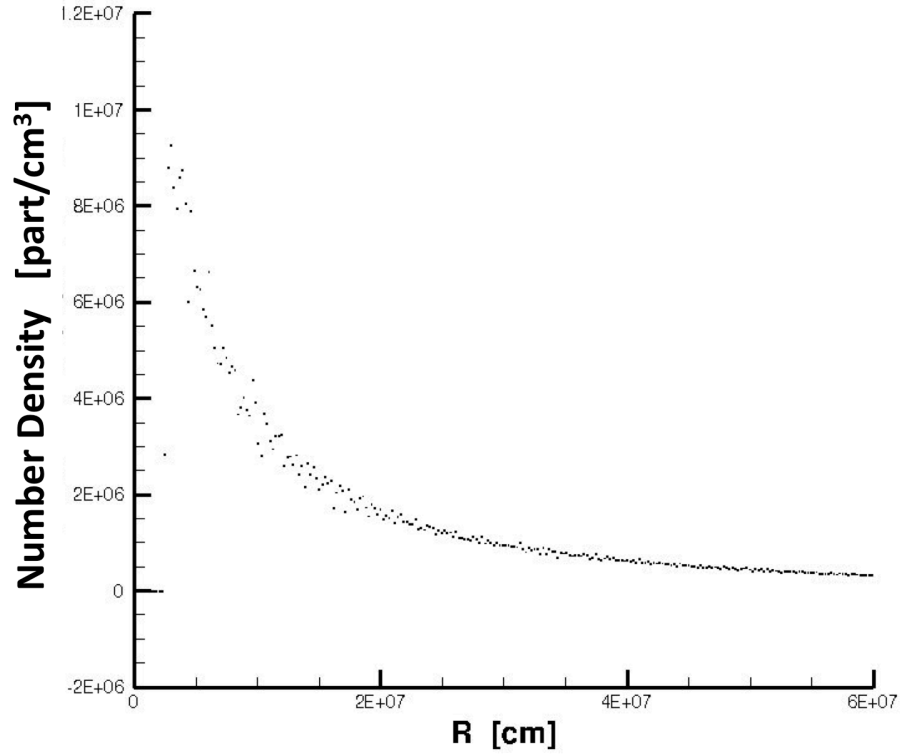


Figure 14. Oxygen+1 background plasma number density as a function of radius.

## E. VERIFICATION OF ZMR

ZMR has been used for the simulations of plasma dynamics for over 30 years at LLNL. While it uses a different algorithm to solve for the electric and magnetic fields, its results are comparable to those from other hybrid plasma codes. During the modification of ZMR in this dissertation research, care was taken to verify that results from reference calculations were the same before and after each modification. Additionally, cross section calculations from ZMR match cross section calculations performed by hand. This provided a high level of confidence that the code modifications were implemented correctly.



As a separate test, ZMR was also modified to remove the plasma background and replace it with only a neutral hydrogen background. The debris plasma was injected as a beam directed into the neutral hydrogen. According to the Trapped Radiation Handbook, the fraction of atoms that should be neutral is given by

$$Y = \frac{\sigma_{10}}{\sigma_{10} + \sigma_{01}} \left\{ 1 - \exp \left[ -\frac{\rho(\sigma_{01} + \sigma_{10})s}{m} \right] \right\} \quad (49)$$

where  $Y$  is the neutral fraction,  $\sigma_{01}$  is the ionization cross section,  $\sigma_{10}$  is the neutralization cross section,  $\rho$  is the mass density,  $s$  is the penetration depth and  $m$  is the atomic mass.<sup>75</sup> The steady state case allows for very deep penetration of the projectile ion into the neutral background and  $s$  is very large. The steady state value of the neutral fraction reduces to just the leading term of equation 49. To run this test case computationally, the external magnetic field was turned off ( $B_z=0$ ) so the uranium ions would not turn. The background plasma was set to neutral atomic hydrogen so there was no coupling and no energy transfer between the uranium ions and the background. The exponential neutral atmosphere profile was replaced with a constant density profile. At a velocity of  $2 \times 10^8$  cm/s, the cross section for electron capture is calculated as  $2.7 \times 10^{-16}$  cm<sup>2</sup> and the cross section for electron loss is calculated as  $2.75 \times 10^{-16}$  cm<sup>2</sup>. The asymptotic limit for equation 49 is 0.48. Figure 15 show Equation 49 plotted as a mathematical function. Figure 16 shows the fraction of neutral particles from the simulation approaching the theoretical limit of 0.48. The simulation data in Figure 16 also has the calculated characteristic time ( $e^{-1}$ ) of 0.003 seconds. The similarity between Figures 15 and 16 show the similarities between the physics principle and the computational simulation of that principle. This similarity furthers the confidence that modification to ZMR to include charge exchange was implemented correctly.

---

<sup>75</sup> *Trapped Radiation Handbook*, 7-7.

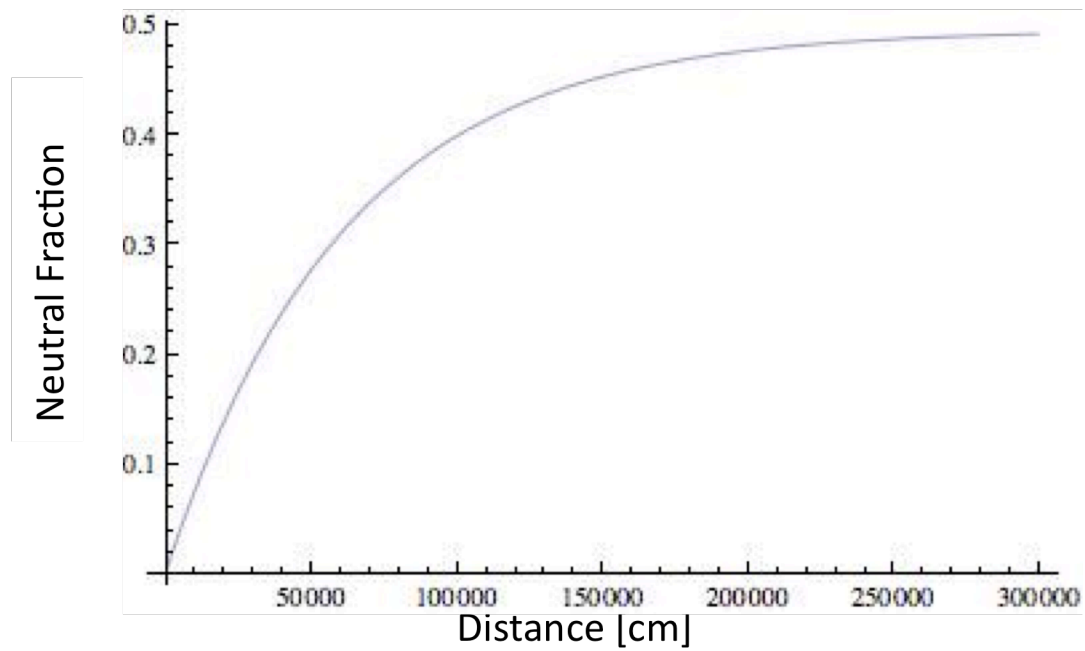


Figure 15. Neutral fraction of uranium in theoretical calculation as a function of penetration distance.

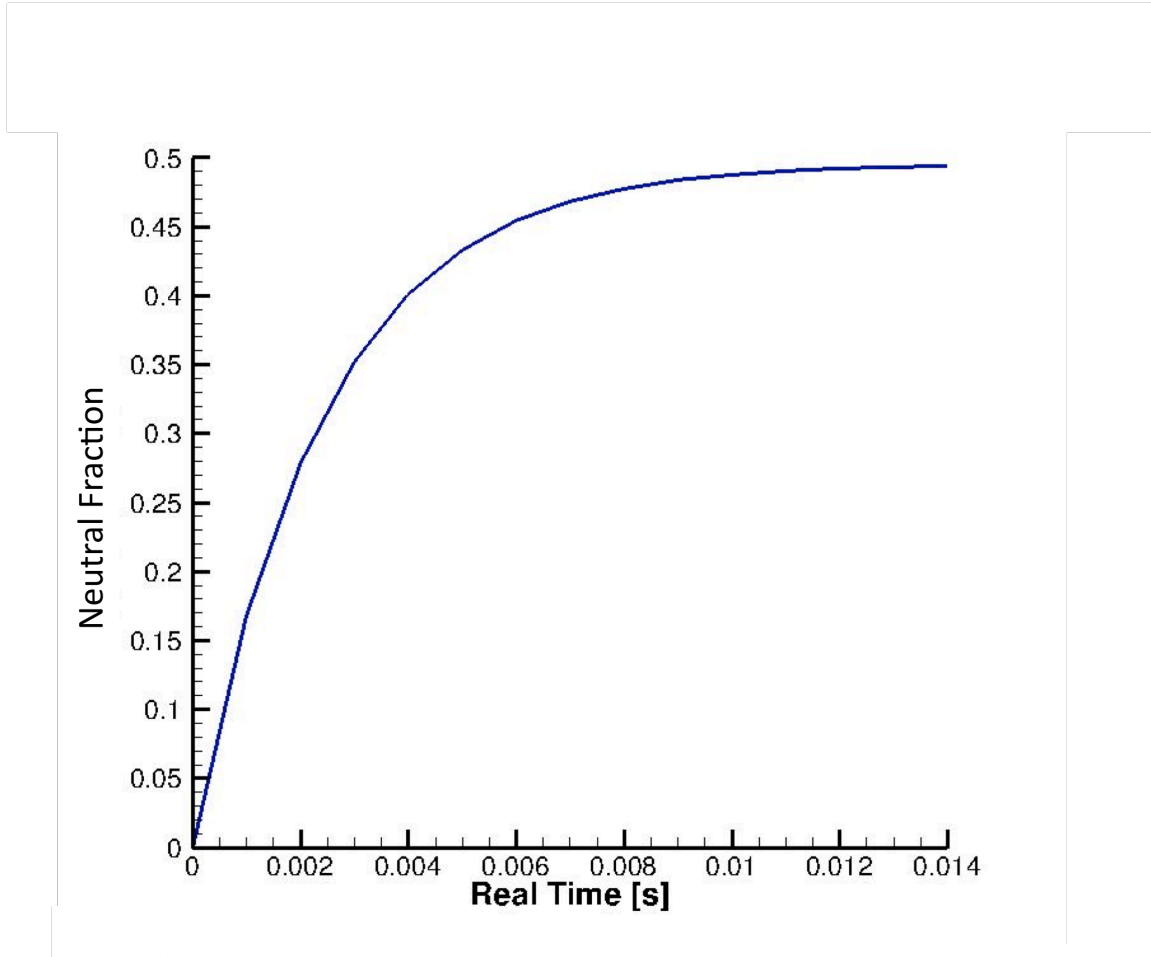


Figure 16. Neutral fraction of uranium in test simulation as a function of real time.

This match between the theoretical calculations and the simulation results for a simple case gives higher confidence that the simulation is correctly applying the same physics in a more complicated case with velocity dependent cross sections.

## F. OVERVIEW OF SIMULATIONS EMPLOYED

This work employed simulation of plasma to reveal the underlying physics of the debris streaming outward from a HANE. Because the principles under investigation are kinetic in nature and involved the movement of ions under the influence of magnetic fields, including those that are self-induced, a particle-in-cell (PIC) code was employed.

This work relied primarily on a previous code developed at LLNL – ZMR,<sup>76</sup> with modifications to introduce additional physics. The resulting modifications of ZMR provided the vehicle to examine two different processes – (1) collisionless shock driven by multiple species; and (2) charge exchange, as well as the effects of those processes on the final spatial disposition of the debris from a HANE. These two processes were considered as possible explanations for the anomalous debris distributions observed in tests such as STARFISH.

The first process investigated was collisionless shock driven by multiple species of debris ions. To keep the comparisons similar across various simulations, the simulations considered multiple ionic states of the single isotope uranium-238. The effects of multiple species were introduced by varying the charge state of the uranium atoms. One debris species of uranium was kept at charge state +1 while the second debris species of uranium had a variable charge state, taking values of +2, +4 and then +8. The variable charges served as a surrogate for consideration of other lighter elements. The advantage of varying charge state in lieu of mass was consistency in comparison between simulations. Since the mass and number density were the same between simulations, the various simulations could be conducted with the same total energy content. The different gyroradii (from the different charge states) was the variable under consideration.

This evaluation of collisionless shock simulated two different configurations of the debris. In the first configuration, the debris species were considered to be mixed evenly at the starting radius (i.e., the point of detonation). This first configuration was simulated to serve as a proof of principle and to confirm the proper functioning of the model. The ZMR program was programmed to handle two debris species (with a set number density) in which the user specifies the initial region of the debris. In the second configuration, the debris was staggered in initial distribution: the outer debris had the lower charge state (charge state +1), representing the heavier ions. The inner debris had a higher charge state (charge state +2, +4 or +8), representing the lighter ions. These second configuration simulations, with the staggered debris, tested the hypothesis that the

---

<sup>76</sup> D.W. Hewett, Documentation of the EM 2.5 Quasi-neutral Hybrid Code ZEMER, 1.

large gyroradii ions could drive collisionless shock disproportionately affecting the smaller gyroradii (i.e., lighter or more highly charged) ions as they passed through the shock. Table 1 summarizes the simulations carried out to evaluate the hypothesis of collisionless shock.

<b>Simulation</b>	<b>Debris Species 1</b>	<b>Debris Species 2</b>	<b>Debris Configuration</b>	<b>Hypothesis tested</b>
CS-1	U+1	U+1	Co-located – evenly mixed	Proof of coding
CS-2	U+1	U+2	Co-located – evenly mixed	Effects of lighter species – half mass
CS-3	U+1	U+4	Co-located – evenly mixed	Effects of lighter species – quarter mass
CS-4	U+1	U+8	Co-located – evenly mixed	Effects of lighter species – eighth mass
CS-5	U+1	U+2	Staggered	Effects of lighter species – half mass
CS-6	U+1	U+4	Staggered	Effects of lighter species – quarter mass
CS-7	U+1	U+8	Staggered	Effects of lighter species – eighth mass

Table 1. List of simulations conducted to examine collision shock driven by multiple species.

Following the simulations with multiple species focusing on the collisionless shock mechanism, the investigation turned to examine the hypothesis that charge exchange among the debris ions could contribute to the observed anomalous distribution of debris. This investigation considered both electron capture and electron loss by the debris ions interacting with the neutral oxygen in the background. The hypothesis pursued was that debris ions that would normally be coupled with the background plasma (and therefore not able to penetrate very far during the course of the simulation) would

travel further (radially from the explosion) with charge exchange as a portion of the ions would be neutralized and therefore not coupled behind the background plasma. Formed as fission fragments, these particles could later beta decay and release high-energy electrons further from the center of the nuclear explosion. Columns 2 and 3 in Table 2 list the combination of debris species examined in the charge exchange portion of this dissertation. Debris Species 2 (listed in the third column of Table 2) shows the common fission fragments used by LLNL in their separate simulations.

Another characteristic of the configuration used in the simulation to evaluate charge exchange was the use of different atmospheric profiles. The background plasma (of flash-ionized monatomic oxygen) had two different configurations. The first configuration assumed a constant number density for the background plasma throughout the radial dimension of the simulation cells. The second configuration employed an exponentially-decreasing number density for the background plasma of flash ionized oxygen. These differences are shown in the fourth column in Table 2.

In both atmospheric configurations, there were two simulations per debris species pairing – one without charge exchange and one with charge exchange. Without charge exchange, both species of the debris plasma coupled with the background plasma. With charge exchange, some of each species in the debris plasma moved through the shock front in the background plasma. It is these debris atoms, which could later beta decay at higher elevations and introduce high-energy electrons, that appear to account for some of the observed anomalous debris distributions. Table 2 summarizes the simulations carried out to evaluate the hypothesis of Charge Exchange.

<b>Simulation</b>	<b>Debris Species 1</b>	<b>Debris Species 2</b>	<b>Atmosphere</b>	<b>Charge Exchange</b>
CE-1	U+1	U+1	Constant	No
CE-2	U+1	U+1	Constant	Yes
CE-3	U+1	Xe+1	Constant	No
CE-4	U+1	Xe+1	Constant	Yes
CE-5	U+1	Zr+1	Constant	No
CE-6	U+1	Zr+1	Constant	Yes
CE-7	U+1	Pb+1	Constant	No
CE-8	U+1	Pb+1	Constant	Yes
CE-9	U+1	Xe+1	Exponential	No
CE-10	U+1	Xe+1	Exponential	Yes
CE-11	U+1	Zr+1	Exponential	No
CE-12	U+1	Zr+1	Exponential	Yes
CE-13	U+1	Pb+1	Exponential	No
CE-14	U+1	Pb+1	Exponential	Yes

Table 2. List of simulations conducted to examine charge exchange.

THIS PAGE INTENTIONALLY LEFT BLANK



## VII. RESULTS AND CONCLUSIONS

### A. OVERVIEW

The simulations all used cylindrical geometry with the debris loaded on the center axis with an initial radial velocity set at  $2 \times 10^8$  cm/s; this value was provided by LLNL as representative of the debris velocity. The undisturbed ambient magnetic field was set at 0.3 Gauss in the z direction. This geometry frames the problem of how streaming charged particles moved across the magnetic field lines.

#### 1. Simulations Examining Collisionless Shock Driven by Multiple Ion Species

Simulations completed to examine multi-species collisionless shock involved two separate debris species. However, to keep the energy constant, the two debris species had the same mass and used different charge states to represent the difference in their motion. The simulations began with both debris species having velocities of  $2 \times 10^8$  cm/s; using the same mass for the two debris species reduced the number of variables between simulations down to one. The principle under examination is the Larmor radius. As defined in equation 14, the charge state of the ion is the variable controlled to achieve different physical results. The hypothesis tested was the effect of the species with the smaller gyroradius (represented in this case as the one with the higher charge state) on the motion of the species with the larger gyroradius.

The simulations in this portion of the work all used uranium ions with various charge states. After testing the code in simple scenarios to ensure the multiple species were handled correctly, initial runs included two different charge states of uranium to represent separate species. In these simulations, it was easy to observe the correct behavior of the different species of uranium, and these runs confirmed ZMR's ability to handle multiple species.

Following the initial simulations where the results were intuitive, follow-on simulations involved uranium ions with non-trivial charge states to analyze the multi-species effects. In each of these simulations, one of the uranium ions was at the +1 state

(providing the longer gyroradius) while the other species of uranium had a charge state of +2, +4 or +8. These charge states are characterized by ionic motion with successively smaller Larmor radii.

There were two different configurations of the uranium ions in terms of initial location. In the first configuration, all the debris was collocated at the beginning of the simulation. This caused the debris to be co-mingled at the start of the simulation and stream out radially at a constant initial velocity. In the second configuration, the debris was staggered with the higher charge state ions on the outside and the lower charge state ions on the inside. This replicates a debris configuration with the lighter debris streaming outward in front of the heavier debris.

## **2. Simulations Completed Examining Charge Exchange**

Simulations completed to examine charge exchange involved two separate debris species. Buffering problems with ZMR prevented using more than two initial debris species. The simulations began with the debris species having a radial velocity of  $2 \times 10^8$  cm/s. The principle examined in these simulations involved charge exchange with the ambient atmosphere. As Figure 4 shows, the most prominent gas at the elevation of STARFISH is neutral, atomic oxygen so that is the catalyst for all charge exchange calculations. The simulations always used uranium +1 as a debris species and those simulations that used two debris species included of the following additional ions: xenon +1, zirconium +1 or lead +1. These debris ions were chosen as being representative of the likely fission products produced in nuclear fission.

To evaluate the effects of charge exchange, the simulations were first run with charge exchange disabled and the debris moving under normal kinematics as charged particles. The number densities of the debris and background ions were adjusted to ensure the debris species coupled with the background ions. Then the same simulation was completed with charge exchange enabled. These two simulations were compared and the differences related to charge exchange and the movement of the atoms as neutral particles allowing for the examination of the role of charge exchange.

There were two different configurations of the neutral, atomic oxygen used as catalyst for the charge exchange. This neutral, atomic oxygen represents the un-ionized portion of the atmosphere and not the ionized portion of the atmosphere that constitutes the background plasma. The neutral, atomic oxygen serves only as a catalyst for charge exchange and does not interact energetically with the debris species. Nor are there any calculations of motion for these catalyst atoms. The first configuration of neutral, atomic oxygen assumed a constant number density in the radial distance from the center of the simulation. Because ZMR has symmetry in the angular direction, no variable can have a dependence on  $\theta$ , the angle around the  $z$  axis. Therefore, the constant atmosphere is a good model over a short simulation grid. The exponentially decaying atmosphere matches the data plotted in Figure 4. However, since ZMR takes the debris which is streaming out isotropically and resets its motion in one dimensional radially outward, the exponential atmosphere discounts the debris which should be streaming down into the atmosphere; these debris would hit a denser atmosphere and generate more collisionless shock. Using an exponential atmosphere underestimates the amount of collisionless shock generated. Since neither the constant atmosphere or the exponential atmosphere are perfect models to use in ZMR, both atmospheric profiles were simulated to bound the results. Both atmospheric profiles allow for the examination of the relevant physics of collisionless shock generated by multiple species and charge exchange. It should be stated that ZMR was chosen for its relatively short simulation run times and accurate representation of the kinetic effects on ions and these advantageous features over compensate for the slight irregularities with the atmospheric profiles.

## **B. MULTISPECIES COLLISIONLESS SHOCK**

The hypothesis of collisionless shock with multiple debris species involved the lighter debris generating the shock and accelerating the heavier debris as it moved through that shock front. This hypothesis was simulated in two different geometries. In the simulations, instead of varying the mass, the charge state was varied to adjust the Larmor radius according to equation 14. Changing the charge state ensured the energy and number densities in the simulations remained constant across the different computer

runs. Changing the charge state produces the multi-species effect while reducing the number of variables to be considered.

### **1. Debris Co-Located**

Figure 18 shows the expansion of a multiple species debris plasma with two different charges, one with charge state +1 and the second with charge state +2. Correspondingly, their gyroradii differ by a factor of 2. This physics is similar to the case of two species both having a charge state +1 where one species is half the mass of the other. Manipulating charge state is an easier method to investigate multiple species while keeping the energy and number densities constant. In these simulations, neither debris species couples into the background and both species turn with a normal gyroradii. An acceleration of the debris would be observed as a jump in radial velocity. In the phase space plot shown in Figure 17, a jump in radial velocity would be observed as a vertical shift upwards in the simulation particles' radial velocity. Figure 17 shows both debris species ( $U^{+1}$  and  $U^{+2}$ ) having smooth curves to their motion in phase space and therefore not showing acceleration.

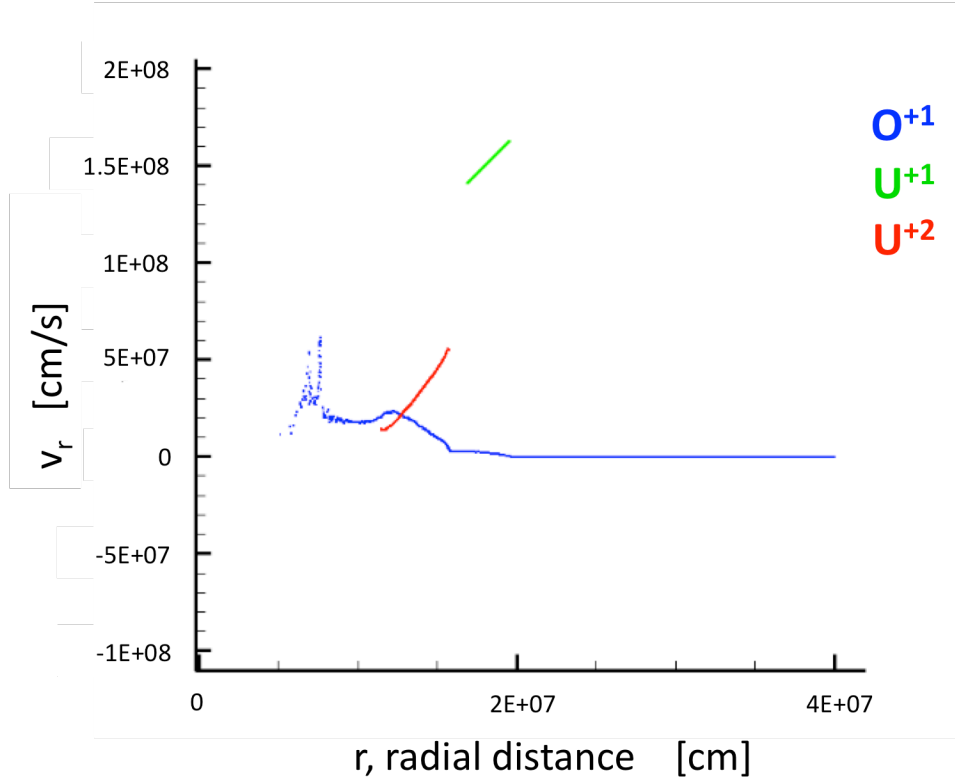


Figure 17. Simulation of two uranium debris species with charge states +1 (green) and +2(red) expanding into a background plasma of O+1 (blue) plotted as a radial velocity [cm/s] versus radial distance [cm]. The smooth profile for uranium +1 indicates no acceleration.

As the charge state increases to +4 and above in subsequent simulations, the higher charge state debris (i.e., the species with the smaller Larmor radius) couples into the background, but the debris with charge +1 never does. Using Hewett's coupling constant from equation 30 and the densities and charge states for the two debris species and the background species, the value of  $\alpha_{DC}$  is 1.35, greater than the decoupling threshold of 1.0. Therefore, the expectation is the debris will couple with the background. Figure 18 shows the higher charge state debris ( $U^{+4}$ ) coupled behind the background plasma ( $O^{+1}$ ) as expected. However, the lower charge state debris ( $U^{+1}$ ) does not have an increase in radial velocity. The phase space plot in Figure 18 shows a smooth profile for radial velocity for  $U^{+1}$  indicating no acceleration.

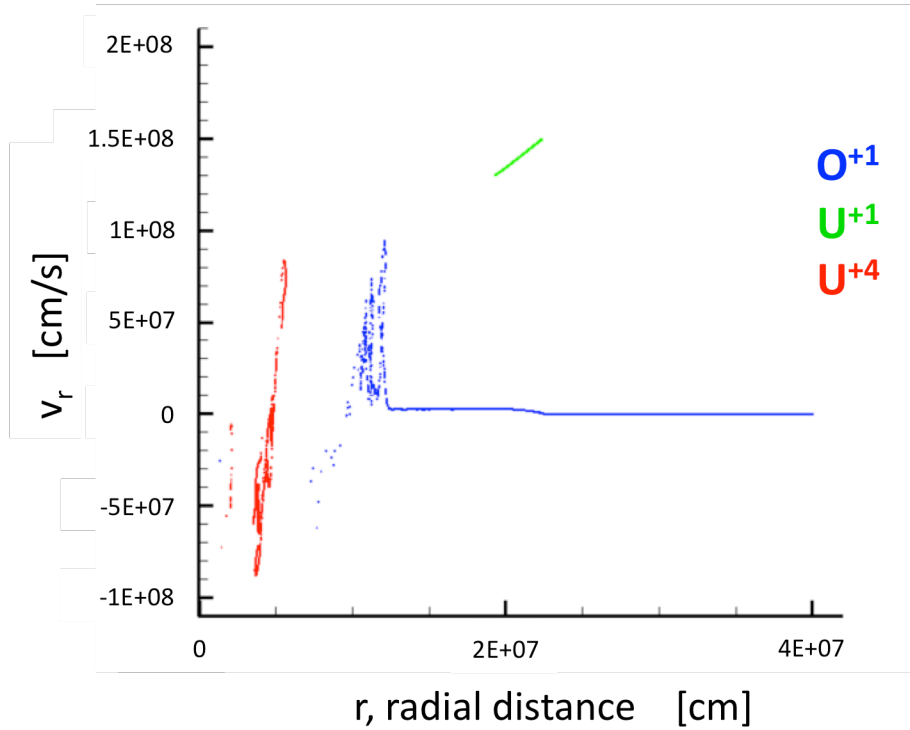


Figure 18. Simulation of two uranium debris species with charge states +1 (green) and +4 (red) expanding into a background plasma of O+1 (blue) plotted as a radial velocity [cm/s] versus radial distance [cm]. The smooth profile for uranium +1 indicates no acceleration.

As the charge state for the debris species increases, beyond +4, the observed trends continue with the higher charge state coupling into the background and the debris at charge state +1 continues to remain uncoupled. Figure 19 shows the results run at the highest charge state of +8, which corresponds to the same Larmor radius of  $\text{Si}^{+1}$ . Again, the higher charge state debris ( $\text{U}^{+8}$ ) coupled behind the background the background plasma ( $\text{O}^{+1}$ ). The phase space plot in Figure 19 shows a smooth profile for radial velocity for  $\text{U}^{+1}$  indicating no acceleration.

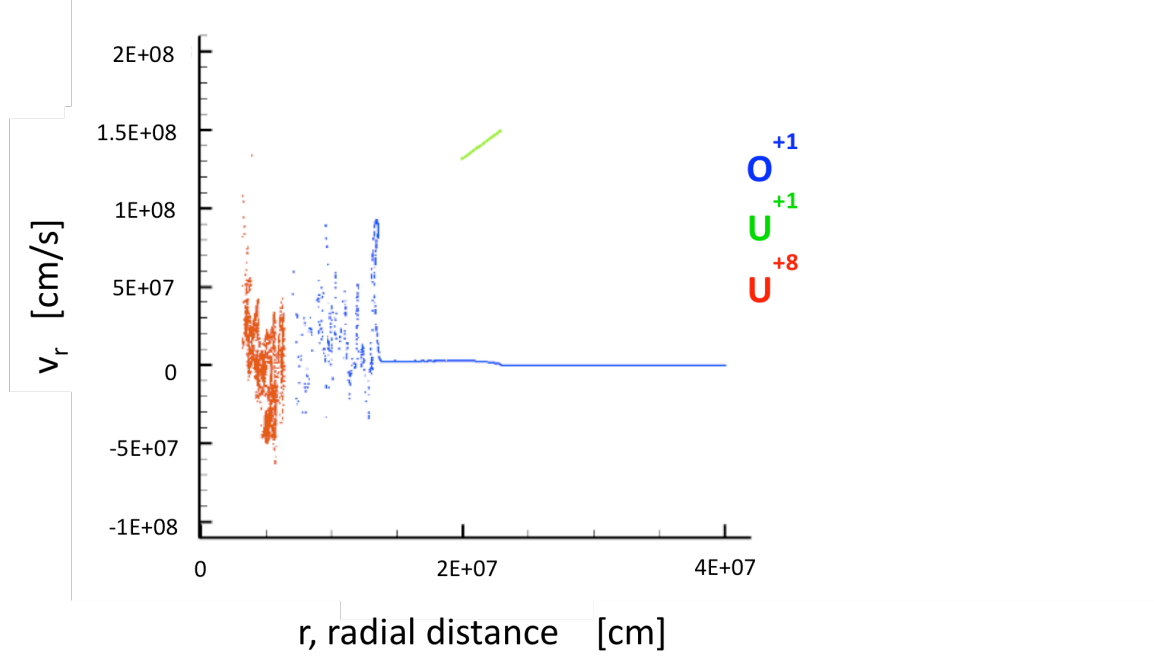


Figure 19. Simulation of two uranium debris species with charge state +1 (green) and +8 (red) expanding into a background plasma of O+1 (blue) plotted as a radial velocity [cm/s] versus radial distance [cm]. The smooth profile for uranium +1 indicates no acceleration.

With the two debris species co-located at the beginning of the simulation, the higher charged debris species (corresponding to a smaller gyro-radii element at charge state +1) did not generate a collisionless shock sufficient to accelerate the uranium +1 debris species.

## 2. Debris Staggered

To account for the geometry and allow the higher charge debris to precede the lower charge state debris, the simulations were rerun with debris staggered. As discussed in section VI.D.1, the higher charge state debris began the simulation in a shell outside of the lower charge state debris. As the simulation began, all the debris pushes into the charged background plasma. Figure 20 shows that two debris species with charge states +1 and +2 expanding into the background plasma of  $O^{+1}$ . Based on the decoupling constant (equation 30), these two debris species are decoupled from the background.

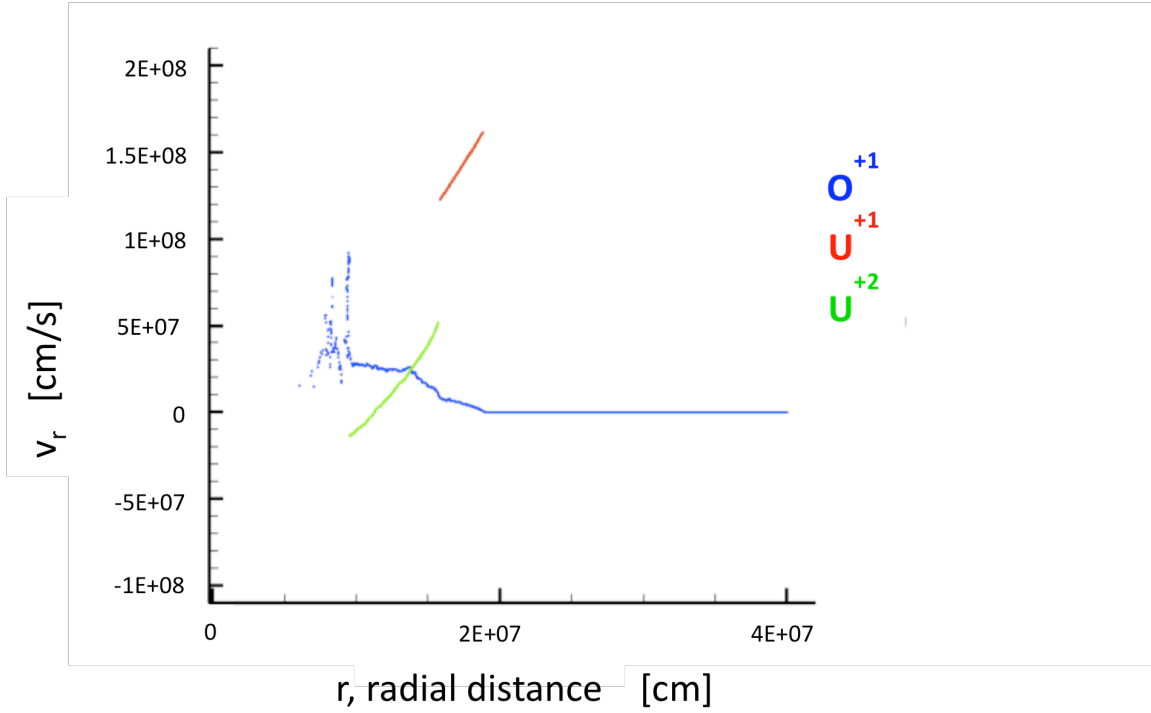


Figure 20. Simulation of two uranium debris species with charge state +1 (red) and +2 (green) expanding into a background plasma of O+1 (blue) plotted as a radial velocity [cm/s] versus radial distance [cm]. The smooth profile for uranium +1 indicates no acceleration.

The results are similar to the co-located results (Figure 17). In the staggered simulation, the  $U^{+2}$  begins outside the  $U^{+1}$  and spends more time interacting with the ambient magnetic field. The  $U^{+1}$  debris follows behind the  $U^{+2}$  and passes through the collisionless shock generated by the  $U^{+2}$ . However, in Figure 20, the profile of the radial velocity for  $U^{+1}$  remains smooth showing no acceleration.

As the charge state of the outside debris species increases to +4, the results mirror the co-located scenarios. Figure 21 shows the  $U^{+4}$  coupled inside the background plasma with the  $U^{+1}$  not trapped inside the background.



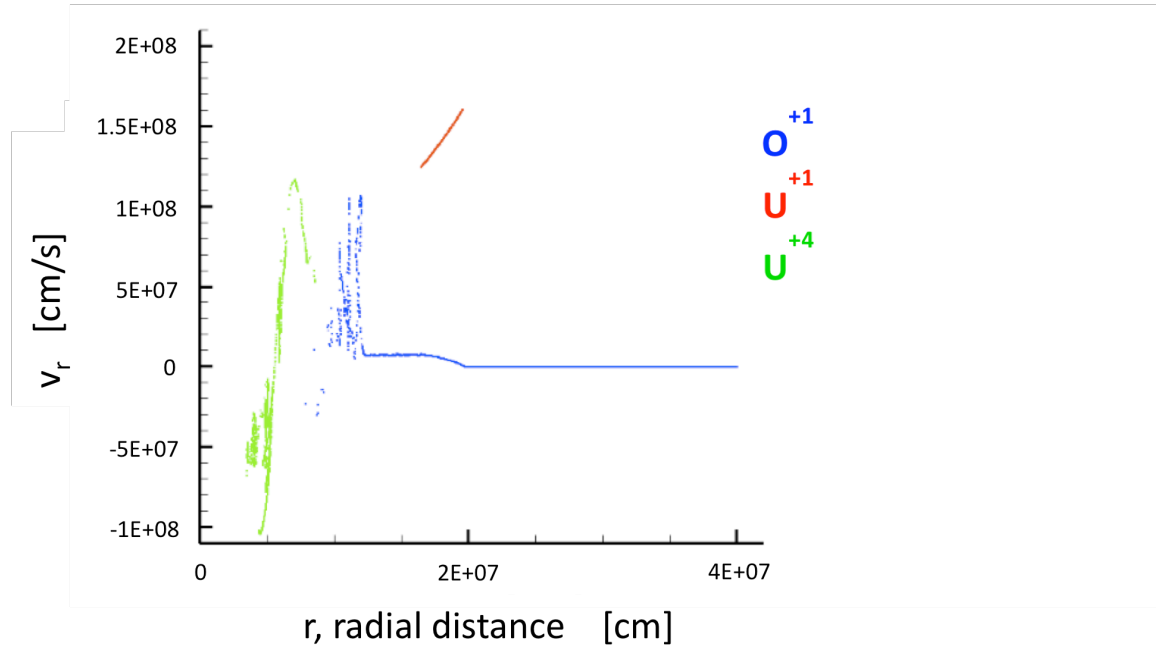


Figure 21. Simulation of two uranium debris species with charge state +1 (red) and +4 (green) expanding into a background plasma of O+1 (blue) plotted as a radial velocity [cm/s] versus radial distance [cm]. The smooth profile for uranium +1 indicates no acceleration.

As shown in Figure 21,  $U^{+1}$  has a smooth profile in radial velocity indicating no acceleration from the collisionless shock formed by the  $U^{+4}$ . Similarly, as the charge state of the debris species increases to +8, the inside debris species remains decoupled as seen in Figure 22. Again, the  $U^{+1}$ , which represents a larger gyroradius, maintains a smooth profile for the radial velocity in phase space. Figure 22 shows no indication of acceleration due to the collisionless shock formed by the  $U^{+8}$  (representing a smaller gyroradius).

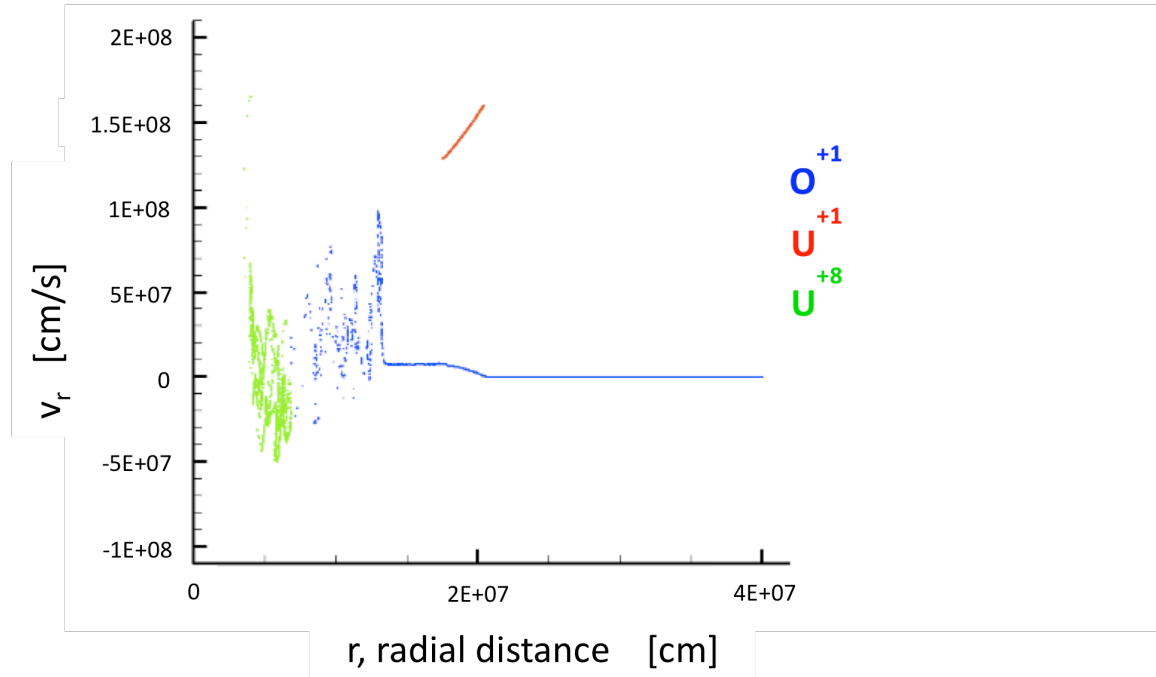


Figure 22. Simulation of two uranium debris species with charge state +1 (red) and +8 (green) expanding into a background plasma of O+1 (blue) plotted as a radial velocity [cm/s] versus radial distance [cm]. The smooth profile for uranium +1 indicates no acceleration.

This simulation did not support the hypothesis that the smaller gyroradius debris would drive the collisionless shock and accelerate the larger gyroradius debris. The simulation suggests the debris species interact independently with the ambient magnetic field and the background plasma. Even with the debris staggered at the beginning of the simulation, the smaller gyroradius debris did not form a collisionless shock large enough to accelerate the larger gyroradii debris.

### C. CHARGE EXCHANGE

The effects from charge exchange were examined using the same initial conditions for a multi-species simulation where the debris coupled with the shock front and remained inside the background ions. That is, as the simulation progressed all the debris stayed behind the shock front and expended all its energy driving the shock. These same initial conditions were simulated with charge exchange enabled. Since the initial

simulation had 100% of the debris coupled inside the background plasma, any debris now ahead of the shock front is attributed to the effects of charge exchange.

## **1. Sensitivity**

The sensitivity of the number of neutral atoms produced to the cross sections was examined. The sensitivity of the cross section for both electron capture and electron loss was examined independently. First the cross section for electron capture was scaled by a factor of two, then five and finally ten. The total number of neutral atoms at the end of the simulation scaled up accordingly. Secondly, the cross section for electron loss was scaled by a factor of two, then five and finally ten. Then the total number of neutral atoms at the end of the simulation scaled down accordingly. As expected, the total number of neutrals produced directly scales with the values of the cross sections for both electron capture and electron loss computed by the semi-empirical formula.

The sensitivity of the cross sections is important because the semi-empirical formula does not exactly match the experimental data. If better semi-empirical formulas for the cross sections of the elements of interest are found, they could easily be implemented in the simulation. The values determined from the semi-empirical here are used to demonstrate the relevant physics of charge exchange.

## **2. Effects of Collisionless Shock on Charge Exchange**

The impact of collisionless shock on charge exchange was examined. The simulation was run without a charged background plasma using neutral hydrogen as the background material. The neutral oxygen profile was also loaded and charge exchange enabled. This caused the expanding debris of  $U^{+1}$  to stream radial outward and without the charged background plasma there is no coupling between the debris plasma and the background so there is no kinetic energy transferred to the background plasma by shock formation. As the charged background passes through the neutral oxygen profile, charge exchange occurs but without any impact from collisionless shock (which is absent due to the lack of a charge background). The total number of neutral uranium atoms as a function of time is shown in Figure 23. The shape of the results plotted in Figure 23 match the expectation from equation 49 and theoretical calculation plotted in Figure 15.

The importance of Figure 23 is the value of the total number of real, neutral uranium atoms produced in the simulation.

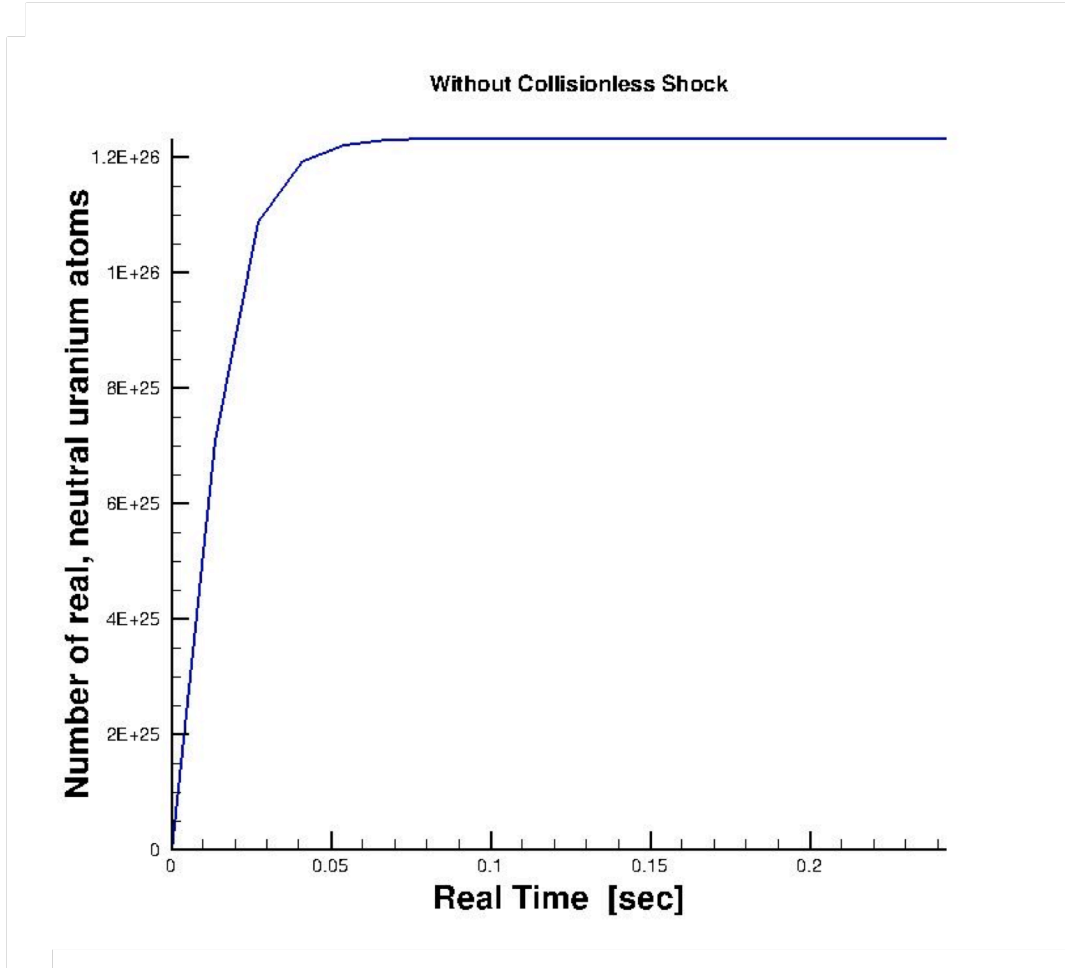


Figure 23. Simulation of uranium+1 expanding into a background of neutral hydrogen without generating a collisionless shock and with charge exchange enabled.

The same conditions were used in another simulation however in this case the background plasma was switched from neutral hydrogen back to  $O^{+1}$ . The charged background and the ambient magnetic field interact with the expanding debris ions ( $U^{+1}$ ) generating a collisionless shock. Again, the neutral oxygen profile remained on the grid and charge exchange was enabled. The difference between the two simulations was only the formation of the collisionless shock. The simulation results of the number of real, neutral uranium atoms plotted as a function of time is shown in Figure 24. Again, the data

plotted in Figure 24 matches the form expected from equation 49 and the late time value of the total number of neutral uranium atoms produced is important.

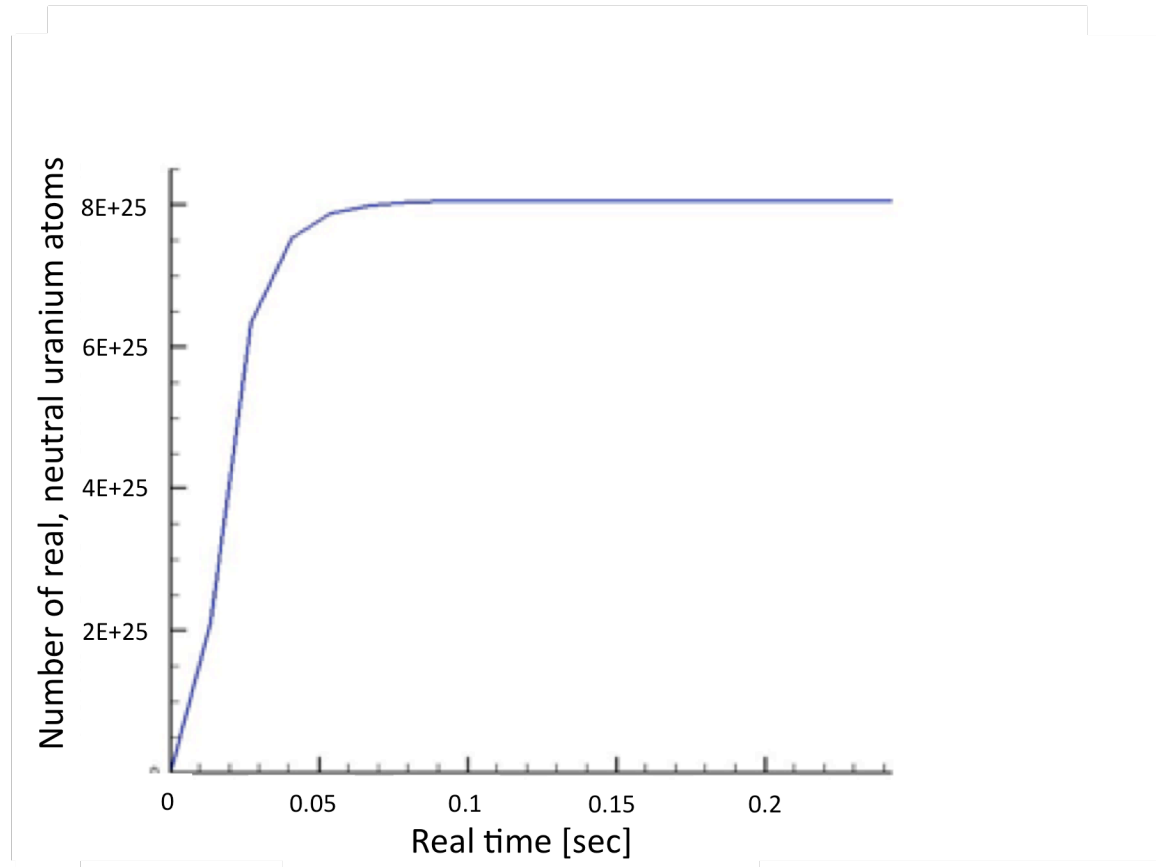


Figure 24. Simulation of uranium+1 expanding into a background of oxygen+1 while generating a collisionless shock and with charge exchange enabled. Plot of number of real, neutral uranium atoms as a function of time.

The simulations were similar except for the collisionless shock. Both began with the same energy and only the collisionless shock moved energy from the debris to the background plasma. Both simulations reached a steady state of neutral uranium in about 0.06 seconds however, the steady state values for the two simulations were different. The simulation without collisionless shock reached a steady state value of  $1.26 \times 10^{26}$  atoms of neutral uranium and the simulation with collisionless shock reached a steady state value of  $8 \times 10^{25}$  atoms of neutral uranium. While the absence of a collisionless shock caused an increase of 33% in the number of neutrals, the net change in velocity with and without collisionless shock was only 1%. Without collisionless shock and no mechanism for

energy exchange between the debris ions and the background, the debris ions lost no energy or velocity to the background and maintained their velocity of  $2 \times 10^8$  cm/s. With collisionless shock and a mechanism to exchange energy between the debris ions and the background ions, the average speed of the neutral particles was  $1.98 \times 10^8$  cm/s. The probability of charge exchange is calculated using equation 34 and includes cross section, speed, size of the time step, and number density of the target (neutral oxygen). Additionally, the cross section is energy dependent and is influenced by the debris ion's speed. A decrease of 1% in velocity changes the cross section for electron capture by 5% and changes the cross section for electron loss by 3%. Both with and without collisionless shock, the size of the time step and the number density profile of the target atoms is the same. Neither the size of the time step nor the number density profile of the target atoms accounts for the difference between the numbers of neutrals produced for the simulations with and without collisionless shock.

Collisionless shock introduces an electric field in the angular direction that turns the debris ions from their original radial path. The angular electric field is small and the overall effect on the speed is small; hence the only 1% difference in the speeds. However, the speed is the vector sum of the components of the velocity vector. While the magnitude of the velocity is the same, the velocity components have shifted with a larger theta velocity. Due to the turning, the debris ions are no longer streaming radially through an exponentially decreasing atmosphere with a decreasing number density of target atoms (neutral oxygen). Instead, as the debris ions turn in the presence of a transverse electric field, the debris ions move through a higher number density of target atoms and undergo more charge exchange before the charge exchange “freezes out.”

### **3. Constant and Exponential Atmosphere**

As described in Chapter V.C, the simulations were run with both a constant and exponential atmosphere and there are different results in slip through for each atmosphere. The different atmospheric profiles produced dramatically different results in the amount of slip through. In cylindrical geometry, neither atmospheric representation is a correct representation of the actual atmosphere; however, this work shows there is a

clear difference in the results and the appropriate atmospheric model should be used. Future work in three dimensions should include more accurate atmospheric model.

#### 4. Slip through with Constant Atmosphere

The results described in this section are from simulations using a constant atmosphere for both the background plasma ( $O^{+1}$ ) and the neutral oxygen background ( $O^{+0}$ ).

##### a. Uranium Only

These simulations show the effects of charge exchange, demonstrate the results and describe the process that will be repeated when a second debris species is added in later simulations. The simulation included one Uranium debris species with a charge state of +1. In the first simulation there was no charge exchange. The debris began with an initial radial velocity of  $2 \times 10^8$  cm/s which corresponds to a kinetic energy representative of 0.29 MT yield. Without charge exchange, the debris couples with the background ions as seen in Figure 25.

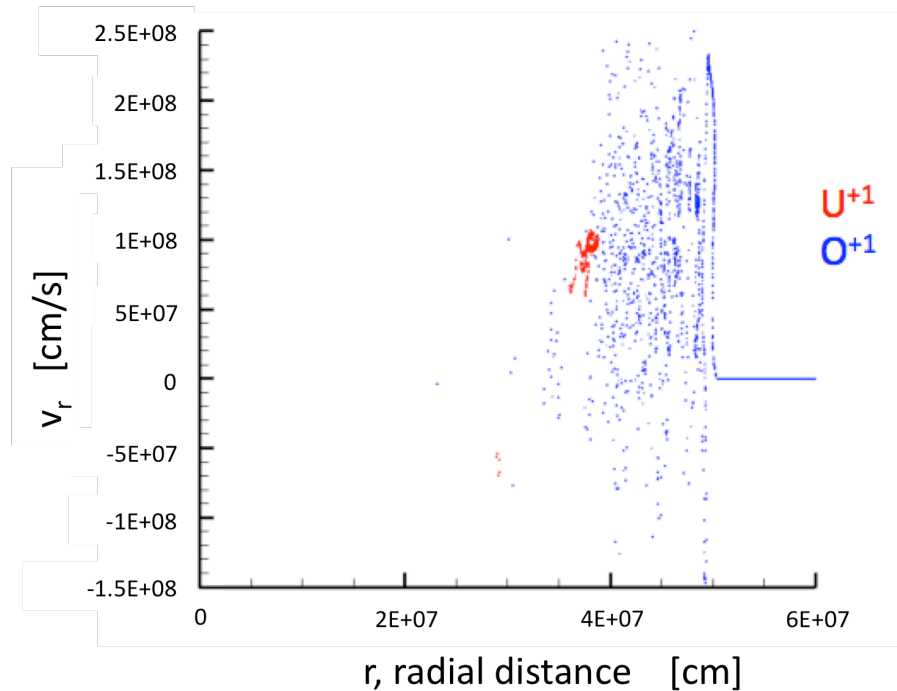


Figure 25. Simulation of Uranium+1 (red) expanding into background plasma of Oxygen+1 (blue) in a constant atmosphere without charge exchange.

The simulation was rerun again with only one debris species of  $U^{+1}$  but with charge exchange enabled. During this simulation, particles experienced charge exchange of both electron capture and electron loss. All other inputs were kept the same. Figure 26 shows different results from charge exchange with some of the uranium atoms slipping ahead of the shock front in the background plasma. The comparison between Figures 25 and 26 show the clear difference the effects from simulations run with charge exchange, specifically how much further down the simulation grid the debris travels and how some debris clearly is decoupled from the background plasma.

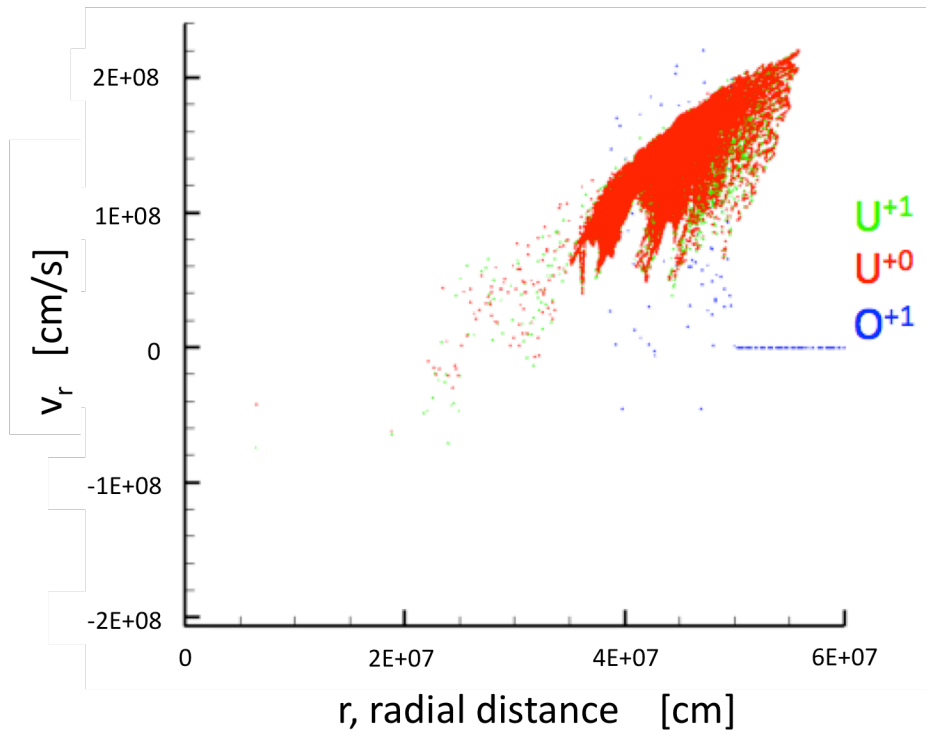


Figure 26. Simulation of Uranium+1 expanding into background plasma of Oxygen+1 in a constant atmosphere with charge exchange.

Enabling charge exchange allowed some debris to slip ahead of the shock front. Since the initial simulation without charge exchange resulted in all the debris behind the shock front, this makes an easy comparison to see the effects of charge exchange. Charge exchanged allowed 1.02% of the debris to slip ahead of the shock front with most of the



slip-through debris being in the neutral charge state. A comparison of the results between the two simulations with  $U^{+1}$  as the debris species is shown in Table 3 with the last two columns showing the amount of real atoms that slipped ahead of the magnetic shock front at the completion of the simulation.

	<b>Total # of <math>U^{+1}</math> ions (t=0)</b>	<b>Total # of <math>U^{+0}</math> atoms (t=0)</b>	<b>Total # of <math>U^{+1}</math> ions ahead of shock front (t=5000)</b>	<b>Total # of <math>U^{+0}</math> ions ahead of shock front (t=5000)</b>
Without Charge Exchange	$1.70 \times 10^{27}$	0	0	N/A
With Charge Exchange	$1.70 \times 10^{27}$	0	$5.18 \times 10^{23}$	$1.69 \times 10^{25}$

Table 3. Comparison of slip through data without and with charge exchange for uranium.

Figures 25 and 26 illustrate significant differences in simulation outcomes (though it should be noted that Figure 26 includes more points plotted than Figure 25). Both simulations have the same number of particles and energy. However, the use of the charge exchange function in ZMR creates new simulation particles and reduces the real-particle-per-simulation particle value. Therefore, Figure 26 has more points plotted but each point represents fewer real particles in the simulation. The same effect will occur for all simulations involving charge exchange and all those graphs will have more points plotted at the completion of the simulation than the corresponding runs without charge exchange.

#### ***b. Uranium and Xenon***

The next set of simulations includes uranium and xenon both at charge state +1. Again, the debris began the simulation with an initial velocity of  $2 \times 10^8$  cm/s in the radial direction. The kinetic energy representative of a 0.29 MT yield. At the completion of the simulation with charge exchange disabled, the debris is coupled to the background plasma. Figure 27 shows the debris of  $U^{+1}$  (light blue) and  $Xe^{+1}$  (red) behind the background plasma  $O^{+1}$  (blue). Without charge exchange, 100% of the debris couples to the background plasma and none of the debris gets ahead of the shock front.

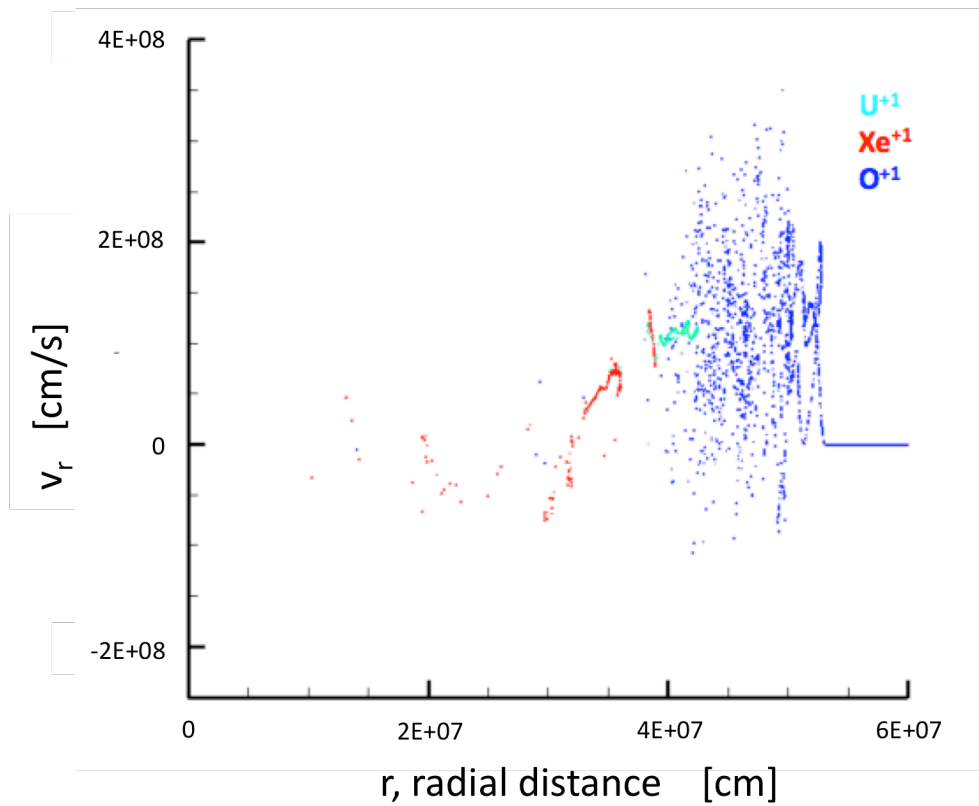


Figure 27. Simulation involving Uranium+1 (light blue) and Xenon+1 (red) expanding into background plasma of Oxygen+1 with a constant atmosphere without charge exchange.

The simulation was run again with charge exchange enabled. All the other parameters were kept constant. The simulation allowed the  $U^{+1}$  ions to neutralize to  $U^{+0}$  and later re-ionize back to  $U^{+1}$ . The same was true to the  $Xe^{+1}$  ions. Figure 28 shows the results of the simulation at its completion with some of the debris ahead of the shock front. The comparison between Figures 27 and 28 show the difference charge exchange contributes to the results with two species.

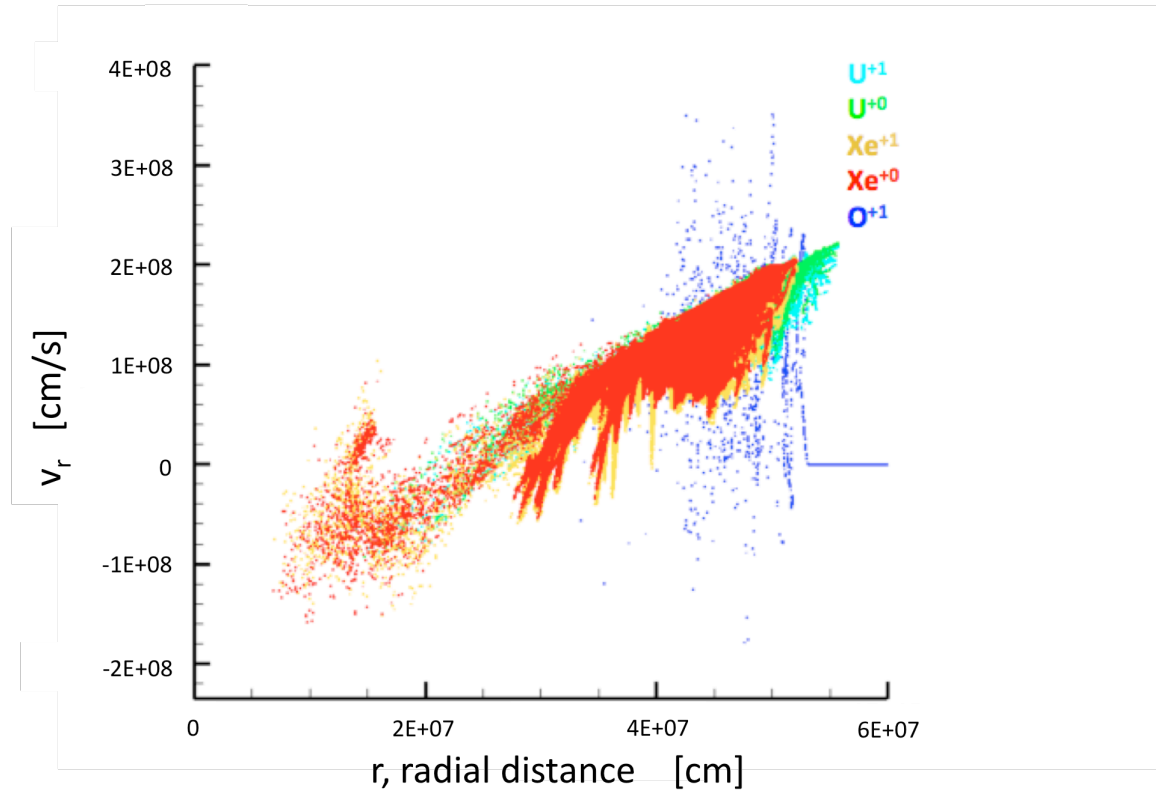


Figure 28. Simulation involving Uranium+1 (light blue) and Xenon+1 (gold) expanding into a background plasma of Oxygen+1 with a constant atmosphere and charge exchange enabled.

Without charge exchange, all the debris coupled inside the background plasma and none was in front of the shock front. With charge exchange, some of the debris was able to move in front of the shock front and beyond the background plasma. Charge exchange resulted in 0.33% of the debris ending in front of the shock front. Table 4 shows the results of the two simulations containing U and Xe as debris with charge exchange disabled and then again with charge exchange enabled. The last four columns of Table 4 show the number of atoms that moved beyond the shock front at the completion of each simulation.

	Total # of U <sup>+1</sup> ions (t=0)	Total # of Xe <sup>+1</sup> ions (t=0)	Total # of U <sup>+0</sup> atoms (t=0)	Total # of Xe <sup>+0</sup> atoms (t=0)	Total # of U <sup>+1</sup> ions ahead of shock front (t=5000)	Total # of Xe <sup>+1</sup> ions ahead of shock front (t=5000)	Total # of U <sup>+0</sup> ions ahead of shock front (t=5000)	Total # of Xe <sup>+0</sup> ions ahead of shock front (t=5000)
Without Charge Exchange	1.41x10 <sup>27</sup>	2.81x10 <sup>26</sup>	0	0	0	0	NA	NA
With Charge Exchange	1.41x10 <sup>27</sup>	2.81x10 <sup>26</sup>	0	0	1.25x10 <sup>23</sup>	7.94x10 <sup>21</sup>	4.34x10 <sup>24</sup>	6.49x10 <sup>23</sup>

Table 4. Comparison of slip through data for uranium and xenon without and with charge exchange in a constant atmosphere.

*c. Uranium and Zirconium*

The next set of simulations included both uranium and zirconium as debris species with charge state +1. Again, the debris began the simulation with a velocity of  $2 \times 10^8$  cm/s in the radial direction. The kinetic energy of the debris was representative of a 0.29 MT yield. At the completion of the simulation with charge exchange disabled, the debris had coupled inside the background. Figure 29 shows the debris species coupled to the background plasma at the completion of the simulation.

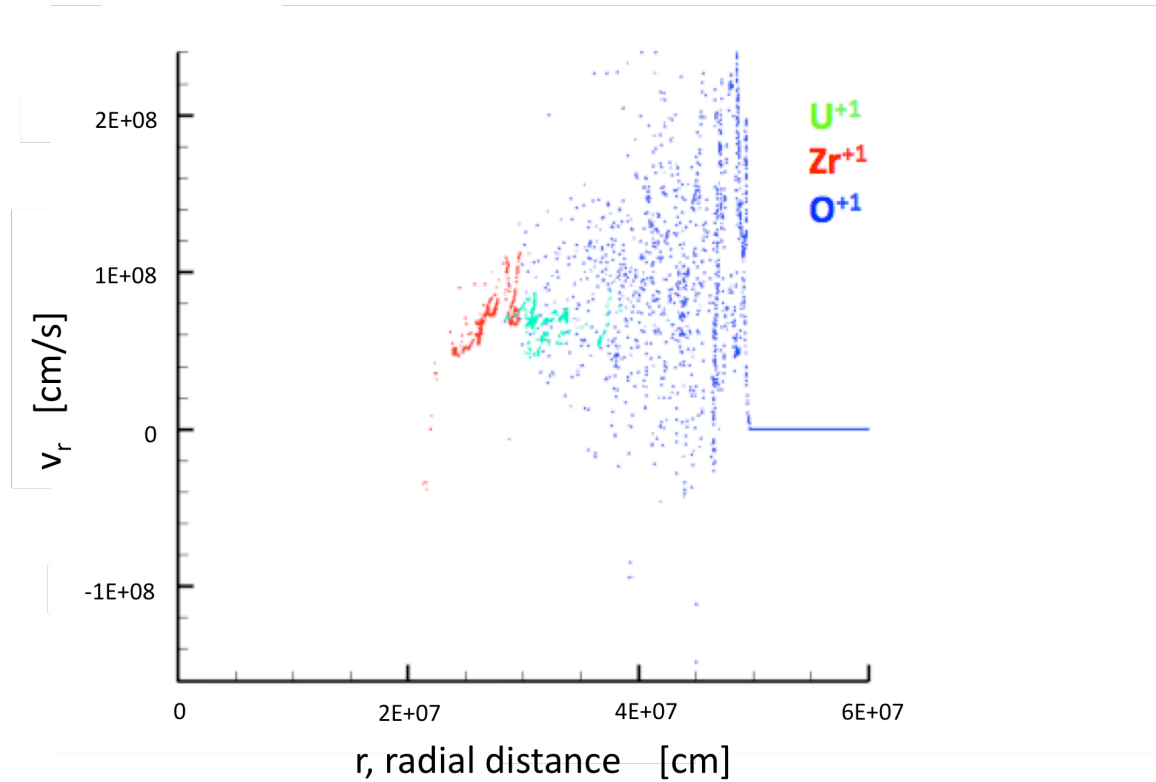


Figure 29. Simulation involving Uranium+1 (green) and Zirconium+1 (red) expanding into a background plasma of O+1 (blue) with a constant atmosphere without charge exchange.

The simulation was rerun with all the same parameters and charge exchange enabled. With charge exchange, some of the debris was neutralized and slipped ahead of the shock front. Figure 30 shows the results of the simulation with charge exchange enabled. A comparison of Figures 29 and 30 show the difference charge exchange contributes to the results with two species.

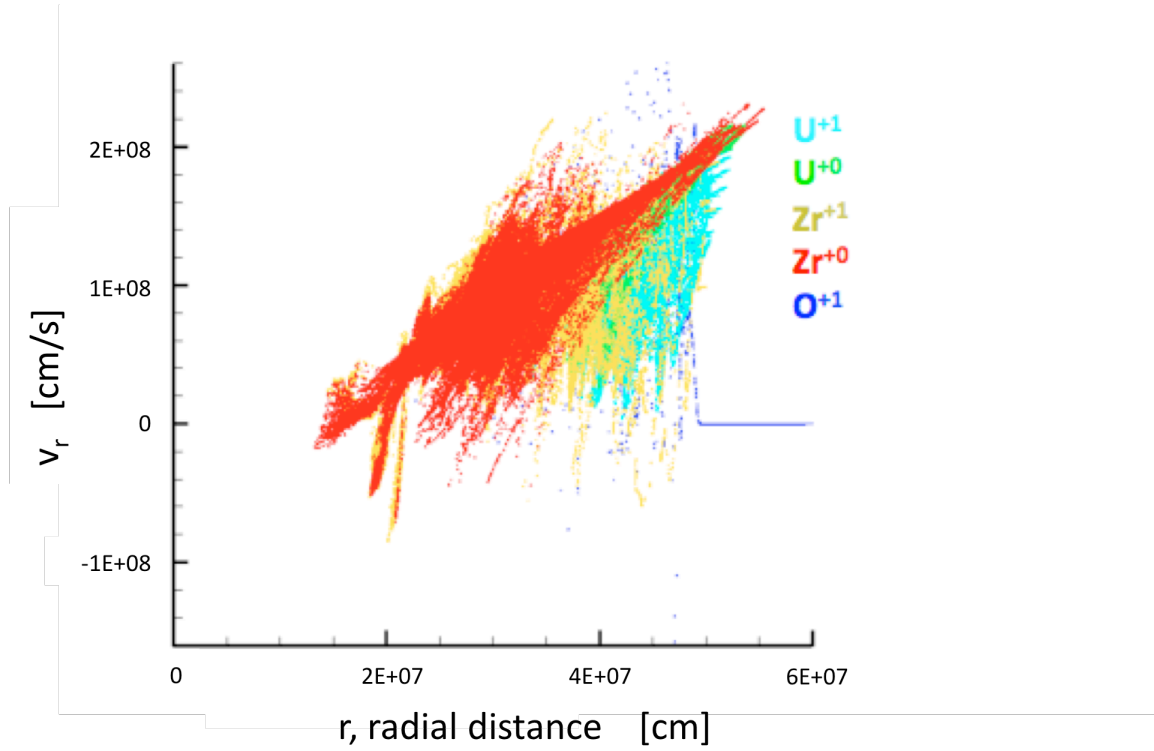


Figure 30. Simulation involving Uranium+1 (light blue) and Zirconium+1 (gold) expanding into a background plasma of O+1 (blue) with a constant atmosphere and charge exchange.

Enabling charge exchange in the simulation allowed 1.1% of the debris to slip ahead of the shock front. Table 5 shows the results of both simulations involving U and Zr at the completion of the simulations with charged exchange disabled and then again with charge exchange enabled. The last four columns of Table 5 show the difference in the number of atoms that slip beyond the shock front at the completion of the simulations.

	Total # of U <sup>+1</sup> ions (t=0)	Total # of Zr <sup>+1</sup> ions (t=0)	Total # of U <sup>+0</sup> atoms (t=0)	Total # of Zr <sup>+0</sup> atoms (t=0)	Total # of U <sup>+1</sup> ions ahead of shock front (t=5000)	Total # of Zr <sup>+1</sup> ions ahead of shock front (t=5000)	Total # of U <sup>+0</sup> ions ahead of shock front (t=5000)	Total # of Zr <sup>+0</sup> ions ahead of shock front (t=5000)
Without Charge Exchange	1.41x10 <sup>27</sup>	3.7x10 <sup>26</sup>	0	0	0	0	NA	NA
With Charge Exchange	1.41x10 <sup>27</sup>	3.7x10 <sup>26</sup>	0	0	5.74x10 <sup>23</sup>	3.31x10 <sup>22</sup>	1.40x10 <sup>25</sup>	2.31x10 <sup>24</sup>

Table 5. Comparison of slip through data without and with charge exchange for uranium and zirconium in a constant atmosphere.

***d. Uranium and Lead***

The next set of simulations includes both uranium and lead both at charge state +1. Again, the debris began the simulation with a radial velocity of  $2 \times 10^8$  cm/s and the total kinetic energy of the debris was representative of a 0.29 MT yield. At the completion of the simulation with charge exchange disabled, all the debris had coupled behind the shock front. Figure 31 shows the results at the completion of the simulation with charge exchange disabled.

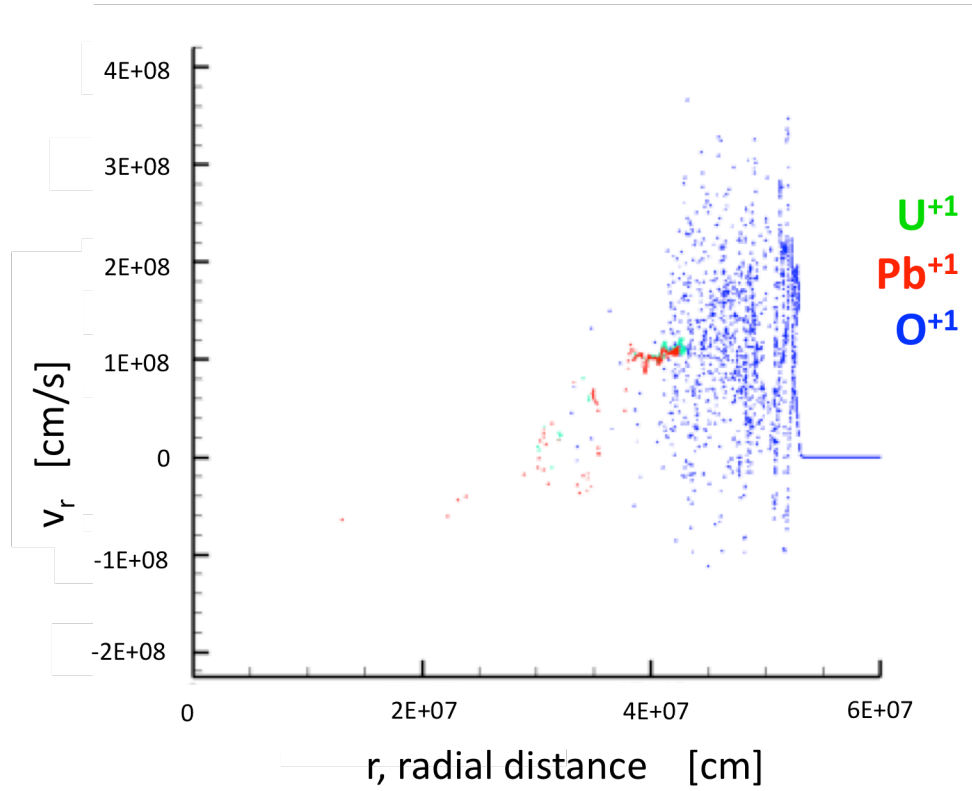


Figure 31. Simulation involving Uranium+1 (green) and Lead+1 (red) expanding into a background of Oxygen+1 (blue) with a constant atmosphere without charge exchange.

The simulation was rerun with all the same parameters with charge exchanged enabled. Figure 32 below shows the results of the simulation with charge exchange enabled. At the completion of the simulation, some of the debris was in front of the shock front. The comparison between Figures 31 and 32 shows the impact of charge exchange on the simulation results.



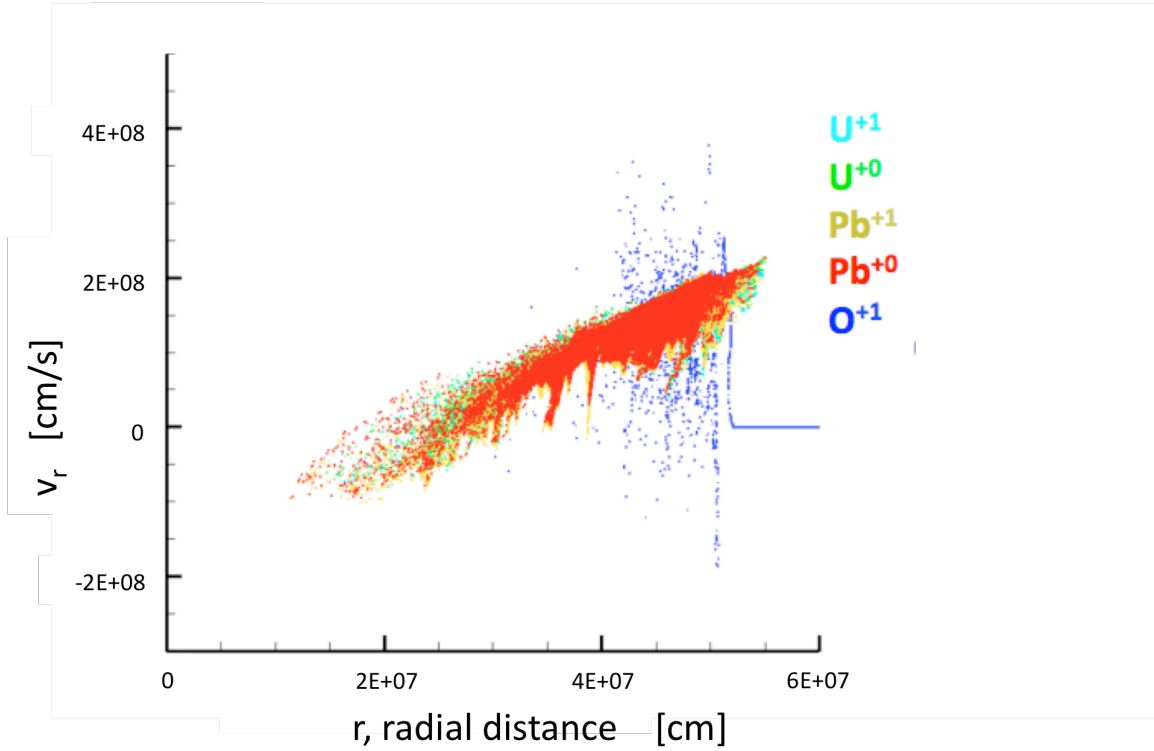


Figure 32. Simulation with Uranium +1 (light blue) and Lead+1 (gold) expanding into a background plasma of Oxygen+1 (blue) in a constant atmosphere with charge exchange.

Charge exchange enabled 1% of the debris to slip ahead of the shock front. Table 6 shows a comparison of the results of uranium and lead with charge exchange disabled and then with charge exchange enabled. The last four columns show the total number of atoms ahead of the shock front at the completion of the simulation.

	Total # of U <sup>+1</sup> ions (t=0)	Total # of Pb <sup>+1</sup> ions (t=0)	Total # of U <sup>+0</sup> atoms (t=0)	Total # of Pb <sup>+0</sup> atoms (t=0)	Total # of U <sup>+1</sup> ions ahead of shock front (t=5000)	Total # of Pb <sup>+1</sup> ions ahead of shock front (t=5000)	Total # of U <sup>+0</sup> ions ahead of shock front (t=5000)	Total # of Pb <sup>+0</sup> ions ahead of shock front (t=5000)
Without Charge Exchange	1.41x10 <sup>27</sup>	1.8x10 <sup>26</sup>	0	0	0	0	NA	NA
With Charge Exchange	1.41x10 <sup>27</sup>	1.8x10 <sup>26</sup>	0	0	6.31x10 <sup>23</sup>	4.41x10 <sup>22</sup>	1.44x10 <sup>25</sup>	1.31x10 <sup>24</sup>

Table 6. Comparison of slip through data without and with charge exchange for uranium and lead in a constant atmosphere.

## 5. Slip through with Exponential Atmosphere

### a. Uranium Only

The initial simulation examining charge exchange with the assumption of an exponential atmosphere involved only Uranium at charge state +1. The initial debris velocity was set at  $2 \times 10^8$  cm/s and the number density of U<sup>+1</sup> was set at  $7 \times 10^6$  part/cm<sup>3</sup>. This was set to have the single species couple inside the background plasma. It also corresponds to kinetic energy of a 0.25 MT yield. These initial conditions ensure the debris plasma will couple to the background plasma to show the impact of charge exchange on the final spatial distribution of the debris ions. It is motion of these debris ions, which will later beta decay and inject high-energy electrons, that is the foundation of this research. Figure 33 shows the results at the completion of the simulation with charge exchange disabled. Here all the debris is coupled with the background plasma.

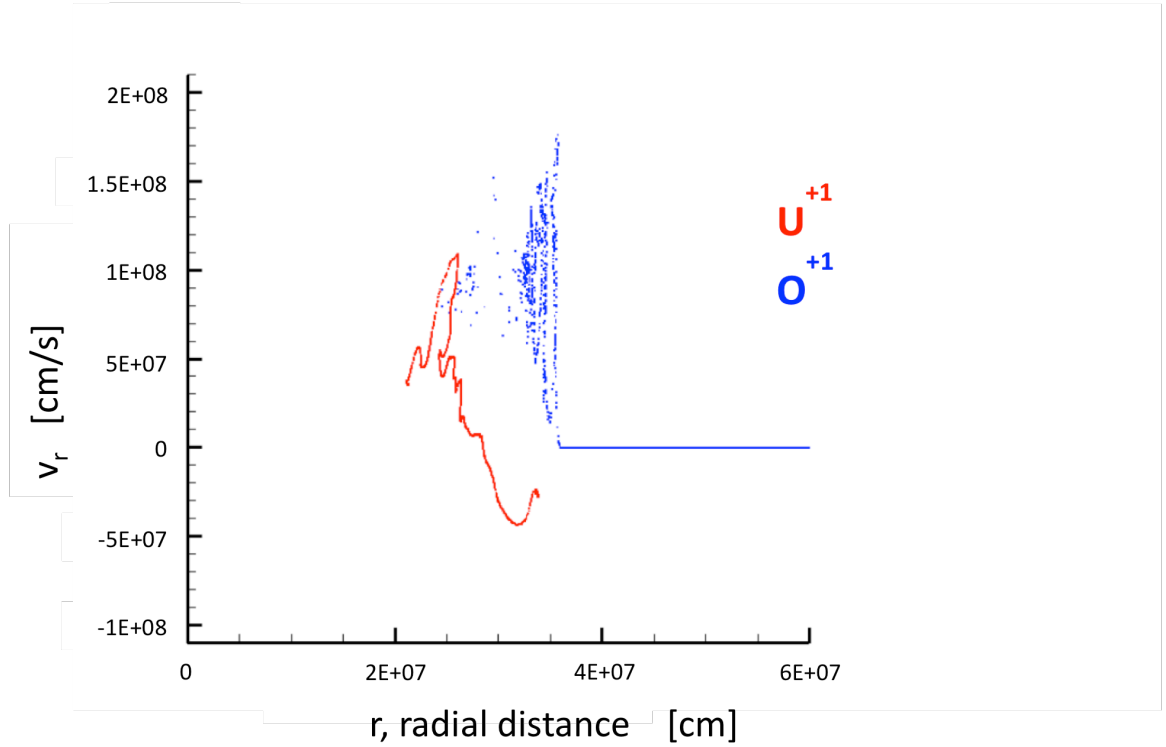


Figure 33. Simulation involving Uranium +1 (Red) into Oxygen +1 (Blue) without charge exchange where the debris couples into background.

The same simulation was run with charge exchange enabled. All the other parameters were kept the same. All the debris ions initially start at charge state +1. Figure 34 shows the phase space distribution at the end of the simulation. The debris ions of  $U^{+1}$  are plotted in green and the neutral uranium atoms ( $U^{+0}$ ) are plotted in red. The comparison between Figures 33 and 34 illustrates the impact of charge exchange on the results of the simulation. Figure 34 shows that some of the debris has slipped through the background plasma.

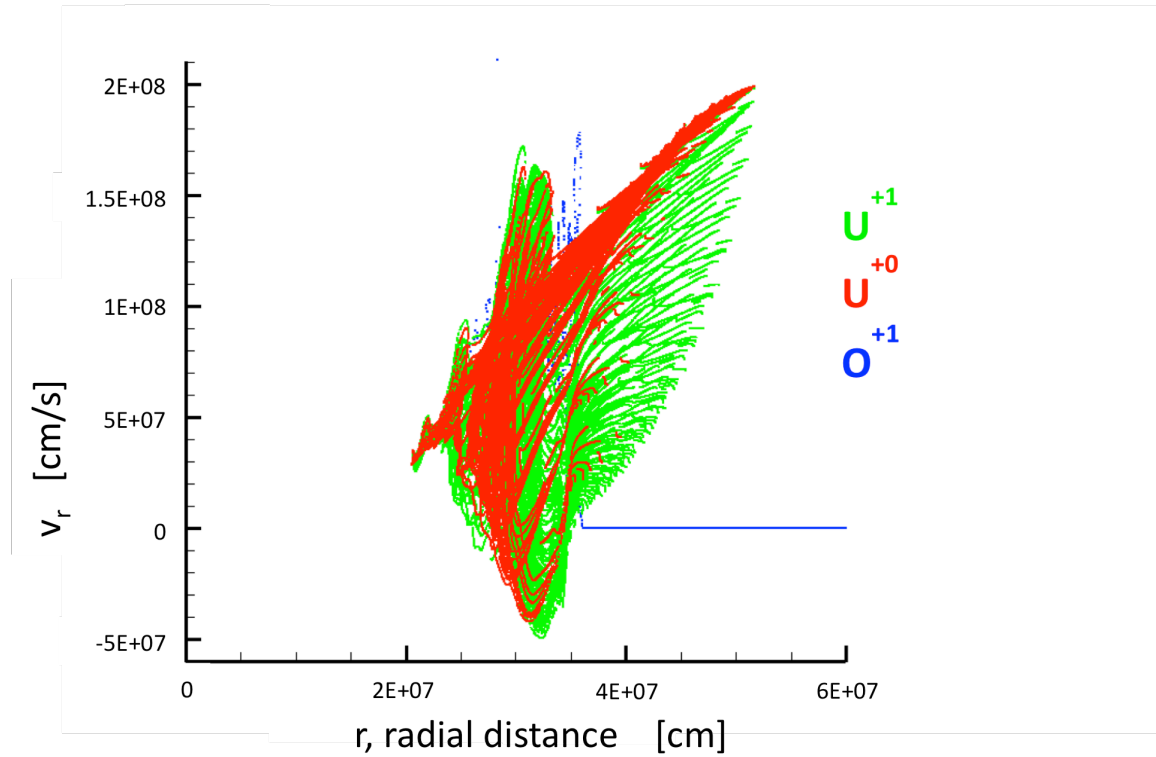


Figure 34. Simulation involving Uranium +1 (Green) into Oxygen +1 (Blue) with charge exchange forming neutral Uranium (Red) where some debris slips ahead of shock front.

With charge exchange enabled, 6% of the debris species (uranium) gets ahead of the shock front. The magnetic field shock front in the z component was defined as 0.4 Gauss. The total number of real particles in front of the shock front was calculated by ZMR. Without charge exchange, there is no mechanism to produce the  $U^{+0}$  atoms so they could not be in front of the shock front in the first simulation (second row of table). Table 7 shows the comparison between the simulations with charge exchange disabled and with charge exchange enabled. The last two columns show the number of atoms that slip ahead of the shock front.

	Total # of U <sup>+1</sup> ions (t=0)	Total # of U <sup>+0</sup> atoms (t=0)	Total # of U <sup>+1</sup> ions ahead of shock front (t=5000)	Total # of U <sup>+0</sup> ions ahead of shock front (t=5000)
Without Charge Exchange	1.37x10 <sup>27</sup>	0	0	NA
With Charge Exchange	1.37x10 <sup>27</sup>	0	8.35x10 <sup>23</sup>	8.78x10 <sup>25</sup>

Table 7. Comparison of slip through data without and with charge exchange for uranium.

***b. Uranium and Xenon***

Again, all the debris began the simulation with a speed of  $2 \times 10^8$  [cm/s] and the number densities were adjusted so the system had kinetic energy representative of a 0.25 MT yield. The simulation was first completed without charge exchange and the debris clearly coupled behind the shock front at the end of the simulation. Figure 35 shows both of the debris species coupled behind the background plasma at the completion of the simulation.

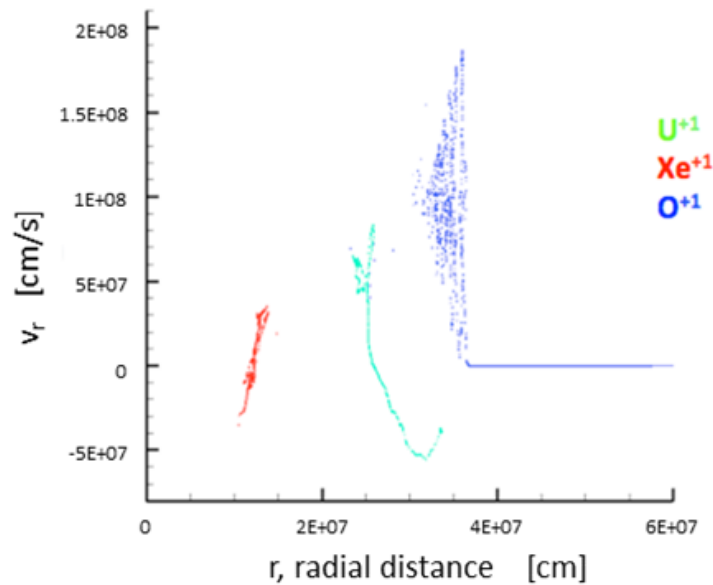


Figure 35. Simulation involving Uranium +1 (green) and Xenon +1 (red) into Oxygen +1 (blue) without charge exchange where debris couples into background.

The simulation was run again with all the same parameters and charge exchange was enabled. Figure 36 shows the phase space distribution of the debris at the completion of the simulation. The comparison between Figures 35 and 36 show the impact of charge exchange in the simulation.

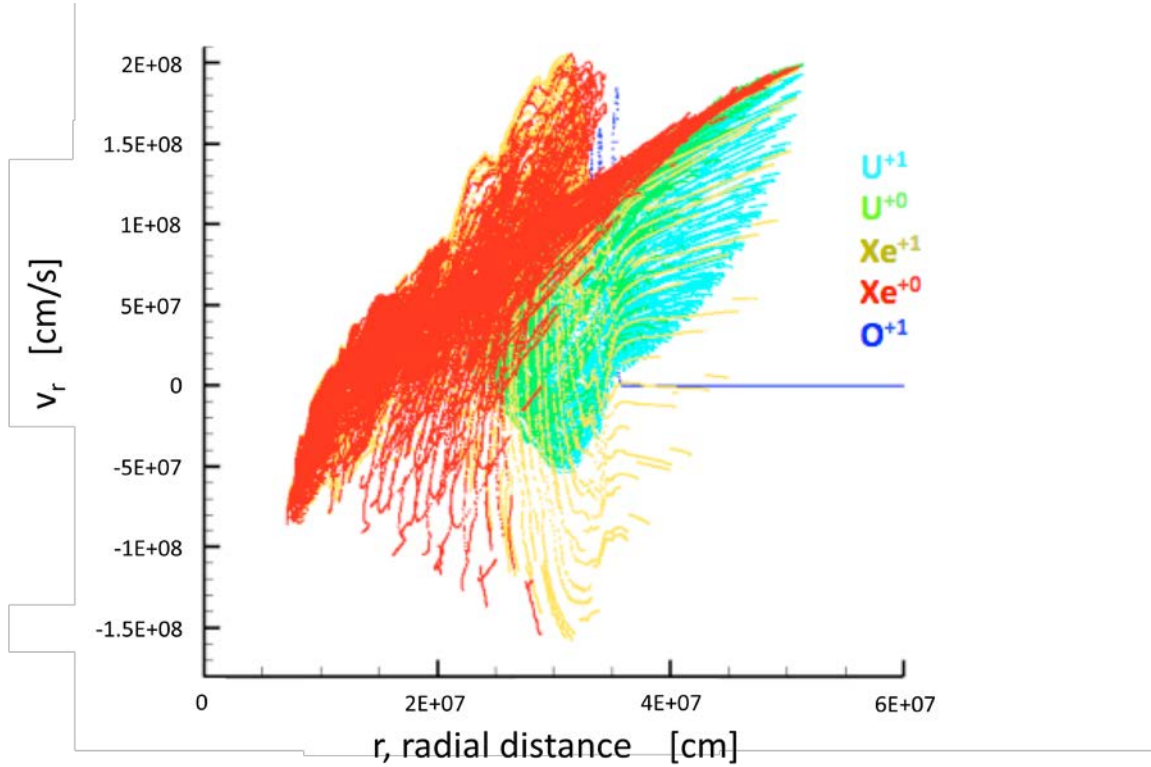


Figure 36. Simulation involving Uranium+1 (light blue) and Xenon+1 (red) into Oxygen+1 (blue) with charge exchange forming neutral Uranium (green) and neutral Xenon (gold) where some debris slips through the background.

ZMR calculated the portion of the debris ahead of the shock front which was set at  $B_z=0.4$  Gauss. With charge exchange enabled, 10.7% of the debris slipped through the shock in the background plasma. The results are shown in Table 8 below. The last four columns show the number of atoms ahead of the shock front at the completion of the simulation. Without charge exchange, there is no mechanism for the simulation to produce  $U^{+0}$  or  $Xe^{+0}$  so they could not be in front of the shock front at the 5000 time step in the first simulation (second row of table).

	Total # of U <sup>+1</sup> ions (t=0)	Total # of Xe <sup>+1</sup> ions (t=0)	Total # of U <sup>+0</sup> atoms (t=0)	Total # of Xe <sup>+0</sup> atoms (t=0)	Total # of U <sup>+1</sup> ions ahead of shock front (t=5000)	Total # of Xe <sup>+1</sup> ions ahead of shock front (t=5000)	Total # of U <sup>+0</sup> ions ahead of shock front (t=5000)	Total # of Xe <sup>+0</sup> ions ahead of shock front (t=5000)
Without Charge Exchange	1.24x10 <sup>27</sup>	2.47x10 <sup>26</sup>	0	0	0	0	NA	NA
With Charge Exchange	1.24x10 <sup>27</sup>	2.47x10 <sup>26</sup>	0	0	1.84x10 <sup>23</sup>	7.92x10 <sup>23</sup>	8.05x10 <sup>18</sup>	1.43x10 <sup>23</sup>

Table 8. Comparison of slip through data without and with charge exchange for uranium and xenon.

*c. Uranium and Zirconium*

Again, the debris began the simulation with a speed of  $2 \times 10^8$  [cm/s] and the number densities were adjusted so the system had kinetic energy representative of 0.25 MT of yield. The simulation was initially run without charge exchange enabled. Figure 37 shows the debris clearly coupled behind the shock front at the end of the simulation.

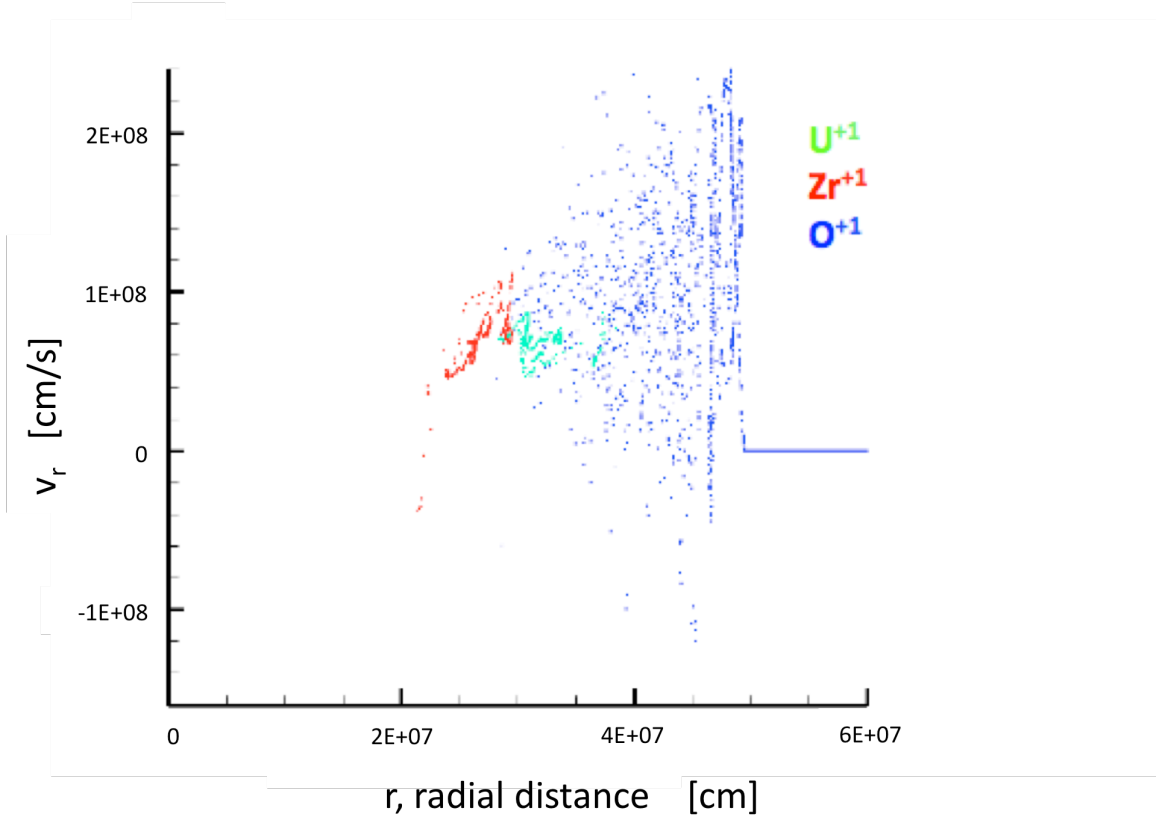


Figure 37. Simulation involving Uranium +1 (green) and Zirconium +1 (red) into Oxygen +1 (blue) without charge exchange where debris couples into background.

The simulation was run again with all the same parameters and charge exchange was enabled. Figure 38 shows the phase space disposition of the debris at the completion of the simulation with charge exchange. The comparison between Figures 37 and 38 shows the impact on the simulation results with charge exchange enabled.



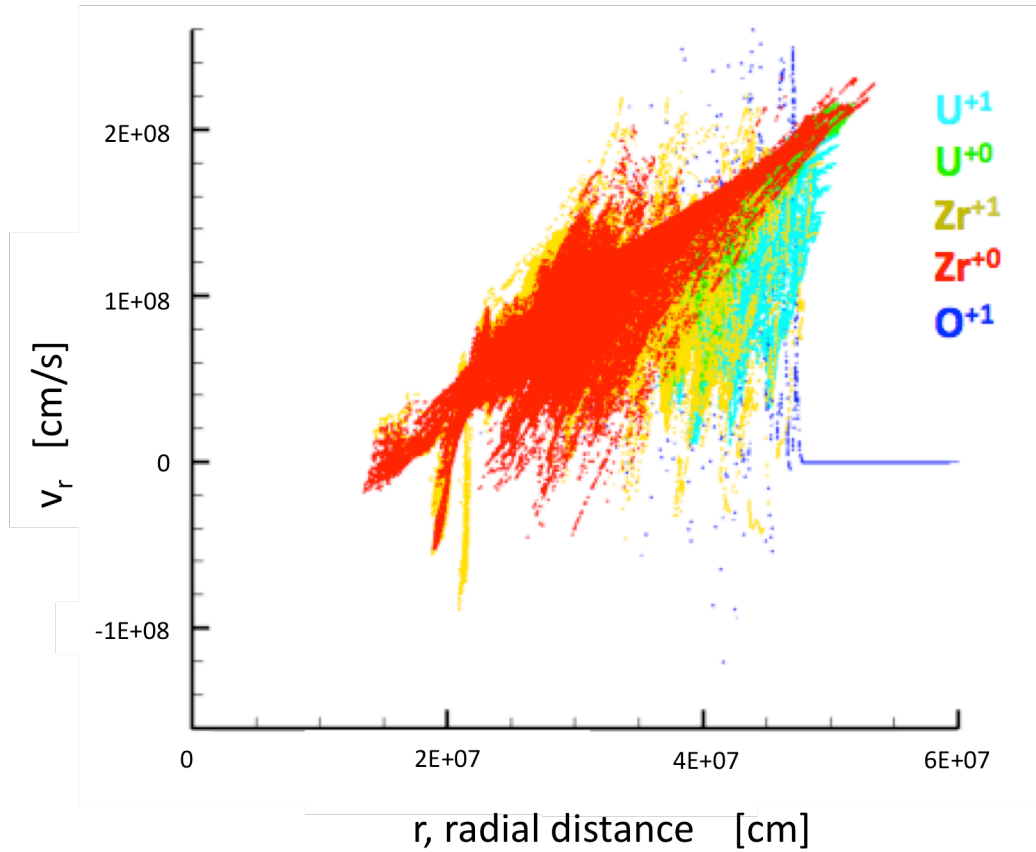


Figure 38. Simulation involving Uranium +1 (Blue) and Zirconium +1 (Yellow) into Oxygen +1 (Blue) with charge exchange where some debris slips through the background.

At the completion of the simulation with charge exchange enabled, 2.3% of the total debris had slipped through the shock front, and nearly all that debris was neutral. There were at least six orders of magnitude between the number of neutral and charged constituents in the debris ahead of the shock front. The results are shown in Table 9 below. The last four columns show the number of atoms ahead of the shock front at the completion of the simulation. Without charge exchange, there is no mechanism for the simulation to produce  $U^{+0}$  or  $Zr^{+0}$  so they could not be in front of the shock front at the 5000 time step in the first simulation (second row of table).

	Total # of U <sup>+1</sup> ions (t=0)	Total # of Zr <sup>+1</sup> ions (t=0)	Total # of U <sup>+0</sup> atoms (t=0)	Total # of Zr <sup>+0</sup> atoms (t=0)	Total # of U <sup>+1</sup> ions ahead of shock front (t=5000)	Total # of Zr <sup>+1</sup> ions ahead of shock front (t=5000)	Total # of U <sup>+0</sup> ions ahead of shock front (t=5000)	Total # of Zr <sup>+0</sup> ions ahead of shock front (t=5000)
Without Charge Exchange	1.24x10 <sup>27</sup>	3.55x10 <sup>27</sup>	0	0	0	0	NA	NA
With Charge Exchange	1.24x10 <sup>27</sup>	3.55x10 <sup>27</sup>	0	0	1.51x10 <sup>19</sup>	9.76x10 <sup>16</sup>	4.31x10 <sup>25</sup>	6.79x10 <sup>25</sup>

Table 9. Comparison of slip through data without and with charge exchange for uranium and xenon.

*d. Uranium and Lead*

Again, the debris began the simulation with a speed of  $2 \times 10^8$  [cm/s] and the number densities were adjusted so the system had kinetic energy representative of 0.25 MT of yield. The simulation was initially run without charge exchange. Figure 39 shows the debris clearly coupled behind the shock front at the end of the simulation.

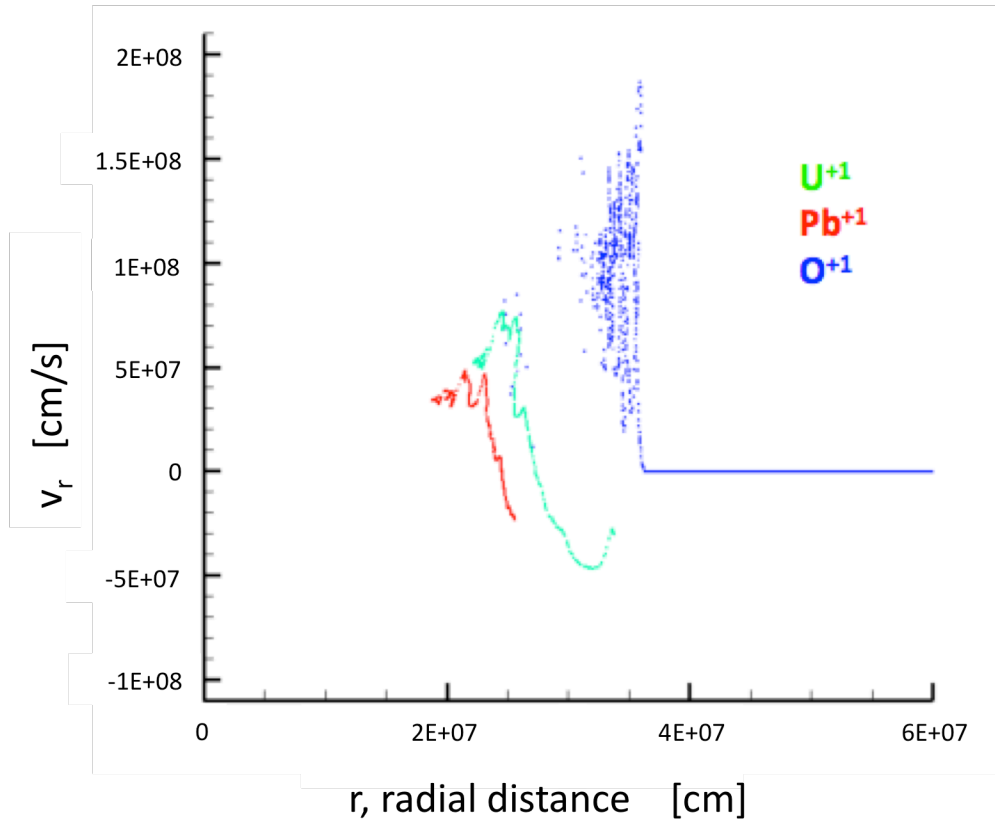


Figure 39. Simulation involving Uranium +1 (Green) and Lead +1 (red) into Oxygen +1 (Blue) without charge exchange where debris couples into background.

The simulation was run again with all the same parameters and charge exchange was enabled. Figure 40 shows the phase space disposition of the debris at the completion of the simulation with charge exchange. The comparison between Figures 39 and 40 shows the impact on the simulation results with charge exchange enabled.

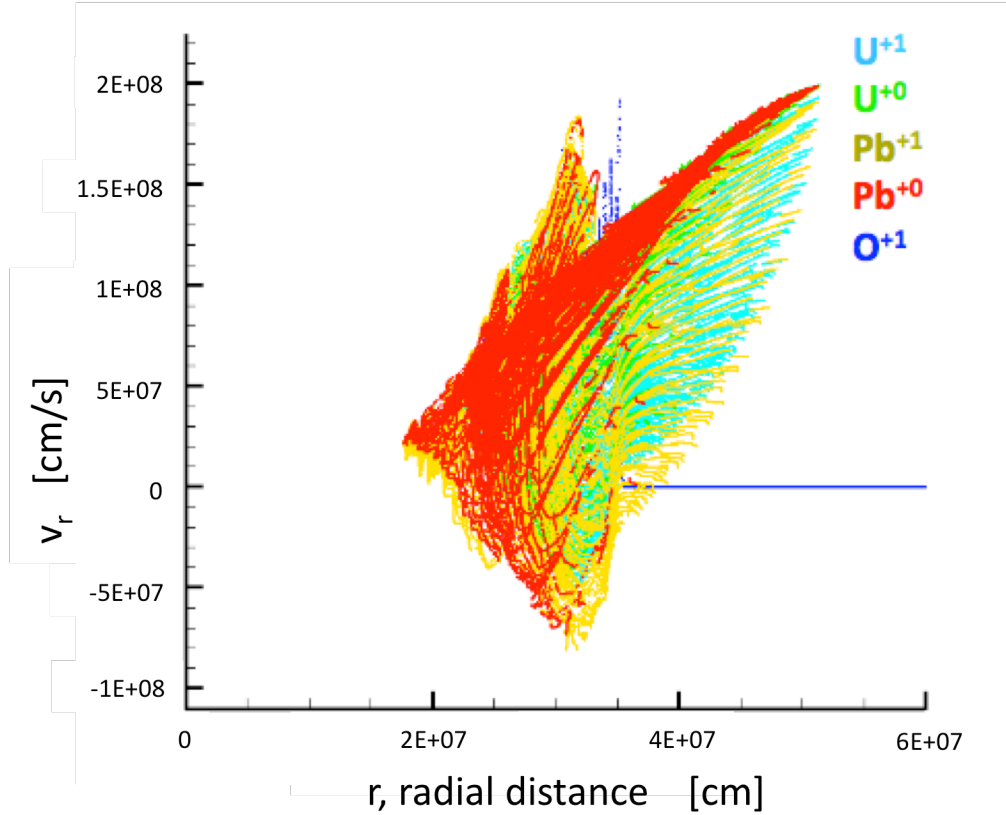


Figure 40. Simulation involving Uranium +1 (Blue) and Lead +1 (Yellow) into Oxygen +1 (Blue) with charge exchange where debris slips through background.

At the completion of the simulation, 6.4% of the total debris had passed through the shock front, and nearly all that debris was neutral. There was a two order of magnitude difference between the neutral and charged constituents of the debris ahead of the shock front. The results are shown in Table 10 below. The last four columns show the number of atoms ahead of the shock front at the completion of the simulation. Without charge exchange, there is no mechanism for the simulation to produce  $U^{+0}$  or  $Pb^{+0}$  so they could not be in front of the shock front at the 5000 time step in the first simulation (second row of table).

	Total # of U <sup>+1</sup> ions (t=0)	Total # of Pb <sup>+1</sup> ions (t=0)	Total # of U <sup>+0</sup> atoms (t=0)	Total # of Pb <sup>+0</sup> atoms (t=0)	Total # of U <sup>+1</sup> ions ahead of shock front (t=5000)	Total # of Pb <sup>+1</sup> ions ahead of shock front (t=5000)	Total # of U <sup>+0</sup> ions ahead of shock front (t=5000)	Total # of Pb <sup>+0</sup> ions ahead of shock front (t=5000)
Without Charge Exchange	1.24x10 <sup>27</sup>	1.55x10 <sup>26</sup>	0	0	0	0	NA	NA
With Charge Exchange	1.24x10 <sup>27</sup>	1.55x10 <sup>26</sup>	0	0	1.89x10 <sup>23</sup>	1.39x10 <sup>23</sup>	7.92x10 <sup>25</sup>	9.86x10 <sup>24</sup>

Table 10. Comparison of slip through data without and with charge exchange for uranium and lead.

## 6. Calculations of Neutral Yield to Match Measured Flux

Assuming the fission fraction of the total yield is 0.5 and each fission produces two fission fragments, STARFISH would produce  $2 \times 10^{26}$  fission fragments. Assuming four beta decays per fission fragment, this corresponds to  $8 \times 10^{26}$  electrons from beta decay. Hess states the total number of trapped electrons between 1.75 Earth radii ( $R_e$ ) and  $2.25 R_e$  is  $1.2 \times 10^{26}$  electrons.<sup>77</sup> Hess' number of trapped electrons corresponds to 15% of the total electrons from beta decay. This rough calculation benchmarks approximately how many neutrals are required to traverse across magnetic field lines for subsequent beta decay and injecting the high-energy electrons into higher L-shells. There are many subtleties not addressed in this rough calculation such as the time dependency of beta decay or the random pitch angle of high-energy electrons born of beta decay. However, stipulating that approximately 15% of the high-energy electrons born of beta decay were trapped following the STARFISH test does help judge that these results provide a reasonable contribution to the physics underlying the observations of STARFISH.

---

<sup>77</sup> W.N. Hess "The Artificial Radiation Belt Made on July 9, 1962" *The Journal of Geophysical Research*, 68 (1963) 680.

## **D. ANALYSIS OF DATA**

### **1. Atmospheric profiles**

The different atmospheric profiles in the simulations affected the results of the amount of neutrals that slipped ahead of the background plasma. The constant atmosphere resulted in roughly an order of magnitude fewer neutrals in front of the background plasma than the exponentially decreasing atmosphere. This difference can be first explained in terms of “freeze out.” In the exponentially decreasing atmosphere, the chance of either type of charge exchange decreasing exponentially with radial distance so after the initial round of charge exchange, the charge state remains constant (or “frozen”) for the remainder of the simulation. In a constant atmosphere, the density of the background oxygen, which is the catalyst for charge exchange, never changes so particles undergo multiple charge exchanges throughout the whole simulation. The charge state continues to alternate and those debris ions that become neutral undergo electron loss and become ionized again.

The second contribution the atmosphere makes to the effect of charge exchange is through the collisionless shock. A comparison of Figures 23 and 24 show that collisionless shock impacts the number of neutrals formed. The transfer of energy from the debris ions to the background ions has a two-fold effect on number of charge exchange interactions. First, the speed of ions undergoing collisionless shock is decreased and the speed directly impacts the calculations of the number of charge exchange interactions in a time step. Second, the cross sections for both electron capture and electron loss have energy dependence in them. Collisionless shock, which transfers energy from the debris ions to the background ions, decreases the energy used in the calculation of the cross section. The exponential atmosphere generates less collisionless shock as the number density of the background plasma decreases with radius and this collisionless shock impacts the amount of charge exchange.

### **2. Elemental Considerations**

The differences in the percentages of neutrals produced between the various elements have several explanations. First, the atomic differences among the elements

results in different cross sections (for both electron capture and electron loss). The features of the different atomic configurations results in more or less electromagnetic shielding of the valence electrons affecting the cross sections for both electron capture and electron loss. Second, differences in the percentage of neutral uranium between the various runs requires another explanation. Between the various simulations, the second debris element (lead, zirconium, xenon) had varying number densities to keep the overall energy in the simulations constant. Varying the number densities varied the coupling coefficient and affected the path of the uranium ions. As the neutral oxygen density is related to the path, the resulting collisionless shock affected the percentage of neutral uranium atoms formed across the various simulations.

## **E. RECOMMENDATIONS FOR FUTURE WORK**

The purpose of this work was to determine the impact of collisionless shock formation driven by multiple species of ions and charge exchange processes on the spatial distribution of debris from a HANE. This work used PIC simulations to identify the effect of charge exchange processes on previously fully coupled debris plasma expansions and showed it produced significant results when included in the simulation. This physics should be included in a higher fidelity model (like LLNL's KIM3D) since it appears to have measurable and realistic effects on the simulation in simpler geometry. Buffering limitations inherent within ZMR prevented running more than two species at a time with charge exchange enabled, as conserving energy and momentum resulted in an exponential growth in simulation particles over time. Employing a different buffering scheme would alleviate the geometric growth in simulation particles that hindered ZMR. Realistically, the debris from a HANE initially consists of thousands of different isotopes; while most are very short lived. After the debris has moved out several kilometers, it will still consist of substantially more than just two elements. The elements used in this work are from the peaks of the double humped curve of fission fragments (Figure 3) and also match the elements used by LLNL for other simulations. The use of more than two debris species will impact the final results. As the shock formation is non-linear and does impact the charge exchange, the inter-species influence will have impact

the shock formation. The differences in the shock formation will impact the charge exchange.

This work assumed all the debris started at charge state +1. In the simulation with charge exchange, ions could either be +1 or neutral and switched back and forth based on both the processes of electron capture and electron loss. Charge states higher than +1 are possible and ZMR was modified to handle higher charge states. A higher charge state ion would have a smaller Larmor radius and equations 14 and 30 suggest they would drive the collisionless shock differently. Starting an ion at charge state +2 presented the same geometric growth of simulation particles that plagued multispecies runs. Again, a better buffering system would be able to handle higher charge states. While ZMR can handle higher charge states, there is no current mechanism to handle charge exchange in integer values greater than one; that is, the code can not yet handle multiple electron losses or captures in a single event. The current limit remains changes to the charge state of  $\pm 1$  only.

More robust codes could better account for the real atmosphere. This work used both a constant density atmosphere and an exponentially decreasing atmosphere. The angular symmetry of ZMR makes neither of these assumptions physical. The real atmosphere is exponentially decreasing in the vertical direction and exponentially increasing in the downward direction. It is relatively constant parallel to the Earth. From the curvature of the L-shells, a bound particle will encounter a variety of densities as it travels. A charged particle bound to a field line of the magnetic field will encounter a different atmospheric density at the magnetic equator and at its mirror points. None of those conditions were included in this simulation and should be examined in future work to more accurately replicate the physical geometry as the ultimate goal is to predict the locations and charge state of the debris from any HANE.

The importance of the neutral fraction  $Y$  (equation 49) bears further examination, since this quantity impacts the total number of neutral particles. It suggests those neutrals with high ionization potentials (like the Group 7 and 8 elements from the periodic table) would have the largest impact on the total number of neutrals. Further code development



that focused on those elements that had the highest probability of forming neutrals would be an efficient method to draw out the physical effects of those elements.

## **E. CONCLUSIONS**

This dissertation examined the motion of the debris from a high altitude nuclear explosion (HANE) like STARFISH to determine if the physics of collisionless shock generated by multiple species and charge exchange supported the observation of high-energy electrons at higher L-shells. It was shown that the inclusion of charge exchange does impact the kinetic motion of the debris ions and can move them to locations not previously predicted but aligned with the measured data. Charge exchange accounts for previously unreported movement, which positions portions of the debris to locations where later beta decay would inject high-energy electrons consistent with observations. The effects of multiple species in the debris plasma is also found to be significant and demonstrates the importance of the non-linearity of the shock formation on the charge state of the debris ions while employing the charge exchange processes. Inclusion of the electron capture and electron loss computational routines in a higher fidelity code is important to get relevant physical results. If implemented, obtaining the proper results is likely to be well worth the additional computational time because this work has shown the physical results to be significantly impacted by the inclusion of charge exchange. Collisionless shock driven by multiple species was also modeled and did not prove significant as a stand-alone hypothesis, but the importance of collisionless shock on charge exchange was demonstrated.

An overview of the simulations examining charge exchange is illustrated in Figure 41. After the nuclear detonation (red star in Figure 41), the debris streams perpendicular to the ambient magnetic field. The interaction of this debris with the background plasma of flash ionized monatomic oxygen, shown as two dashed blue lines representing both density profiles, generates the collisionless shock. As the debris continues, it interacts with the neutral monatomic oxygen in the background and undergoes charge exchange. Once neutral, the particles continue on their trajectory unaffected by the electromagnetic forces. After several seconds of travel, those neutrals

were found to arrive at much higher L-shells and undergo beta decay introducing high-energy electrons similar to those observed in STARFISH.

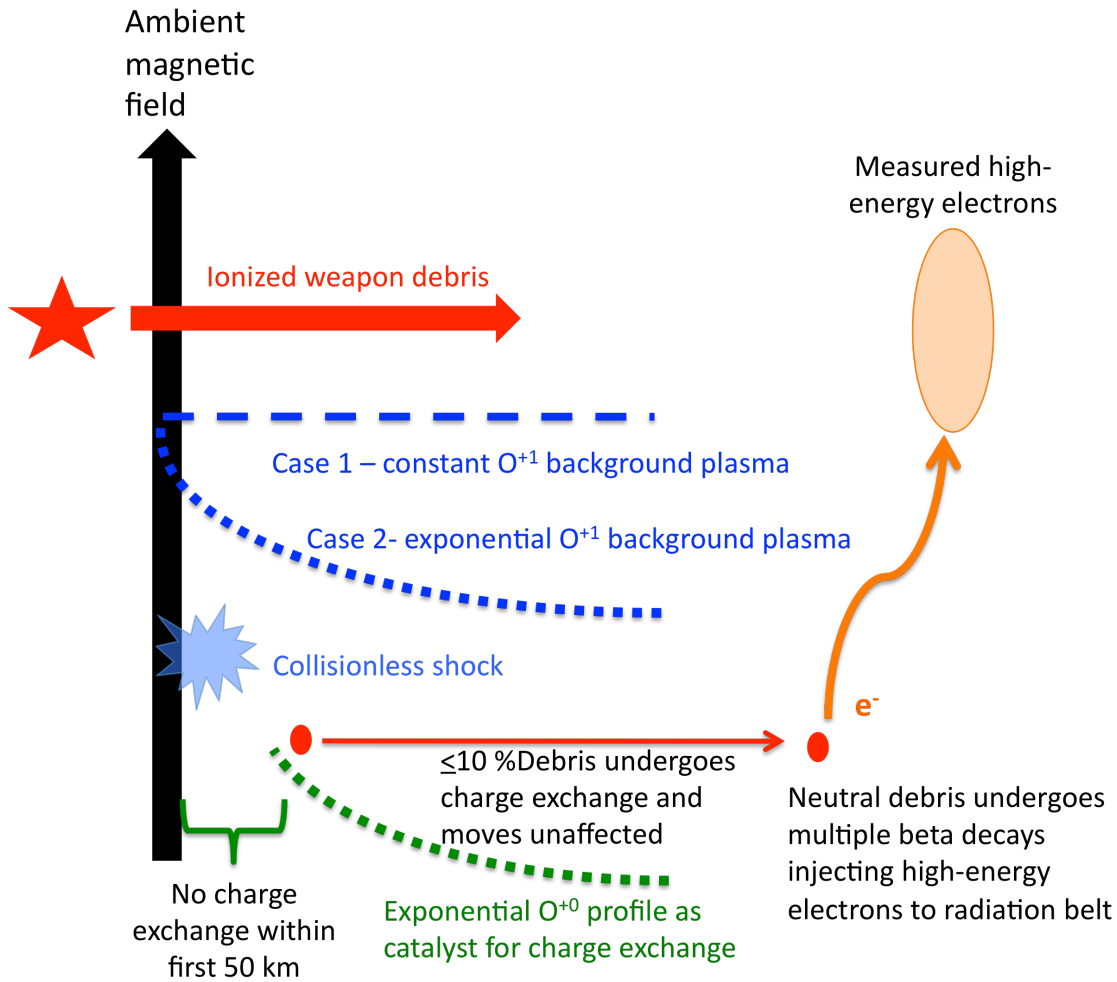


Figure 41. Graphic summary of simulations examining charge exchange.

Charge exchange is shown to be a significant contributing factor to this process and explains the observation of high-energy electrons at higher L-shells following a HANE; the physics of charge exchange should be included in future high fidelity modeling. While collisionless shock did not have an independent impact on the motion of the debris, when included in conjunction with charge exchange it did affect the simulation outcomes and future simulations should employ both principles to capture the relevant physics.

In the course of this research, both electron capture and electron loss computational subroutines were developed and implemented in a particle-in-cell hybrid code. The quantifiable differences of including these subroutines was determined and proved to be important.

While this work was not intended to replicated the precise results from STARFISH, it did prove the value of including the physics of collisionless shock and charge exchange into simulations in order to examine the motion of the debris across the magnetic field lines to higher L-shells where they beta decay and inject high-energy electrons.

THIS PAGE INTENTIONALLY LEFT BLANK

## LIST OF REFERENCES

- Anastasiadis, Anastasios. “Acceleration of solar energetic particles: The case of solar flares.” *Journal of Atmospheric and Solar-Terrestrial Physics*, 64 (2002) 481–488.
- Basler, R.P., R.B. Dyce and H. Leinbach. “High-Latitude Ionization Associated with the July 9 Explosion.” *Journal of Geophysical Research* 68 (1963) 741–743.
- Betz, Hans-Dieter. “Charge States and Charge-Changing Cross Sections of Fast Heavy Ions Penetrating Through Gaseous and Solid Media.” *Review of Modern Physics*, 44, 1972.
- Birdsall C.K. and A.B. Langdon. *Plasma Physics Via Computer Simulation*. New York: Taylor and Francis, 2005.
- Bransden, B.H., and M.R.C. McDowell. *Charge Exchange and the Theory of Ion-Atom Collisions*. Oxford: Clarendon Press, 1992.
- Brecht, S.H., D.W. Hewett and D.J. Larson. “A magnetized, spherical plasma expansion in an inhomogeneous plasma: The transition from super to sub-Alfvenic.” LLNL-JRNL-411549: Lawrence Livermore National Laboratory, 25 March 2009.
- Brown, W.L., W.N. Hess and J.A. Van Allen. “Introduction.” *Journal of Geophysical Research* 68, 1963
- Bridgeman, Charles. *Introduction to the Physics of Nuclear Weapons Effects*. Wright-Patterson Air Force Base: Defense Threat Reduction Agency, 2001.
- Bush. H.D. *Atomic and Nuclear Physics: Theoretical Principles*. Englewood Cliffs: Prentice-Hall, 1962.
- Bykov, A.M. “Shocks and particle acceleration in SNRs: theoretical aspects.” *Advances in Space Research* 33 (2004) 366–375.
- Chamberlain, Joseph. *Motion of Charged Particles in the Earth’s Magnetic Field*. New York: Gordon and Breach, 1964.
- Chen, Francis F. *Introduction to Plasma Physics and Controlled Fusion, Volume 1: Plasma Physics*. 2<sup>nd</sup> ed. New York: Springer, 2006.
- Cowling, T.G. *Magnetohydrodynamics*. Bristol, United Kingdom: Adam Hilger, 1976.

- Cross, Christopher G. *Computational Modeling of the Spatial Distribution and Temporal Decay of Geomagnetically Trapped Debris of a High Altitude Nuclear Detonation*. Monterey: Naval Postgraduate School, 2007.
- De Sequeira, M.L. and J.W.D. Connolly. "The Calculation of Heavy Atom Ionization Potentials by the Relativistic Transition State Approximation." *Chemical Physics Letters* 28 (1974) 482–484.
- Dyal, Palmer. "Particle and field measurements of the STARFISH diamagnetic cavity." *Journal of Geophysical Research* 111 (2006) 1–23.
- Gedalin, M., J.A. Newbury and C.T. Russel. "Numerical analysis of collisionless particle motion in an observed supercritical shock front." *Journal of Geophysical Research* 105 (2000) 105–114.
- Gibbons, M.R. and D.W. Hewett. "The Darwin Direct Implicit Particle-in-Cell (DADIPIC) Method for Simulation of Low Frequency Plasma Phenomena." *Journal of Computational Physics* 120 (1995) 231–247.
- Glassey, Robert T. and Walter A. Strauss. "Absence of Shocks in an Initially Dilute Collisionless Plasma." *Communications in Mathematical Physics* 113 (1987) 191–208.
- Glasstone, S. and P.J. Dolan. *The Effects of Nuclear Weapons*. Washington, DC: Department of the Army. DA Pamphlet No 50-3, 1977.
- Hedin, A.E. and A.O. Nier. "A Determination of the Neutral Composition, Number Density and Temperature of the Upper Atmosphere from 120 to 200 Kilometers with Rocket-Borne Mass Spectrometers." *Journal of Geophysical Research* 71 (1966) 4121–4131.
- Hellinger, Petr. "Structure and Stationarity of Quasi-perpendicular Shocks: Numerical simulations." *Planetary and Space Science* 51 (2003) 649–651.
- Hess, Wilmont. "The Effects of a High Altitude Explosions." NASA, Greenbelt MD, NASA TN D-2402, 1964.
- . *The Radiation Belts and Magnetosphere*. Waltham: Blaisdell Pub Co, 1968.
- Hewett, D.W. "A Global Method of Solving the Electron-Field Equations in a Zero-Inertia-Electron-Hybrid Plasma Simulation Code." *Journal of Computational Physics* 38 (1980) 378–395.
- . "Elimination of Electromagnetic Radiation in Plasma Simulation: The Darwin or Magneto Inductive Approximation." *Space Science Review* 42 (1985) 29–40.

- Hewett, D.W., S.H. Brecht and D.J. Larson. “The Physics of Ion Decoupling in Magnetized Plasma Expansions.” LLNL-CONF-470416. Orlando: HEART Conference, 2011.
- Hockney, R.W. and J.W. Eastwood. *Computer Simulation Using Particles*. Philadelphia: Institute of Physics Publishing, 1988.
- Hoerlin, Herman. “United States High-Altitude Test Experiences: A Review Emphasizing the Impact on the Environment. A LASL Monograph.” Los Alamos NM: LA-6405, OCT 1976.
- Horowitz, E.J., D.E. Shumaker and D.V. Anderson. “QN3D: A three-dimensional quasi-neutral hybrid particle-in-cell code with applications to the tilt mode instability in field reversed configurations.” *Journal of Computational Physics* 84 (1989) 279–310.
- Jackson, John David. *Classical Electrodynamics*. Third Edition. Hoboken: John Wiley & Sons, 1999.
- Janev, R.K., L.P. Presnyakov and V.P. Shevelko. *Physics of Highly Charged Ions*. New York: Springer-Verlag, 1985.
- Johnson, R.E.. *Atomic and Molecular Collisions*. New York: Plenum, 1982.
- Kaspzak, W.T., D. Krankowsky and A.O. Nier. “A Study of Day-Night Variations in the Neutral Composition of the Lower Thermosphere.” *Journal of Geophysical Research, Space Physics* 73 (1968) 6765–6782.
- Kilb, R.W. and D.E. Glenn. “CMHD Simulations of Very High Altitude Nuclear Bursts from 0 to 1 second (U).” Santa Barbara: Mission Research Corporation.
- Knudsen, H., H.K. Haugen and P. Hvelplund. “Single-electron-capture cross section for medium- and high-velocity, highly charged ions colliding with atoms.” *Physical Review A* 23 (1981) 597–610.
- Krane, Kenneth. *Introduction to Nuclear Physics*. New York: John Wiley & Sons, 1988.
- Ledvina, S.A., Y.J. Ma and E. Kallio. “Modeling and Simulating Flowing Plasmas and Related Phenomena.” *Space Science Review* 139 (2008) 143–189.
- Limited Test Ban Treaty, <http://www.state.gov/www/global/arms/treaties/lbtbt1.html>, (accessed 5 October, 2011)

- Martinez, H., C. Cisneros, I. Dominguez and I. Alvarez. "Measurements of single electron capture cross sections in collisions of Kr<sup>+</sup> with Xe." *Nuclear Instruments and Methods in Physics Research Section B: Beam Interactions with Materials and Atoms* 124 (1997) 464–468.
- McCormac, Billy Editor. *Radiation Trapped in the Earth's Magnetic Field*. New York: Science Publishers, 1966.
- McDaniel, Earl W, J.B.A. Mitchell and M. Eugene Rudd. *Atomic Collisions: Heavy Particles*. New York: Wiley, 1993.
- McDiarmid, I.B. and J.R. Burrows. "Satellite Measurements in the 'STARFISH' Artificial Radiation Zone." *Canadian Journal of Physics* 41 (1963) 63–132.
- McIlwain, Carl E.. "Coordinates for Mapping the Distribution of Magnetically Trapped Particles." *Journal of Geophysical Research* 66 (1961) 3681–3691.
- Mozer, F.S., D.D. Elliott, J.D. Mihalov, G.A. Paulikas, A.L. Vampola and S.C. Freden. "Preliminary Analysis of the Fluxes and Spectrums of Trapped Particles after the Nuclear Test of July 9, 1962." *Journal of Geophysical Research* 68 (1963) 641–649.
- Niemann, C., W. Gekelman, C.G. Constantin, E.T. Everson, D.B. Schaeffer, S.E. Clark, D. Winske, A.B. Zylstra, P. Pribyl, S.K.P. Tripathi, D. Larson, S.H. Glenzer and A.S. Bondarenko. "Dynamics of exploding plasmas in a large magnetized plasma." *Physics of Plasmas* 20 (2013) 12108-12120.
- Parks, George K. *Physics of Space Plasmas, An Introduction*. 2<sup>nd</sup> ed. Boulder: Westview Press, 2004.
- "A 'Quick Look' At the Technical Results of STARFISH PRIME." AD-A955 411, August 1962.
- Sawyer, R.F. "Electron capture rates in a plasma." *Physical Review C* 83 (2011) 1–9.
- Schlachter, A.S., J.W. Stearns, W.G. Craham, K.H. Berkner, R.V. Pyle and J.A. Tanis. "Electron capture for fast highly charged ions in gas targets: An empirical rule." *Physical Review A*. 27 (1983) 3372–3374.
- Schulz, M. "Canonical Coordinates for Radiation-Belt Modeling." *Geophysical Monograph Series, Radiation Belts: Models and Standards*. American Geophysical Union: Washington, DC (1996).



- Shevelko, V.P., I.L. Beigman, M.S. Litsarev, H. Tawara, I.Yu Tolstikhina, and G. Weber. “Charge-changing processes in collisions of heavy many-electron ions with neutral atoms.” *Nuclear Instruments and Methods in Physics Research B* 269 (2011) 1455–1463.
- Shevelko, V.P., I. Yu. Tolstikhina and Th. Stöhlker. “Stripping of fast heavy low-charged ions in gaseous targets.” *Nuclear Instruments and Methods in Physics Research B* 184 (2001) 295–308.
- Shumaker, D.E., D.V. Anderson and G.F. Simonson. “3D and 2D Simulation of an Expanding Plasma Using a Darwin Hybrid Particle Code.” UCRL-ID-109852, 2 March 1992.
- Simonson, G.F., D.W. Hewett, D.E. Shumaker, D.V. Anderson, J.A. Byers, and G. DiPeso. “Numerical Simulations of the Interactions of Nuclear Weapons with Geomagnetic Field.” UCRL-JC-109841: 1992 Sensor Technical Conference Patrick AFB, FL. 28 April 1992.
- Spjeldvik, Walther A and Theodore A. Fritz. “Theory for Charge States of Energetic Oxygen Ions in the Earth’s Radiation Belts.” *Journal of Geophysical Research* 83 (1978) 1583–1594.
- Thomas, V.A. and Stephan H. Brecht. “Two-dimensional simulation of high Mach number plasma interactions.” *Phys Fluids* 29 (1986) 2444–2454.
- Vainio, Rami , Laurent Desorgher, Daniel Heynderickx, Marisa Storini, Erwin Fluckiger, Richard B. Horne, Gennady A. Kovaltsov, Karel Kudela, Monica Laurenza, Susan McKenna-Lawlor, Hanna Rothkaehl and Ilya G. Usoskin. “Dynamics of the Earth’s Particle Radiation Environment.” *Space Science Review* 147 (2009) 187–231.
- Whipple, E.C. Jr. “A kinetic approach to magnetospheric modeling.” Quantitative Modeling of Magnetospheric Processes. American Geophysical Union: Washington, DC, 1979
- Winske, Dan. “Simulations of HANE/VHANE Dynamics.” LA-UR-91–3750. Los Alamos. 1991
- Winske, Dan and S. Peter Gary. “Hybrid simulations of debris-ambient ion interactions in astrophysical explosions.” *Journal of Geophysical Research* 112 (2007) 1–11.

THIS PAGE INTENTIONALLY LEFT BLANK

## **INITIAL DISTRIBUTION LIST**

1. Defense Technical Information Center  
Ft. Belvoir, Virginia
2. Dudley Knox Library  
Naval Postgraduate School  
Monterey, California